

LANGLEY GRANT
N-02-CR
261646
171P.

SURFACE PRESSURE DISTRIBUTIONS
ON A DELTA WING UNDERGOING LARGE
AMPLITUDE PITCHING OSCILLATIONS

Scott A. Thompson, Stephen M. Batill, and Robert C. Nelson
University of Notre Dame

NAG-1-727
December 1989

(NASA-09-186320) SURFACE PRESSURE
DISTRIBUTIONS ON A DELTA WING UNDERGOING
LARGE AMPLITUDE PITCHING OSCILLATIONS M.S.
Thesis (Notre Dame Univ.) 171 p CSCL 01A

490-17558

Unclass

93/02 0261040

SURFACE PRESSURE DISTRIBUTIONS
ON A DELTA WING UNDERGOING LARGE
AMPLITUDE PITCHING OSCILLATIONS

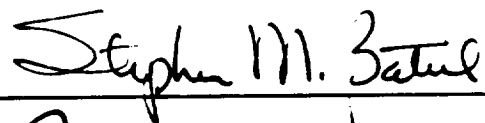
A Thesis

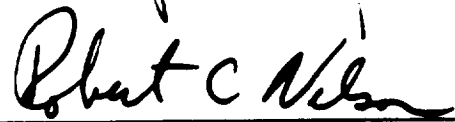
Submitted to the Graduate School
of the University of Notre Dame
in Partial Fulfillment of the Requirements
for the Degree of

Master of Science

by

Scott A. Thompson, B.S.M.E.





Directors

Department of Aerospace and Mechanical Engineering

Notre Dame, Indiana

July, 1989

**SURFACE PRESSURE DISTRIBUTIONS
ON A DELTA WING UNDERGOING LARGE
AMPLITUDE PITCHING OSCILLATIONS**

Abstract

by

Scott A. Thompson

Wind tunnel experiments were performed on a 70° sweep delta wing to determine the effect of a sinusoidal pitching motion on the pressure field on the suction side of the wing. Twelve pressure taps were placed from 35-90% of the chord, at 60% of the local semi-span. Pressure coefficients were measured as a function of Reynolds number and pitch rate.

The pressure coefficient was seen to vary at approximately the same frequency as the pitching frequency. The relative pressure variation at each chord location was comparable for each case. The average pressure distribution through each periodic motion was near the static distribution for the average angle of attack. Upon comparing the upstroke and downstroke pressures for a specific angle of attack, the downstroke pressures were slightly larger. Vortex breakdown was seen to have the most significant effect at the 40-45% chord location, where a decrease in pressure was apparent.

TABLE OF CONTENTS

	Page
LIST OF TABLES	iv
LIST OF FIGURES	v
NOMENCLATURE	x
ACKNOWLEDGEMENTS.....	xii
I. INTRODUCTION	1
1.1 Static Delta Wing Aerodynamics	1
1.1.1 Leading Edge Vortex Development.....	1
1.1.2 Leading Edge Vortex Breakdown.....	4
1.2 Unsteady Delta Wing Aerodynamics	7
1.3 Scope of Current Research	12
II. EXPERIMENTAL APPARATUS.....	14
2.1 Wind Tunnel and Test Section Specifications	14
2.2 Unsteady Pitching Mechanism.....	15
2.3 Displacement Transducer	17
2.4 Delta Wing Model : Design and Fabrication.....	19
2.5 Pressure Measuring Equipment	20
2.6 Data Acquisition and Reduction Equipment.....	21
III. EXPERIMENTAL PROCEDURE.....	23
3.1 Experimental Set-Up.....	23
3.2 Location of Pressure Transducers.....	24
3.3 Obtaining Pressure Data	30
3.3.1 Pressures Recorded.....	30
3.3.2 Conversion to Pressure Coefficient.....	34
3.3.3 Correspondence to Vortex Breakdown Location.....	36
3.4 Ensemble Averaging.....	37
3.5 Accuracy and Error Analysis.....	38
IV. EXPERIMENTAL RESULTS	44

4.1	Overview.....	44
4.2	Model Motion and Freestream Response.....	45
4.3	Static Pressure Data.....	46
4.4	Unsteady Pressure Data.....	50
4.4.1	Tests at Reynolds Number 250,000.....	52
4.4.2	Tests at Reynolds Number 335,000.....	58
4.4.3	Tests at Reynolds Number 420,000.....	61
4.4.4	Tests at Reynolds Number 500,000.....	63
4.5	Additional Pressure Data.....	65
4.5.1	Right Side Pressure Data.....	66
4.5.2	Reference Pressure Port Data.....	69
V.	CONCLUSIONS AND RECOMMENDATIONS.....	71
5.1	Conclusions.....	71
5.1.1	Unsteady Pressure Data.....	71
5.1.2	Acquisition of Unsteady Pressure Data.....	76
5.2	Recommendations.....	78
	APPENDIX A - UNCERTAINTY OF PRESSURE COEFFICIENTS.....	146
	APPENDIX B - TABULAR STATIC DATA.....	148
	APPENDIX C - WIRING SCHEMATICS.....	150
	REFERENCES.....	153

LIST OF TABLES

Table		Page
1	LIST OF DYNAMIC TESTS PERFORMED.....	81
2	LIST OF STATIC TESTS PERFORMED.....	82
3	STANDARD DEVIATION OF THE 50 SETS OF PRESSURE DATA AVERAGED FOR EACH TEST	83
4	CORRESPONDENCE OF CYCLES OF MOTION TO ANGLE OF ATTACK.....	84
5	PERCENT VARIATION OF INSTANTANEOUS PRESSURE COEFFICIENT FROM MEAN VALUE : RE = 250,000 , U = 30 FT/S.....	85
6	PERCENT VARIATION OF INSTANTANEOUS PRESSURE COEFFICIENT FROM MEAN VALUE : RE = 335,000 , U = 40 FT/S.....	86
7	PERCENT VARIATION OF INSTANTANEOUS PRESSURE COEFFICIENT FROM MEAN VALUE : RE = 420,000 , U = 50 FT/S.....	87
8	PERCENT VARIATION OF INSTANTANEOUS PRESSURE COEFFICIENT FROM MEAN VALUE : RE = 500,000 , U = 60 FT/S.....	88
9	PERCENT VARIATION OF INSTANTANEOUS PRESSURE COEFFICIENT FROM MEAN VALUE FOR RIGHT SIDE DISTRIBUTIONS : RE = 250,000 and 335,000 , U = 30 AND 40 FT/S , k = 0.10.	89
A1	UNCERTAINTIES IN THE PRESSURE COEFFICIENT : STATIC AND DYNAMIC TESTS.....	147
B1	TABULAR STATIC DATA	149

LIST OF FIGURES

Figure		Page
1.1	Delta Wing Leading Edge Vortex Flow.....	90
1.2	Leading Edge Vortex Cross Section.....	91
1.3	Lift Coefficient as a Function of Angle of Attack for 70° Leading Edge Sweep Delta Wing. Courtesy of McKernan, 1983.....	92
1.4	Schematic of Leading Edge Vortex Breakdown.....	93
1.5	Vortex Breakdown Occuring on Delta Wing Fighter Aircraft.....	94
1.6	Schematic of Vortex Breakdown Area.....	95
2.1	Low Speed Wind Tunnel Facility.....	96
2.2	Unsteady Pitching Mechanism.....	97
2.3	Displacement Transducer : Schematic.....	98
2.4	Displacement Transducer Calibration Curve.....	99
2.5	Delta Wing Pressure Model.....	100
2.6	Data Aquisition Flowchart	101
3.1	Experimental Set-Up.....	102
3.2	Experimental Set-Up for Preliminary Tubing Transfer Function Analysis.....	103
3.3	Frequency Response for Manometers and Tubing Used to Measure Fluctuating Surface Pressures : Transfer Function and Phase Shift up to 100 Hz.....	104

3.4	Frequency Response for Manometers and Tubing Used to Measure Freestream Dynamic Pressure : Transfer Function and Phase Shift up to 100 Hz.....	105
3.5	Dynamic Pressure Loss Through Wind Tunnel Screens.....	106
3.6	Discrete Fourier Transform of Unsteady Pressure Data : Re = 500,000 , U = 60 ft/s , k = 0.30.....	107
4.1	Static Data : U = 30 ft/s , α = 29° , 34° , 39°.....	108
4.2	Static Data : U = 40 ft/s , α = 29° , 34° , 39°.....	109
4.3	Static Data : U = 50 ft/s , α = 29° , 34° , 39°.....	110
4.4	Static Data : U = 60 ft/s , α = 29° , 34° , 39°.....	111
4.5	Comparison Between Current Static Data and McKernan (1983) and Visser (1989).....	112
4.6	Angle of Attack Time History for Unsteady Model Motion.....	113
4.7	Unsteady Pressure Data : Pressure Coefficient as a function of Time and Chord Location. Re = 250,000 , U = 30 ft/s , k = 0.10.....	114
4.8	Unsteady Pressure Data : Pressure Coefficient as a function of Time and Chord Location. Re = 250,000 , U = 30 ft/s , k = 0.20.....	115
4.9	Unsteady Pressure Data : Pressure Coefficient as a function of Time and Chord Location. Re = 250,000 , U = 30 ft/s , k = 0.30.....	116
4.10	Unsteady Pressure Data : Pressure Coefficient as a function of Time and Chord Location. Re = 335,000 , U = 40 ft/s , k = 0.10.....	117
4.11	Unsteady Pressure Data : Pressure Coefficient as a function of Time and Chord Location. Re = 335,000 , U = 40 ft/s , k = 0.20.....	118
4.12	Unsteady Pressure Data : Pressure Coefficient as a function of Time and Chord Location. Re = 335,000 , U = 40 ft/s , k = 0.30.....	119

4.13	Unsteady Pressure Data : Pressure Coefficient as a function of Time and Chord Location. $Re = 420,000$, $U = 50$ ft/s , $k = 0.10$	120
4.14	Unsteady Pressure Data : Pressure Coefficient as a function of Time and Chord Location. $Re = 420,000$, $U = 50$ ft/s , $k = 0.20$	121
4.15	Unsteady Pressure Data : Pressure Coefficient as a function of Time and Chord Location. $Re = 420,000$, $U = 50$ ft/s , $k = 0.30$	122
4.16	Unsteady Pressure Data : Pressure Coefficient as a function of Time and Chord Location. $Re = 500,000$, $U = 60$ ft/s , $k = 0.10$	123
4.17	Unsteady Pressure Data : Pressure Coefficient as a function of Time and Chord Location. $Re = 500,000$, $U = 60$ ft/s , $k = 0.20$	124
4.18	Unsteady Pressure Data : Pressure Coefficient as a function of Time and Chord Location. $Re = 500,000$, $U = 60$ ft/s , $k = 0.30$	125
4.19	Unsteady Pressure Data from Right Side of Model: Pressure Coefficient as a function of Time and Chord Location. $Re = 250,000$, $U = 30$ ft/s , $k = 0.10$	126
4.20	Unsteady Pressure Data from Right Side of Model: Pressure Coefficient as a function of Time and Chord Location. $Re = 335,000$, $U = 40$ ft/s , $k = 0.10$	127
4.21	Unsteady Pressure Data : Pressure Coefficient as a function of Time. $Re = 250,000$, $U = 30$ ft/s , $k = 0.30$. Twelve Chord Locations Shown.....	128
4.22	Unsteady Pressure Data : Pressure Coefficient as a function of Time. $Re = 250,000$, $U = 30$ ft/s , $k = 0.30$. Two Chord Locations Shown. (Expanded View of Figure 4.19).....	129
4.23	Unsteady Pressure Data : Pressure Coefficient as a function of Time. $Re = 335,000$, $U = 40$ ft/s , $k = 0.30$. Two Chord Locations Shown.....	130
4.24	Unsteady Pressure Data : Pressure Coefficient as a function of Time. $Re = 500,000$, $U = 60$ ft/s , $k = 0.30$. Two Chord Locations Shown.....	131

4.25	Instantaneous Pressure Distribution at 34° Angle of Attack : Upstroke, Downstroke, and Static. Re = 250,000, U = 30 ft/s , k = 0.10.	132
4.26	Instantaneous Pressure Distribution at 34° Angle of Attack : Upstroke, Downstroke, and Static. Re = 250,000, U = 30 ft/s , k = 0.20.	133
4.27	Instantaneous Pressure Distribution at 34° Angle of Attack : Upstroke, Downstroke, and Static. Re = 250,000, U = 30 ft/s , k = 0.30.	134
4.28	Instantaneous Pressure Distribution at 34° Angle of Attack : Upstroke, Downstroke, and Static. Re = 335,000, U = 40 ft/s , k = 0.10.	135
4.29	Instantaneous Pressure Distribution at 34° Angle of Attack : Upstroke, Downstroke, and Static. Re = 335,000, U = 40 ft/s , k = 0.20.	136
4.30	Instantaneous Pressure Distribution at 34° Angle of Attack : Upstroke, Downstroke, and Static. Re = 335,000, U = 40 ft/s , k = 0.30.	137
4.31	Instantaneous Pressure Distribution at 34° Angle of Attack : Upstroke, Downstroke, and Static. Re = 420,000, U = 50 ft/s , k = 0.10.	138
4.32	Instantaneous Pressure Distribution at 34° Angle of Attack : Upstroke, Downstroke, and Static. Re = 420,000, U = 50 ft/s , k = 0.20.	139
4.33	Instantaneous Pressure Distribution at 34° Angle of Attack : Upstroke, Downstroke, and Static. Re = 420,000, U = 50 ft/s , k = 0.30.	140
4.34	Instantaneous Pressure Distribution at 34° Angle of Attack : Upstroke, Downstroke, and Static. Re = 500,000, U = 60 ft/s , k = 0.10.	141
4.35	Instantaneous Pressure Distribution at 34° Angle of Attack : Upstroke, Downstroke, and Static. Re = 500,000, U = 60 ft/s , k = 0.20.	142
4.36	Instantaneous Pressure Distribution at 34° Angle of Attack : Upstroke, Downstroke, and Static. Re = 500,000, U = 60 ft/s , k = 0.30.	143

4.37	Unsteady Pressure Data : Average Pressure Coefficient as a Function of Chord Location. $Re = 250,000$, $U = 30$ ft/s , $k = 0.10, 0.20, 0.30$. Static Curve at 34° also Shown.....	144
4.38	Unsteady Pressure Data : Pressure Coefficient Recorded at the Right Side, 90% Chord Location During each of Twelve Tests Performed on the Left Side. $Re = 250,000$, $U = 30$ ft/s , $k = 0.10$. Corresponds to Left Side Pressures Shown in Figure 4.7.....	145
C1	Wiring Schematic for Unsteady Pitching Mechanism Control Box	151
C2	Wiring Schematic for Unsteady Pitching Mechanism Motor Controller	152

NOMENCLATURE

Symbols

c	Root Chord
f	Pitching Frequency in Hz
k	Reduced Frequency; $k = 2\pi fc / U_\infty$
s	Trailing Edge Span Length
U	Local Velocity
U_∞	Freestream Velocity
W	Uncertainty in Pressure Coefficient (from Kline, 1985)
x	Chordwise Distance
y	Spanwise Distance

Greek Symbols

α	Angle of Attack
----------------------------	------------------------

Abbreviations

AD	Analog-to-Digital
C_p	Pressure Coefficient; $C_p = P_{tap} - P_\infty / Q_\infty$
DFT	Discrete Fourier Transform
LVDT	Linear Variable Differential Transformer
Re	Reynolds Number (Based on Root Chord for Delta Wing)

ACKNOWLEDGEMENTS

This research has been sponsored by the University of Notre Dame Department of Aerospace and Mechanical Engineering in conjunction with the National Aeronautics and Space Administration, Langley Research Center, Hampton, Virginia, under grant NAG-1-727. Jay Brandon is the NASA technical monitor for this research grant. The author wishes to thank the following individuals for their expertise and assistance during the course of this research. Their help in surmounting the insurmountable made this work possible :

Faculty advisors Dr. Stephen M. Batill and Dr. Robert C. Nelson for their expert guidance, insight and experience; and for their infinite patience.

Dr. Flint Thomas and Dr. Mihir Sen for their critical review and helpful suggestions.

Lab technicians Mike Swadener and Joel Preston for their help in fabricating and maintaining the model and testing apparatus.

Colleagues Scott LeMay, Ken Visser, Dr. Joe Hollkamp, and Roger Kenna for their constant assistance with and suggestions for the use of laboratory equipment, computer hardware and software, and darkroom equipment.

Secretary Mrs. Marilyn Walker for help with all the odds and ends.

Musicians of various backgrounds who were willing to put aside routine in an effort to express themselves in a different light.

"The ordinary man has problems; the warrior has only challenges."

I INTRODUCTION

Highly swept wings, often referred to as delta wings due to their triangular planform, have become increasingly popular as aerospace vehicles have become faster and more maneuverable. At low speeds, delta wings generate higher lift than rectangular planform wings, resulting in increased performance and handling capabilities. At supersonic speeds, delta wings have better drag characteristics, resulting in better supersonic cruise characteristics. In addition, delta wings have a structural advantage over rectangular planform wings.

1.1 Static Delta Wing Aerodynamics

1.1.1 Leading Edge Vortex Development

The flow over a flat delta wing with sharp leading edges at low angles of incidence is similar to the flow over a flat plate. As the angle of attack is increased, the flow field becomes dominated by two large scale vortices formed above the suction side of the wing. These vortices are counter-rotating and lie approximately along a line from the apex to the trailing edge. Further increase in angle of attack results in a phenomenon known as vortex breakdown, or

—
— simply breakdown. This is characterized by an abrupt change in the size and strength of the leading edge vortices.

—
— At moderate angles of attack, the incoming flow impinges on the lower surface of the delta wing, and moves outboard and downstream. Upon reaching the leading edge, the flow encounters a sharp change in geometry which cannot be negotiated. As a result the flow separates, forming a free shear layer that wraps over the leading edge and above the upper surface. This shear layer, or vortex sheet, then rolls up to form a vortex lying above the upper surface from the apex to the trailing edge (Gad-el-Hak 1983). Figure 1.1 is a sketch of the vortex structure over a flat plate delta wing. The roll-up occurs on both sides of the upper surface of the delta wing, resulting in two counter-rotating vortices. The freestream flow moving over these primary vortices is entrained towards the wing where it attaches to the upper surface. It is then swept outboard, beneath the primary vortices. The large adverse pressure gradient between the primary vortex and the leading edge causes the attached flow to separate, creating a secondary vortex. This secondary vortex is smaller and weaker than the primary vortex, and rotates in a direction opposite the primary vortex. The presence of the secondary vortex moves the primary vortex upward and inboard. Outboard of the secondary vortices the flow reattaches and continues moving towards the leading edge. As the flow reaches the leading edge it is entrained into the vortex sheet that is separating from the lower surface and feeding into the primary vortices. A spanwise cross section of the primary and secondary vortices is shown in Figure 1.2.

—
— Earnshaw (1961) took measurements of delta wing vortices and determined that the primary vortex is characterized by three regions: the outer or free shear layer, the rotational core, and the viscous sub-core. The regions

are characterized as follows. The free shear layer results from the flow separation at the leading edge, and is responsible for adding vorticity to the vortex core. The rotational core is the outer layer of the vortex core and is approximately thirty percent of the local semispan in diameter. The viscous sub-core is located within the rotational core and is approximately five percent of the local semispan in diameter. This region contains very large pressure and velocity gradients and rotates as a solid body.

The strength of the vortices depends on the planform geometry (essentially the leading edge sweep angle), the angle of attack, and the Reynolds number to a lesser extent. The strength of the vortex also increases down the length of the wing due to the addition of vorticity from the vortex feeding sheet rolling off of the leading edge. The height above the wing of the vortex also increases with chordwise distance.

For an aircraft equipped with delta wings, the increase of lift due to the leading edge vortices is as much as 40 percent compared to the potential lift generated over a flat plate wing. Axial velocities as high as three times the freestream velocity have been measured within the sub-core of the vortex (Earnshaw 1961). This high velocity fluid, in addition to the higher speed fluid caused by the acceleration of the flow as it passes over the vortices, causes lower pressures over the suction side of the wing, resulting in the increase in lift. This effect is commonly known as vortex or non-linear lift. The non-linearity of this additional lift results from the change of the vortex height-above-wing with changing angle of attack. The lift coefficient for a 70° leading edge sweep delta wing is shown in Figure 1.3. This lift data is from McKernan (1983). The angle of attack range of the current research is indicated on this figure. As the angle

of attack increases, the height above the wing increases, as does the velocity of the vortex; the pressure is lowered and the lift is increased.

One of the first research efforts to obtain pressure measurements over the surface of a delta wing was conducted by Peckham (1958). He examined fifteen wing planforms, recording force and pressure measurements. Peckham obtained spanwise pressure profiles for a variety of angles of attack and chord positions. Peckham identified the location of the vortex core from these profiles by the suction peak, caused by the high axial velocity of the core.

Further pressure measurements were made by McKernan (1983) and Er-EI (1985). McKernan obtained pressure measurements for a 70° sweep wing at varying angle of attack, yaw angle, and chord position. Er-EI conducted similar experiments on a 60° sweep wing. Both investigations showed the existence of a suction peak in the spanwise pressure profile due to the vortex core.

1.1.2 Leading Edge Vortex Breakdown

When the angle of incidence of a delta wing becomes large enough, the leading edge vortices undergo a transition. This transition, characterized by an abrupt decrease in vortex core flow velocity and increase in vortex size, is known as vortex breakdown. The specific angle of attack at which this occurs is a function of the leading edge sweep angle and the wing thickness to a lesser extent. A schematic of vortex breakdown is shown in Figure 1.4. Elle (1960) observed this phenomenon during a study of delta wings in both a wind tunnel and a water tunnel. Elle found that at high angles of attack the vortex underwent breakdown, and that this was related to the sweep angle of the wing. He also found that asymmetric breakdown occurred for a wing set at a non-zero yaw angle.

Further research was done by Lambourne and Bryer (1962) when they conducted a study of the vortex breakdown phenomenon using a water tunnel. By using flow visualization they identified various forms of breakdown, such as spiral and bubble types. They also verified that both the sweep angle and the angle of incidence affect the location of breakdown. In addition, Lambourne and Bryer conducted tests at root chord Reynolds numbers ranging from 10,000 to 4.6 million and found no significant difference, concluding that this type of leading edge vortex flow is unaffected by Reynolds number in this range.

Additional delta wing research was conducted by Hummel and Srinivasan in 1967, and by Wentz in 1968. Hummel and Srinivasan performed low speed wind tunnel tests on delta wings of varying aspect ratio, finding that the higher aspect ratio wings resulted in a lower angle of attack necessary for the onset of breakdown. Wentz tested thirteen flat plate delta wings with leading edge sweep angles from 45°-85°, using flow visualization to record breakdown position as a function of angle of attack. These tests verified that vortex breakdown occurs at a higher angle of attack as the sweep angle increases.

Breakdown first occurs in the wake near the trailing edge of the wing, and moves upstream towards the apex as the angle of attack is increased. A decrease in angle of attack moves the breakdown back downstream. When vortex breakdown occurs, both the axial and tangential velocities of the vortex flow decrease. In addition, the diameter of the vortex core increases abruptly. Upstream of the breakdown, the flow is tightly bound and vortical. Downstream, the flow moves with a turbulent swirling motion. Vortex breakdown causes a reduction of lift over the wing, as well as a reduction of nose-down pitching moment, both of which can lead to stall for a delta wing aircraft. This decrease in lift and pitching moment due to vortex breakdown was noted by Hummel and

Srinivasan (1967). Another undesirable effect occurs when the vortex breakdown over a delta wing aircraft impinges on the vertical stabilizer as shown in Figure 1.5. The unsteadiness and turbulence in the post breakdown vortex can cause structural vibration and large unsteady loads on the vertical tail and associated control surfaces. In addition, for the case of asymmetric breakdown location between the two leading edge vortices (frequently caused by a non-zero yaw angle or a large enough leading edge sweep angle), a rolling moment can be induced, leading to wing rock. The ability to control the vortex breakdown is tantamount to modifying these destabilizing effects.

Unfortunately, the theory behind vortex breakdown is primarily conceptual at this point. Both the causes and the physical characteristics are difficult to pinpoint. As is typical for most transition situations, vortex breakdown occurs over an area and not at a specific point. The vortex expands from a tightly rolled core to the larger, turbulent post-breakdown region over a small distance. For example Figure 1.6 shows a typical form of vortex breakdown. From Figure 1.6, the chord location of breakdown can be narrowed down to between 50% and 51% of the chord (this is only an example; breakdown does not necessarily occur at 50% of the chord). However, a more specific measurement requires a subjective estimate of where "breakdown" has occurred within the area from 50-51%. Typically in studies examining vortex breakdown, a specific part of this area is designated as the breakdown location, whether it is the front, the end, or a point roughly in the middle. This point is then used throughout the study as the point of breakdown. This can be complicated by any variation in the size or shape of the breakdown area. Both Lambourne and Bryer (1962) and Payne (1987) noted the existence of different types of vortex breakdown. In addition, the position of this area is unsteady; even at a constant angle of attack the breakdown position oscillates. Portnoy

(1988) noticed this phenomenon while using a water tunnel to examine the relative motion of the two vortices above a delta wing. He speculated that the unsteadiness of the breakdown location at a constant angle of attack may be due to the rotational structure of the vortex, or to buffeting caused by post-breakdown turbulence.

1.2 Unsteady Delta Wing Aerodynamics

The steady leading edge vortex flows over slender delta wings at large angles of attack has been studied extensively since the early 1950's. A large data base exists for the flow characteristics of leading edge vortices under steady flow conditions. However, this is not true for the unsteady aerodynamic characteristics of delta wings.

The presence of leading edge vortices is a high angle of attack phenomenon, and one of the major reasons for flying at large angles of attack is for maneuvering. Maneuvering flight is intrinsically transient, therefore, the understanding of the influence of unsteady motions on slender wing performance is essential. The flow field surrounding an aircraft undergoing a flight maneuver will not respond instantaneously, but rather will take time to adjust to the new aircraft attitude. The understanding and control of the leading edge vortices and vortex breakdown will make it possible to increase the performance and capabilities of delta wing aircraft. By understanding the reaction of the vortices to a given maneuver, it may be possible to exploit that reaction to obtain desirable aerodynamic loads over the wing.

Any unsteady motion of a delta wing results in a time lag of the flow field in response to the maneuver. At low angles of attack this can delay flow

separation, while at higher angles of attack it can delay vortex breakdown. For an oscillating or periodic motion, a hysteresis develops in the vortex and vortex breakdown positions, as compared to static positions. Lawson (1964) conducted experiments on a pitching 80° sweep delta wing and recorded the existence of a hysteresis loop in the vortex breakdown position. Using a static, or "pitch-pause" pitching motion, Lawson pitched the wing from 34° to 41° , and then back down to 34° . He found that the vortex breakdown would first appear over the trailing edge at 40° , but remained over the wing during the pitch down motion to 34° .

Gad-el-Hak and Ho (1985) performed experiments on a delta wing pitching sinusoidally from 0° - 30° over root chord Reynolds number from 25,000-340,000 and found no significant differences in the flow or in the vortex size due to a difference in Reynolds number. They also oscillated a 45° sweep delta wing from 10° - 20° and observed the hysteresis in breakdown position relative to the static case. This test was also conducted over a wide range of Reynolds numbers, again with no discernable difference between cases. In an earlier investigation, Gad-el-Hak et al (1983) had also noted a hysteresis in the height above the wing of the vortex core for a delta wing undergoing an oscillatory motion.

Similar hysteresis loops were also reported by Wolffelt (1986), Rockwell (1987), LeMay (1988) and Magness (1989). Wolffelt experimented with a 60° sweep delta wing undergoing harmonic pitching and plunging motions in a water tunnel. He pitched the wing at a constant pitch rate over ranges of 0 - 20° , 5 - 25° , and 10 - 30° . In each of these three cases, a hysteresis in the breakdown position relative to the static position was evident.

Rockwell (1987) examined a 45° sweep delta wing being periodically pitched in a water tunnel. Rockwell noted that the hysteresis loop became

larger with increased reduced frequency. For sufficiently high reduced frequency, Rockwell noticed that the hysteresis loop changes into a figure eight. Rockwell also examined the location of the secondary vortex, finding that its position was affected by the oscillatory motion in the same manner as the primary vortex.

In 1988 LeMay conducted further research into the effect of a sinusoidal pitching motion on vortex breakdown. LeMay used a 70° sweep flat plate delta wing and tested it over root chord Reynolds numbers from 90,000-350,000. Utilizing ranges of motion of 29-39° and 0-45° along with flow visualization methods, LeMay obtained information on both the chordwise breakdown position and the height above the wing of the breakdown; both as functions of angle of attack. LeMay examined the time lag between the dynamic and static positions of the vortex breakdown, and found that it became larger with increasing pitch rate, in agreement with Rockwell (1987).

One of the earliest investigations into the unsteady aerodynamic loads on a delta wing was conducted in 1954 by W.R. Laidlaw (Laidlaw, 1954). Using wings of rectangular, swept, and delta planform, Laidlaw examined the surface pressure distributions for a pure vertical translation and a sinusoidal pitching motion. Delta wings with leading edge sweep angles of 60° and 75° were used. Laidlaw pitched the wings at a root chord Reynolds number of 2.1 million about a mean angle of attack of 0°, and at several pitch rates. Pressure measurements were taken at several chord and span locations. Laidlaw then integrated this pressure field to obtain the lift distribution. Laidlaw also attempted to use analytic theory to evaluate the lift distribution, comparing this to the experimental results. Due the small angle of attack range used the leading edge vortex formation could be neglected, thus Laidlaw used a flat plate, low

aspect ratio lifting theory. He found moderate agreement between theory and experiment, and suggested some modifications to improve the theory.

Unsteady aerodynamic load research was not conducted at high angles of attack until later. In 1988 Bragg and Soltani presented a study on force and moment measurements for a 70° sweep delta wing of geometry similar to the model used by LeMay (1988). Using a constant chord Reynolds number of 1.5 million, Bragg and Soltani examined the aerodynamic loads on a static wing as well as a wing undergoing sinusoidal and ramp pitching motions. Hysteresis loops were noted in the aerodynamic loads. The magnitude of the hysteresis was found to be a function of reduced frequency and pitch rate. For the ramp pitching motion, they observed that after the model motion had stopped the force and moment oscillated with small amplitude before reaching equilibrium.

This hysteresis in the aerodynamic coefficients has been noted by other researchers as well. Brandon (1988) examined the effect of reduced frequency and mean angle of attack on the force and moment coefficients as well as the breakdown position. He found that the lag in the breakdown position and the overshoot and hysteresis in the aerodynamic coefficients were all functions of both pitching frequency and mean angle of attack. Brandon suggested that the overshoot in the normal force and pitching moment coefficients are due to a lag in the development of the vortex core and vortex breakdown during the pitching maneuver.

Jarrah (1989) conducted a study on delta wings of aspect ratios 1, 1.5, and 2; through a Reynolds number range of 450,000-850,000. He found that for a sinusoidal pitching motion, the hysteresis in the aerodynamic coefficients was a function of the pitch rate and the aspect ratio, and that the Reynolds number influence was negligible. Jarrah, similar to Brandon (1988), attributed the large overshoot of the aerodynamic loads during a pitch-up (Jarrah reported

overshoots of up to 50%) to a delay of the onset of vortex breakdown. Similarly, the undershoot seen during a pitch-down was attributed to a delay in the transition back to a pre-breakdown vortex core.

The effect of transient wing motion on vortex breakdown has also been studied, but to a lesser extent. For a transient motion, both the vortex core and the breakdown position experience a time lag before adjusting to the new wing attitude. Wolffelt (1986) also examined the effect of a "ramp" pitching motion during his study of a 60° sweep wing. He noted a lag in the breakdown position relative to the stationary case for the ramp motion. He also noted that the vortex breakdown continued to move after the model has stopped, traveling towards the stationary position.

Reynolds and Abtahi (1987) conducted research on a 75° sweep delta wing in a water tunnel. The root chord Reynolds number varied from 20,000-65,000; and the wing was pitched from 30-51° at pitch rates from 0.03-0.16 rad/s. Distinctive response characteristics were seen for the pitch-up and pitch-down cases. For the pitch-down cases, the breakdown required from 10-30 convective time units to reach the steady state position. Furthermore, Reynolds and Abtahi found that the data would collapse when non-dimensionalized against the freestream velocity.

Similar trends were noted by Magness et al (1989). Using a 75° sweep wing in a water tunnel, Magness verified several of the same results as the previous investigations. First, no Reynolds number effect was seen in the range from 120,000 to 360,000. Second, an increasing hysteresis was seen for a model oscillating from 5-55°, at an increasing pitch rate. Third, for ramp pitch-up and pitch-down motions, Magness noted that the breakdown position continued to move (by as much as 50% of the root chord) after the model motion

had ceased. In addition, Magness reported that the sinusoidal model motion resulted in a momentary upstream movement of the breakdown during a decrease in angle of attack (which is opposite the quasi-static movement). This was attributed to the fact that the breakdown was still moving towards the static position.

1.3 Scope of Current Research

The current research is intended to examine the problem of the unsteady delta wing and the pressure field associated with it. Although pressure distributions along the upper surface have been obtained for the numerous static cases, the amount of information available on the dynamic response of the pressure field to an oscillating wing is small in comparison. The goal of this research is an initial attempt at obtaining dynamic pressure data. The optimum experimental procedure will be considered as well as the unsteady pressure data. This investigation focuses on a 70° sweep, sharp-edged delta wing being pitched about its half-chord point. The pitching motion is sinusoidal, with an angle of attack range such that vortex breakdown exists over the wing throughout the pitching cycle. Pressure measurements were taken along a ray from the apex to the trailing edge of the delta wing model; with the ray located in such a way that it lies very near the leading edge vortices. The goals of this research are, in brief :

1. To obtain pressure distributions as a function of several Reynolds numbers and pitching rates, for one wing planform and one range of angle of attack.

2. To examine the practicality and validity of making dynamic pressure measurements without using surface mounted hardware.

3. To correlate the pressure distributions with previous data on the location of vortex breakdown during the pitching cycle; in effect examining the effect of vortex breakdown on the pressure field.

This study serves as an intermediate step in the road to the eventual control of the leading edge vortex structure. First it is necessary to predict the location of the vortex core and breakdown for a given situation, then to relate that information to the change in the surrounding pressure field, and then to the change in aerodynamic coefficients and loads. Hopefully it will then be possible to tailor a delta wing aircraft or a specific maneuver such that undesirable flight characteristics are avoided, or such that vortex breakdown is used to create superior flight characteristics.

II EXPERIMENTAL APPARATUS

2.1 Wind Tunnel and Test Section Specifications

The wind tunnel used during this research is located at the University of Notre Dame Aerospace Engineering Laboratory. It is one of two subsonic, low turbulence wind tunnels located at this facility. A schematic of the tunnel is shown in Figure 2.1. The inlet is 2.95 m square, has 12 anti-turbulence screens, and a 24:1 contraction ratio. The anti-turbulence screens break up large scale disturbances in the flow; smaller scale disturbances then dissipate in the contraction cone of the inlet. This results in a uniform velocity profile in the test section and a freestream turbulence intensity of less than 0.01%. The tunnel is an indraft or open-circuit type. After passing through the inlet, the flow moves through the test section, through a diffuser, then is exhausted to the outside atmosphere. The diffuser has a circular cross section, is 4.25 m long, and has a half-angle of 4.2°. The tunnel is powered by an 18.6 kW variable frequency AC motor which drives an eight bladed, 1.2 m diameter fan. The motor and fan assembly are housed in a screened shelter located outside of the laboratory. A foam rubber gasket is located between the diffuser and the test section to minimize vibrations from the motor assembly.

The open circuit, outside exhaust design provides a necessary method for expelling any flow visualization tracer particles. However, one end of the

tunnel being open to the atmosphere results in the tunnel being susceptible to gusts of wind and other atmospheric fluctuations. To minimize the effects of such fluctuations on the test section, a flow restrictor (consisting of a honeycomb of plastic tubes) is placed between the diffuser and the test section. The pressure drop through the restrictor reduces the effect of any atmospheric fluctuations.

The test section used for these experiments was 1.83 m long, with a 0.61 m square cross section. The rear panel of the section was hinged to allow for installation of the test model. Plate glass windows were mounted in the top and the front side of the section to facilitate lighting and viewing of the model. The model was strut mounted, with holes cut in the tunnel floor to accommodate the strut, the pitching mechanism drive shaft, and the leads for the pressure transducers. A pitot-static tube was mounted in the floor of the section, 80 cm upstream of the sting (and thus just downstream of the contraction inlet). The head of the pitot static tube was approximately centered in the cross section of the tunnel.

2.2 Unsteady Pitching Mechanism

In order to move the model in a sinusoidal pitching motion, a drive system was constructed that consisted of a motor connected to the delta wing model by a five bar linkage. This mechanism is identical to the one used by LeMay (1988). It consists of a five-bar linkage, one arm of which is used as a

mounting plate for the model. A schematic of the mechanism is shown in Figure 2.2.

A 1 hp 90 V DC electric motor (Dayton model 2M170C) is used to provide power for the system. Attached to this motor is a silicon control rectifier (SCR) motor controller (Dayton model 2M171C), capable of controlling the motor direction and speed. The motor is then connected to an 8:1 gear box by a timing belt and a timing gear. By using different timing gears, overall gear ratios of 26.66:1 and 14.22:1 can be achieved. Gear reductions of this size were used so that a low pitching rate could be achieved with a high motor rpm, providing steadier operation of the system. Pitch rates up to 2.1 Hz could be achieved with this system.

A drive arm was connected from a cam on the output end of the gear box to a slotted intermediate linkage. This intermediate linkage has a variable length lever arm and was connected to the drive rod of the model. This drive rod was 3.5 in (889 mm) behind the pivot point of the model. By changing the point of attachment of the motor drive rod the range of model motion could be changed (in effect changing the intermediate linkage lever arm). By altering the length of the sting, different mean angles of attack could be achieved. The pivot point of the model was located $5/8$ " (15.9 mm) below the one-half chord point. A change in the pitch rate could be affected by changing the rpm of the motor. An optical interrupter attached to the motor was used to read the rpm on a digital counter. This speed could be held at ± 3 rpm about a given setting. LeMay (1988) found that over the angle of attack range of 29° - 39° the pitching motion contained less than 2.5% harmonic distortion.

The gear box for the pitching mechanism contained a brake and an electric clutch so that the motion of the model could be controlled independently of the motor; that is, the motor would continue to run regardless of the model

motion. To operate this clutch, a control box was designed and built such that it could either engage the clutch continuously or engage it for a specified amount of time. In this manner the model could be oscillated in a continuous sinusoidal motion (by engaging the clutch continuously), or in a segment of a sine wave (by engaging the clutch and then braking). The pulse mode of the clutch was controlled by a trigger built into the clutch control box. By varying a potentiometer connected to the trigger, the time duration of the pulse could be changed, and thus the time duration of the model motion. In this manner the wing could be pitched in either a periodic or transient sinusoidal motion. Schematics for both the SCR motor controller and the specially designed clutch control box are shown in Appendix C.

2.3 Displacement Transducer

In order to provide information on the instantaneous angle of attack, a displacement transducer was used. This transducer was a Trans-Tek Series 240, model 0245-0000. A schematic of this unit is shown in Figure 2.3. The transducer consists of a single integrated unit housing the linear variable differential transformer, a solid state oscillator, and a phase-sensitive demodulator. The DC input signal is converted to an AC signal by the oscillator, which then excites the primary winding. The position of the core determines the excitation in the secondary windings. Since the circuits are placed in series opposition, the output is a DC signal that is proportional to the distance of the

core from the electrical center.¹

The transducer was clamped in a fixed position on the pitching mechanism support structure. The core was then attached to the intermediate linkage and was free to move vertically as the model pitched. The transducer has an input voltage range of 5-30 V DC; an input of 20 V DC was chosen. This value was picked to maximize the resolution of the transducer while staying with the voltage limit prescribed by the analog-to-digital conversion software.

Calibration tests were conducted on the transducer throughout the angle of attack range to be used. This consisted of measuring the angle of attack relative to the wind tunnel floor (used as a horizontal reference) and recording the transducer output. Then during the course of a sinusoidal pitching test, the instantaneous angle of attack could be obtained by converting the instantaneous transducer output from a voltage to an angle (by using the results of the calibration tests). Figure 2.4 contains the calibration curve that resulted from the calibration tests. The linearity of the curve is apparent; the small deviations from a straight line is due to the error involved in measuring the angle of attack during the calibration tests. The angle of attack could be measured to within $\pm 0.5^\circ$. This is not a significant amount considering the delta wing flow structure throughout the angle of attack range of 29-40°. Such a difference in angle would not cause a noticeable difference in the pressure field.

¹ This information was obtained from the Trans-Tek Incorporated sales catalog, dated May 1984.

2.4 Delta Wing Model : Design and Fabrication

A 70° leading edge sweep delta wing was used for all the tests performed during this research. The wing had a root chord of 16.375 in (416 mm) and a trailing edge span of 12 in (305 mm), giving it an aspect ratio of 1.47. The model was 0.75 in (168 mm) thick. Both the upper and lower surfaces had a symmetric 23° bevel on all three sides of the model. A schematic of the model is shown in Figure 2.5. The sweep angle and the planform dimensions of the model were chosen to correspond to previous studies using delta wings of similar geometry so that the different sets of data could be comparable. The thickness of the wing was chosen as the minimum possible to house the pressure transducer leads and provide a rigid bottom surface.

The model was constructed of plexiglass and had a hollow body. A removeable top plate was installed to house the mounting plate and the pressure transducer leads. This top plate was attached to the body of the wing by twelve screws spaced evenly along the outer edge of the plate. The top plate was 1/4" (6.35 mm) thick and the bottom surface was 3/16" (4.68 mm) thick, leaving a 5/16" (7.8 mm) cavity. Pressure taps (0.072" diameter holes) were drilled in the top plate along a ray lying from the apex to the trailing edge, at 60% of the local semi-span. Twelve taps were drilled along this ray on both sides of the centerline of the model, spanning from 35-90% of the root chord, in 5% intervals. Due to the width of the upper surface bevel, the taps at 35% of the chord lie on the bevels rather than on the horizontal top surface. Similarly, the 40% lies directly on the corner of the bevel and the top plate. An aluminum plate was glued to the bottom surface such that it coupled with the mounting plate on

the unsteady pitching mechanism. Behind this plate on the bottom of the model was a hole for the pressure transducer leads.

2.5 Pressure Measuring Equipment

Four pressure transducers were used to measure the unsteady pressures over the wing as well as the freestream dynamic pressure. These were all Setra Systems electronic manometers. Two of these had a range of 0-.55 inches of water (model 339B), and two had a range of 0-5.5 inches of water (model 339H). These transducers operate on 117 V AC, 60 Hz. Considering the Reynolds number range of this research, any of the four transducers would work equally well to measure the freestream dynamic pressure. Thus, at low Reynolds numbers the low range manometers were used to measure the unsteady pressure over the wing, to provide higher resolution. As the Reynolds number was increased, it was necessary to use the higher range manometers instead to avoid overloading the manometer.

The freestream manometer was connected to the the pitot-static tube located in the experimental section, while the model manometers were connected to the pressure taps located along the model surface. The pressure lines from each of these manometers consisted of Tygon plastic tubing. The tubing from the delta wing was 36" long, with 3/16" outer diameter and 1/16" inner diameter. The tubing from the pitot-static tube was 48" long, with an inner diameter of 0.25 inches. For the model manometers, the lines were connected from the manometer, through a hole drilled in the test section floor, along the sting, and through the hole in the bottom of the model to the pressure tap. A

piece of 0.072" stainless steel tubing was glued into each pressure tap on the model surface and then used as the connection for the plastic tubing. The pressure line from the freestream manometer was connected directly to the pitot-static tube.

2.6 Data Acquisition and Reduction Equipment

The primary piece of data acquisition equipment was a Digital Equipment Corporation (DEC) PDP 11/23 digital computer. The PDP 11/23 is equipped with a DEC VT52 terminal, an internal clock, and eight channel analog-to-digital (A/D) conversion. Data is stored on an RL02 hard disk. This system is also equipped with two Schmitt triggers for conditional sampling. Software was written in Fortran IV (version 2.5) for use with this system. This software made possible the acquisition of the freestream pressure, the unsteady pressures, and the displacement transducer output. This computer was used in conjunction with a Tektronix 4014-1 monitor used for online monitoring of the data.

Once the data was obtained with the 11/23 system, a PDP 11/34 multi-user system with a TSX-11 operating system was used for the data reduction process. The software for all data reduction was also written in Fortran IV. A Hewlett-Packard 7470A plotter was used for used for graphic presentation of the data, as well as a Macintosh SE and a Macintosh II. A schematic of the data acquisition system is shown in Figure 2.6.

During the preliminary investigation on the effect of remote pressure transducers and the connecting tubing, an MB Dynamics Modal Exciter and 2125MB Power Amp were used with a Scientific Atlanta Spectral Dynamics

SD380 Signal Analyzer in order to determine the transfer function for the tubing used to connect the pressure taps to the pressure transducers.

III EXPERIMENTAL PROCEDURE

This section is divided into five parts, each dealing with a different aspect of the overall experimental method. The first section describes the complete experimental set-up with all of its individual components, and the manner in which they interact to provide the desired data. The next section discusses the impact of using remote pressure transducers; the logic behind their use, testing of the system, and the effect on the magnitude and phase of the unsteady pressures. The third section then deals with the procedure for obtaining the unsteady pressure data in a manageable form. Following this, the final two sections are devoted to the data reduction process and an analysis of the accuracy of the data acquisition process, respectively.

3.1 Experimental Set-Up

A schematic of the complete experimental set-up is shown in Figure 3.1. The four primary parts of the experiment (the delta wing, the unsteady pitching mechanism, the pressure transducers, and the computer and A/D hardware) are positioned in such a way that ample operating and maintenance space is provided while keeping the interconnecting pieces of equipment close to each other.

The unsteady pitching mechanism is located outside of the tunnel directly beneath the delta wing, affixed to a rigid base. This base is also used to support the displacement transducer, which is attached at one end to the base, and at the other end to the model drive rod. The manometers are attached to the test section just above the pitching mechanism. This places the manometers as close to the model as possible while remaining outside of the tunnel itself; this minimizes the necessary length of tubing needed from the model pressure taps to the manometers. Pressure lines run from the model and the pitot-static tube (located upstream of the model) to the manometers. Four analog output cables are then connected from the manometers and the displacement transducer to the A/D board of the data acquisition computer (one from the displacement transducer, one from the freestream manometer, and two from the two unsteady pressure manometers). This A/D board is connected directly to the computer; the PDP 11/23 houses both the A/D board and the disk drives. An auxiliary line can then be run from the 11/23 to a plotter for online plotting capability.

The motor controller, clutch controller, motor rpm readout, and power supply for the displacement transducer are all located on a shelf attached to the test section beneath the level of the pitching mechanism base.

3.2 Location Of Pressure Transducers

During the model design stage of the research, a decision had to be made whether to mount the pressure transducers directly to the pressure taps inside the delta wing model, or to mount them outside of the tunnel and attach

them to the pressure taps by plastic tubing. The primary advantage of using directly mounted transducers is that the pressures are measured directly, without any amplitude attenuation or phase shift due to the length of tubing. This alteration of the pressure signal due to the tubing is also the primary disadvantage of using remote transducers. However, there are other factors to consider that weigh in favor of using transducers mounted outside of the tunnel.

One such factor is the cost of the transducers. Considering the relatively low pressure differences that are to be resolved, it is necessary to use a transducer with as low a range as possible (to obtain the best resolution possible). In general, low range transducers are larger pieces of equipment than high range transducers (a larger sensing element is necessary to resolve lower pressures). Hence an interior mounted transducer would need to be small enough to fit in roughly a 1/2" gap; yet have a very low range, roughly 0-5 inches of water. Pressure transducers that fit both of these requirements were found to be prohibitively expensive.

To further complicate this, the ability to move the transducer has to be considered. There are two options available for taking measurements at several different locations on the wing. First, a small number of transducers can be used, and subsequently moved to each location between tests; or enough transducers can be used so that there is one for each tap. Here again the cost is a factor: purchasing enough transducers for each tap is prohibitively expensive. However, attempting to physically move the transducer between tests involves a risk of damaging the unit, and becomes very time consuming.

An additional consideration when using direct mounted transducers involves the calculation of the pressure coefficient. In order to most conveniently obtain the pressure coefficient as it is typically defined (a complete discussion of this topic can be found in the following section), it would be

necessary to attach the the reference port of the transducer to the freestream total pressure. Since a direct mounted transducer would have this reference port open to the air in the model cavity (at an unknown pressure), it would be necessary to run a pressure line into the model to attach to that port.

The tests conducted during this research involved low pitching rates, up to 2.1 Hz. Considering the low frequency of the pressure signal, as well as to avoid the above problems, it was decided to mount the pressure transducers outside of the test section, with plastic tubing connecting them to the pressure taps on the model. Thus it was necessary to evaluate the effect of the tubing on the unsteady pressures. To this end, a preliminary experiment was performed using the pressure transducers and tubing later used to obtain the unsteady pressures.

A schematic of this experimental set-up is shown in Figure 3.2. Two pressure transducers were mounted on one end of a cylindrical chamber; one flush with the surface of the chamber and one connected to the chamber by a length of plastic tubing. The opposite end of the chamber was a flexible diaphragm that was driven by a modal exciter in a pseudo-random manner, creating pressure fluctuations within the sealed chamber. Thus, the transducer mounted flush against the chamber registered these fluctuations, while the other transducer registered pressure fluctuations that were attenuated and phase shifted due to the tubing. By comparing the two signals, the specific effect due to the tubing could be determined.

Specifically, this was accomplished by using a Scientific Atlanta Spectral Dynamics SD380 Signal Analyzer. By using the flush-mounted transducer as the "input", and the remote mounted transducer as the "output", the transfer function due to the tubing was calculated.

Two separate tests were conducted. First, the tubing to be connected to the model pressure taps was tested with the two high range manometers. This tubing was 36" long with an inner diameter of 1/16". Next, the low range manometers were used with the tubing connected to the pitot-static tube. This tubing was 48" long with an inner diameter of 0.25". The effect on both the fluctuating port pressure and the fluctuating freestream pressure were evaluated. Each test was conducted in the following manner. A pseudo-random input would be applied to the shaking mechanism, generating a fluctuating pressure. One hundred sets of the frequency spectrum of the transducer outputs was then recorded. These one hundred sets were averaged to give an average frequency response. The transfer function and phase shift were then obtained from the two output spectra. This was done for frequency ranges of 100 Hz and 20 Hz. The two 100 Hz range cases are shown in Figures 3.3 and 3.4. These figures are for the high range manometers (surface pressures) and the low range range manometers (freestream dynamic pressure), respectively. The 20 Hz experiments were then conducted to yield better resolution at the low frequencies.

Figure 3.3 shows the phase shift on the top half and the transfer function on the bottom half. The phase shift is plotted in degrees as a function of signal frequency. The transfer function is presented as a semi-log plot of voltage ratio (output divided by input) as a function of signal frequency. Figure 3.4 is arranged in a similar manner. Each of these plots begins at zero frequency with a unit voltage ratio and zero phase shift as would be expected. The lower resolution of the high range manometers can be seen by the smoothness of the curve in Figure 3.3 as compared to Figure 3.4.

Figure 3.3 (high range manometers) shows a trend of a gradually increasing voltage ratio followed by a decrease. Figure 3.3 indicates that the

tubing behaves like a second order system. At 20 Hz, the signal has been somewhat amplified, but is still within 5% of the original value. The phase shift at this point is roughly -23° . The signal amplification peaks near 40 Hz with a 40% increase in the signal. The signal ratio then decreases to approximately a 65% reduction of the original strength at a frequency of 100 Hz. Thus, for the tubing used to measure the model pressure taps, the original signal retains 95% of its magnitude for frequencies up to 20 Hz. For frequencies up to only 10 Hz, the signal retains 99% of its magnitude, with a phase shift of -10° .

Figure 3.4 shows the transfer function and phase plot for the tubing connected to the pitot-static tube. Again, it can be seen that the tubing behaves like a second order system. LeMay (1988) examined the freestream response to a periodic motion of a delta wing of geometry similar to the current wing, and found velocity fluctuations less than 1% of the freestream velocity. However, considering that the dynamic pressure is necessary to calculate the pressure coefficient (for a more complete explanation of this subject see the following section on pressure coefficients), the amplitude attenuation and phase shift of the tubing were examined. The freestream dynamic pressure was measured with the low range manometers. The irregularity of the curve as compared to Figure 3.3 can be attributed in part to the higher resolution available from the lower range manometers. A different size and length of tubing was used for the pitot-static tube than was used for the delta wing pressure taps; this is reflected in the difference in curve shape between Figure 3.3 and Figure 3.4. Figure 3.4 shows a substantial amplification of the pressure signal at about 37 Hz. This point is apparently the resonance frequency of the system. The amplification subsides beyond this point, but then begins increasing again at a lesser rate. Over most of the frequency range the signal ratio is greater than 1; the signal is being amplified rather than attenuated as in Figure 3.3. This is primarily due to

the difference in tubing length and diameter. By 20 Hz the signal has been amplified by roughly 60%; only frequencies below 11 Hz retain at least 95% of their original magnitude (with a $+10^\circ$ phase shift).

To compare the two cases, the model pressure line retains 95% of its magnitude for frequencies up to 20 Hz, with a phase shift up to -23° (lag of 0.064 cycles). For the dynamic pressure line, these values are 11 Hz and $+10^\circ$ (lead of 0.028 cycles). This information can now be applied to the problem of the oscillating delta wing and the corresponding fluctuating pressures. The pitching frequencies utilized during this research vary from 0.35-2.10 Hz. LeMay (1988) found that for velocities from 10-40 ft/s the freestream responds to the sinusoidal model motion (and thus varying blockage) in a similarly sinusoidal manner; at frequencies very near the pitching frequency and at fluctuations up to 1% of the freestream.

Using the transfer function for the connecting tubing, it is possible to correct the unsteady pressure data for the effect of the tubing. The data is recorded in the form of pressure as a function of time. This data could then be transformed into the frequency domain (amplitude as a function of frequency), where the appropriate amplitude ratio could be applied (from the known transfer function). The data could then be transformed back into the time domain; resulting in corrected data. However, for the first analysis of the unsteady pressure data, these steps have not been taken. The ramifications of neglecting the tubing effects is detailed in the following section on error analysis and accuracy.

As a side note, it should be mentioned that this type of transfer function analysis assumes that both transducers are subjected to the same pressure; that is, that the two pressure taps drilled in the test chamber surface are

subjected to equal pressures. Since the pressure fluctuations are generated by a diaphragm and not a piston, the possibility of a nonuniform pressure field exists. However, the pressure was measured at several positions on the end of the chamber and found to be equivalent. This is most likely due to the small amplitude and random nature of the pressure fluctuations used during this testing.

In addition, it is assumed that the two transducers used to measure the pressures are in phase with each other, and that no phase difference would have existed had both transducers been placed directly on the test chamber (with no tubing). However, such a difference would have been included in the phase difference found for the tubing. As such, it would also have been neglected.

3.3 Obtaining Pressure Data

3.3.1 Pressures Recorded

During a given experiment, four variables were recorded; the displacement transducer reading and three pressure readings. One of these pressures was the freestream dynamic pressure; the other two were unsteady pressures taken from the delta wing model pressure taps. For the freestream manometer, the static pressure line from the pitot-static tube was connected to the reference pressure port of the manometer. The total pressure line from the pitot-static tube was then connected to the positive pressure port of the manometer. This resulted in positive dynamic pressures.

For the two model manometers, the reference pressure port was connected to the total pressure from the pitot-static tube. A four-way pressure manifold attached to the stagnation part of the pitot-static tube allowed the total pressure to be run to all three of the manometers. The positive pressure port on each of the two model manometers was then connected to a pressure tap on the model surface (the static pressure on the surface of the model). This resulted in positive pressure differences being recorded, and facilitated the conversion from a pressure value to a pressure coefficient (this topic is discussed in more detail in the following section). Since there were two manometers available for the model pressure taps, two pressures could be recorded simultaneously.

Throughout the tests conducted, one of these manometer was devoted to recording the pressure at the same tap each time. Since there are twelve pressure taps located along the model surface, it required several tests to obtain a complete profile. As a check to ensure that the flow conditions were the same during each test, the pressure at one specific tap was monitored each time. The tap used as this reference points was at the 90% chord location, on the right side of the model centerline.

Hence a given experiment would proceed as follows. First, a preliminary test would be conducted to find the magnitude of the pressures to be recorded so that the appropriate A/D gain code could be chosen. Then the test conditions such as atmospheric pressure, temperature, freestream velocity, and pitch rate would be recorded. The delta wing model would then be set at zero yaw angle (this was measured relative to the vertical side of the wind tunnel). The first test would then measure the following instantaneous quantities: angle of attack (displacement transducer), freestream dynamic pressure, the unsteady pressure at the reference tap (90% chord), and the unsteady pressure at the first

point of the profile, say the 35% chord position. For the second test, the pressure line from the 35% tap would be replaced with the line from the 40% tap, which would then be replaced by the line from the 45% tap, and so on until all twelve of the taps had been sampled. For each test, the pressure at the 90% tap was recorded; any large deviation of this pressure between tests was an indication that there was a difference in the flow conditions (i.e., freestream velocity had changed). For a given profile of the twelve chord positions (at a given freestream velocity and pitch rate), it is necessary for the flow conditions to remain the same. Thus by using one manometer to continually measure the same point, the freestream condition could be monitored between tests.

Unsteady pressure measurements were taken for several Reynolds numbers and several pitch rates. For a given set of flow conditions, one profile was recorded, where a profile consists of the pressures recorded at all twelve of the pressure taps (from 35-90% of the root chord on the left side of the model centerline). The pitching motion ranged from 29-40° for all of the cases. In addition, 50 sets of pressures measurements were taken for 1.1 cycles of motion (one cycle consisting of both the pitch-up and pitch-down motion). These 50 sets of data were then ensemble averaged to yield one set of data covering 1.1 cycles of motion. Each of these sets consists of 50 points; the frequency rate of data sampling was always such that fifty points were taken over 1.1 cycles of motion, regardless of the specific pitch rate.

In addition, pressures were taken at static angles of attack to be used as a comparison to the unsteady pressures. The procedure for obtaining the static pressure data was the same as for the unsteady data acquisition. The A/D sampling rate was kept the same between static and dynamic cases. However, the model was held at a constant angle of attack as the pressure data was

recorded. This information can then be used to compare not only to the unsteady pressures, but also to the static pressures obtain by previous delta wing studies.

Typically, research involving an oscillating motion uses a quantity known as the reduced frequency to describe the unsteadiness. In this type of research, the non-dimensional reduced frequency is often denoted by k , where k is a function of the pitching frequency, the freestream velocity, and the root chord length. The reduced frequency is similar to the Strouhal number, and is defined as :

$$k = 2\pi fc / U_{\infty} \quad (1)$$

During this research, tests were conducted at freestream velocities of 10, 20, 30, 40, 50, and 60 ft/s (3.05, 6.10, 9.04, 12.09, 15.14, and 18.19 m/s). Using the root chord, these velocities correspond to a Reynolds number range of 250,000-500,000. Values of the reduced frequency varied from $k=0.10$ to $k=0.50$. However, at the lower speeds, the pressures were so low that the electronic manometers could not resolve the fluctuating pressures without a substantial amount of noise in the signal. This occurred most notably in the 10 and 20 ft/s cases. As a result, this data was not used in the final analysis. Table 1 shows a matrix of the twelve cases that provided meaningful data, and were thus used. Freestream velocities of 30-60 ft/s and reduced frequencies of 0.10-0.30 were used as the primary data for this analysis. Table 2 shows the static cases. Static data was taken at the same four freestream velocities used for the unsteady measurements. At each of these freestream velocities, three angles of

attack were used, corresponding to the low, middle, and high end of the range of travel. Thus, 29, 34, and 39° angle of attack were examined.

3.3.2 Conversion To Pressure Coefficient

In order to examine the pressure data in a more convenient form the raw pressures obtained during testing were converted to pressure coefficients. The standard definition for pressure coefficient is :

$$C_p = (P_{tap} - P_{\infty}) / Q_{\infty} \quad (2)$$

The following substitution is then made :

$$Q_{\infty} = P_o - P_{\infty} \quad (3)$$

Upon making some algebraic manipulations, equation (2) can be reorganized to yield the following equation :

$$C_p = 1 - (P_o - P_{tap}) / (P_o - P_{\infty}) \quad (4)$$

This is the equation used to calculate the pressure coefficients throughout this research due to its convenience. The denominator term, $(P_o - P_{\infty})$, is obtained directly from the freestream manometer. Due to the use of the four-way pressure manifold to redirect the freestream total pressure, the

numerator term ($P_o - P_{tap}$) is obtained directly from each of the two model manometers.

It is important to note that the total atmospheric pressure, P_{atm} , cannot necessarily be used in place of the total freestream pressure, P_o . This substitution typically simplifies the experimental set-up and data acquisition, and can be found in pressure research using indraft wind tunnels. The problem stems from a total pressure loss that occurs through the wind tunnel anti-turbulence screens, resulting in the P_{atm} and P_o being different. Thus a calibration of the tunnel pressure loss over the specific velocity range would be necessary. Such a calibration is shown in Figure 3.5 in the interest of completeness. This data was taken with the wind tunnel used throughout this research. Figure 3.5 contains three curves: $P_o - P_{\infty}$; $P_{atm} - P_o$; and $P_{atm} - P_{\infty}$. These curves are all plotted as pressure (in psi) as a function of freestream velocity from 10-40 ft/s. The first curve, $P_o - P_{\infty}$, is the freestream dynamic pressure, measured directly from the pitot-static tube and typically used to indicate freestream velocity. The second quantity, $P_{atm} - P_o$, is the total pressure loss through the inlet screens. At atmospheric conditions, or without any pressure loss, P_{atm} and P_o are the same. From 10 ft/s to 40 ft/s, the difference ranges from 20% of the freestream dynamic pressure to roughly 9%. This difference is reflected in the third curve, $P_{atm} - P_{\infty}$. By using this quantity as the denominator of Equation [4], and hence neglecting the pressure loss, an error could be introduced. From Figure 3.5 it can be seen that this quantity is consistently larger than $P_o - P_{\infty}$. This will result in a consistently smaller pressure coefficient magnitude.

If for a low speed, open circuit wind tunnel the pressure loss through the screens (and associated pressure drop) was neglected, the freestream dynamic

pressure Q_∞ would be replaced by $P_{atm} - P_\infty$ (see Equation [3]). This quantity would be measured by leaving the reference pressure port of the model manometer open to the atmosphere. However, by connecting the total freestream pressure line to this port (as has been done in this research), the pressure coefficient can be measured directly without regard to the screen pressure loss.

3.3.3 Correspondence To Vortex Breakdown Location

Considering the dramatic effect that vortex breakdown has on the flow characteristics of a delta wing, it would be interesting to determine the effect of vortex breakdown on the fluctuating pressure field above the wing. Specifically, a correlation between the instantaneous location of vortex breakdown and the fluctuation of the pressure field is of interest. This was the reasoning behind the location of the pressure taps. LeMay (1988) published some information concerning the spanwise location of the vortex. From flow visualization he found that the vortex core was located at approximately 60% of the local semi-span. Considering the similarities in the delta wing models and the test parameters, this position was used as the location for the pressure taps of the current study. The existence of the vortex core at 60% semi-span was also noted by McKernan (1983), due to the presence of a static pressure peak at that location. As for the angle of attack range of this study, 29-40°, it was chosen for two reasons. First, LeMay found that the vortex breakdown was over the wing throughout this range; and second, this was the range used by LeMay during his tests on chordwise breakdown position.

By recording the output of the displacement transducer, the instantaneous angle of attack is recorded through a pitching cycle. By using LeMay's results, this angle of attack can be used to estimate the chordwise breakdown position, for a given Reynolds number and pitch rate. Thus as the unsteady pressure data is examined, it is also possible to estimate the location of breakdown, and thus it may be possible to explain some of the characteristics of the pressure field by the characteristics of the vortex breakdown.

3.4 Ensemble Averaging

For a test at a given chord location, fifty points were sampled over 1.1 cycles of motion. This number of data points was chosen to provide sufficient temporal resolution of the unsteady pressures. This was then repeated fifty times, so that fifty sets of fifty points was obtained. These fifty sets of data were then ensemble averaged. That is, the first points of each data set were averaged together separately, then the second points of set were averaged, and so on. This was possible because for each data set the sampling was begun at the same angle of attack. For each test, the displacement transducer was sampled until a value corresponding to 33.5° angle of attack was obtained. At this point, the sampling of the unsteady pressures was triggered. Furthermore, sampling was only initiated if the model was on the downstroke as it passed through 34° angle of attack. This process of sampling the displacement transducer and triggering data acquisition was controlled by the data acquisition software.

The sampling rate was chosen for each test such that the fifty points spanned over 1.1 cycles of model motion. For a given test, the freestream velocity and reduced frequency were held constant. By using Equation [1] (see section 3.3.1), the pitching frequency can be calculated. This was then used to determine the sampling rate necessary to obtain fifty points over 1.1 pitching cycles.

3.5 Accuracy and Error Analysis

In order to estimate the effect of neglecting the connecting tubing on the fluctuating pressure signal, a Discrete Fourier Transform (DFT) was performed on several of the data sets to determine the frequency content of the signal. This procedure was hampered by the relatively small number of points (50) available for each data set. Typically when the spectral content of a signal is to be examined, the number of data points is much larger; on the order of thousands. This allows for a much higher frequency resolution. Furthermore, the sampling rate during data acquisition was set so that the fifty points would span over 1.1 cycles of motion; this sampling rate then determines the frequency range over which the DFT could be performed. A DFT was performed on three of the data sets; one each at the lowest and the highest pitching frequency, and one at a frequency in between. For all three of the trials, the data set from the 35% chord location was chosen due to its typically having one of the largest signal strengths of all twelve of the chord locations. The resulting frequency spectrum for the highest frequency (pitching rate of 2.1 Hz) is shown in Figure 3.6. This figure shows power spectrum as a function of frequency. The sampling rate for this data set was 95.43 Hz; hence the

frequency spectrum extends up to the Nyquist frequency (the highest frequency that a given sampling rate can resolve), 47.7 Hz. Figure 3.6 shows that the dominant frequency of the signal is near the pitching frequency. The remaining frequency content is at a much smaller amplitude. This general trend was also apparent in the other two sets of DFT data.

With this in mind, for this initial analysis of the pressure data the effect of the connecting tubing was neglected. Considering that throughout the pitching frequency range tested (0.35-2.10 Hz) the amplitude modification is within a few percent for both the freestream pressure and the wing surface pressure, such an assumption seems appropriate. In addition, the phase shift of the pressures was also small. The tests were conducted by taking fifty points over 1.1 cycles, resulting in 0.022 cycles between data points. In terms of degrees of model motion, the amount between data points changed through the pitching motion. Table 4 shows the angle of attack for each of the fifty data points. These fifty points are the same for each of the tests conducted. Near the endpoints of the model motion (i.e., 29° or 40°), there is roughly a 0.05° change in angle of attack between data points. However, near the middle there is roughly 0.75° between data points. For most of the pressure frequencies encountered, the phase shift was less than this amount. At the highest pitch rate of 2.1 Hz, the phase shift for both the freestream pressure and the model pressure is roughly 0.007 cycles (with the freestream pressure leading and the model pressure lagging). The amplitude ratio and phase shift are even smaller for the lower pitching frequencies. Certainly, by neglecting the tubing effects an added measure of uncertainty is included, but not one that is large compared to the magnitude of the other uncertainties.

An additional source of error was created by the testing procedure. Since each of the twelve pressure taps was monitored individually, a pressure line had to be connected to each pressure tap. Two options were available to provide pressure lines to all twelve taps: twelve separate lines could be strung from the model to the transducers, or one line could be used and alternately connected to each pressure port. The advantage of using twelve lines is that the model does not need to be disturbed between tests, in order to switch pressure taps. However, using twelve pressure lines creates the hazard of crimping or tangling the tubes, as well as creating a large bundle of tubes running down the sting from the model to the transducers. The hollow cavity inside the delta wing has a limited amount of space; fitting twelve plastic pressure tubes inside it could result in some of the tubes being crimped or pinched off. To avoid this, while still providing some of the convenience of having more than one pressure tap attached, four pressure lines were connected to the model. One was used at the reference port, while the other three were connected to the pressure ports to be sampled. By switching these three, all twelve ports could be sampled by rearranging the pressure lines four times.

Unfortunately, this required that the wind tunnel be opened during a test. Thus for a specific test (i.e., constant freestream velocity and reduced frequency), three chord locations could be sampled, then the pressure lines had to be reconfigured by opening the delta wing model and reattaching the tubes to three new taps. Throughout this operation, both the tunnel speed and the wing alignment remained constant. However, by opening the test section to the atmosphere, the flow condition is altered. Upon closing the section, roughly five minutes was allowed for the flow to reach a steady state once again. This amount of time was determined during a previous flow visualization study to be

of sufficient duration (Thompson et al, 1989). In addition, a different group of three chord locations was sampled each time. For example, for one test the chord locations may have been sampled in the following groups of three: 35,40,45%; 50,55,60%, 65,70,75%, and 80,85,90%. Then for the next test they may have been grouped like so: 35,60,65%, 40,45,50%, 55,85,90%, 70,75,80%. To aid in the convenience of the testing procedure, the order that the twelve chord locations were sampled was not constant.

As a means of checking the flow condition between tests (and reconfiguration of the pressure lines), one pressure tap was monitored throughout each experiment. For a given freestream velocity and reduced frequency, the pressure distribution recorded at this tap should be the same as each of the other twelve taps were sampled. This was typically the case; the scatter of the pressure from this reference tap during each test was typically small. A more complete discussion of this can be found in section 4.5.2.

During each test, the pressures are sampled through fifty cycles of periodic motion. These cycles are then ensemble averaged to yield the pressure distribution for one cycle of motion. The standard deviation of the fifty cycles can be calculated during the ensemble averaging. Table 3 shows the standard deviations for each of the static tests and each of the dynamic tests. A standard deviation can be calculated for each of the chord locations; the numbers in Table 3 represent the average standard deviation for all twelve of the chord locations.

For the static tests, the standard deviation ranges from 0.0128-0.1177 psi. The maximum standard deviation of 0.1177 psi occurs for a freestream velocity of 60 ft/s and an angle of attack of 39°. For the dynamic tests, the

standard deviations range from 0.0366-0.1446. The maximum occurs at a freestream velocity of 60 ft/s and a reduced frequency of 0.20. In general, the standard deviation seems to increase with the freestream velocity, but does not show a consistent trend relative to the reduced frequency. This increase with freestream velocity could be due to the increase in absolute pressure over the wing as the velocity increases.

The uncertainty analysis method of Kline (1985) can be used to estimate the uncertainty in the pressure coefficient. This method involves estimating the uncertainty of each variable and then combining them; this process is known as propagation of uncertainty. First, the governing equation (in this case the definition of pressure coefficient, Equation [4]) is differentiated with respect to each variable in the equation. Looking at Equation [4], two variables exist: $(P_o - P_{tap})$ and $(P_o - P_\infty)$. Since each of these is measured as a single quantity, each is considered a separate variable, rather than using P_o , P_{tap} , and P_∞ all as separate variables. Next, these partial differentials are multiplied by the estimate of the uncertainty for that variable. These quantities are then squared and summed. The square root of this quantity is the total uncertainty in the measurement. By using this method with the equation for pressure coefficient, Equation [4], the following equation can be derived for the uncertainty in the pressure coefficient :

$$W = \{ 0.0001 (C_p^2 - 2C_p + 2) / (P_o - P_\infty)^2 \}^{1/2} \quad (5)$$

This equation gives an absolute value for the uncertainty, not a percentage. In addition, Equation [5] is derived by assuming an uncertainty of 0.01 inches of water in the pressure measurements, which is a slight

overestimation. This value is the uncertainty of the electronic manometers. Furthermore, the units of the dynamic pressure should be inches of water; this yields a non-dimensional value for W (since the factor of 0.0001 has units of inches of water squared).

From Equation [5] it can be seen that the magnitude of the uncertainty increases with increasing pressure coefficient. However, by dividing through by the pressure coefficient, it can be seen that the percent uncertainty decreases with increasing pressure coefficient, as would be expected. Appendix A contains a table of the uncertainty in pressure coefficient for each of the twelve cases tested during this research. The largest percent uncertainty is 10.9%, while the smallest is 1.6%. As the Reynolds number increases the pressure increases, yielding a smaller percent uncertainty, as can be seen from the table in Appendix A.

IV. EXPERIMENTAL RESULTS

4.1 Overview

The results will be presented in the following manner. First, a discussion of the unsteady model motion and the response of the freestream flow to the oscillation of the model. Then the static data will be presented and compared to pressure distributions presented in earlier research. Then the unsteady pressure data will be presented and discussed. This data consists of the unsteady pressures taken at the four freestream velocities and three reduced frequencies. Following this is a brief discussion of additional pressure data taken during the course of this research. This includes the data taken from pressure taps located on the right side of the model centerline. It should be noted that, considering that the pressure coefficient is a typically negative quantity on the suction side of the wing, it will be discussed in terms of the magnitude and not the actual value. Hence an increasing pressure coefficient is becoming more negative.

4.2 Model Motion And Freestream Response

The performance of the unsteady pitching mechanism and the resulting model motion was examined by LeMay (1988) to determine the amplitude and percent harmonic distortion. LeMay also examined the effect of the model motion, and thus the variation in tunnel blockage, on the freestream flow. Both freestream velocity fluctuations and phase shift between model motion and freestream velocity were examined. These results are summarized here since the same pitching mechanism was utilized. However, the delta wing model used by LeMay was 0.5" thick, while the current study used a 0.75" thick wing.

LeMay used the same displacement transducer and hot-wire anemometry to obtain information on the instantaneous model position as a function of velocity and reduced frequency. Performing a discrete Fourier transform on this data, he was able to find the dominant frequencies of the motion and the amount of harmonic distortion. For a velocity of 40 ft/s and a reduced frequency of 0.20, the resulting harmonic distortion in the sinusoidal model motion was 2.08%.

To ascertain the effect of the model motion on the freestream velocity, LeMay used hot-wire anemometry in addition to the displacement transducer to record instantaneous freestream velocity as a function of model motion. In general, LeMay found that the magnitude of the velocity fluctuations was relatively small, and that it oscillated in a manner similar to the oscillation of the model. The largest fluctuation was found to be 0.5% of the average velocity, and this occurred for a velocity of 30 ft/s and a reduced frequency of 0.05. In general, it was seen that the velocity fluctuations decreased with increasing pitch rate. However, the phase lag increased with reduced frequency. The

phase lag ranged from 13.4° (for the above case) to 50.1° (for 30 ft/s and $k = 0.30$).

During the current research, some of the tests, particularly those at the lower pitch rates, took over an hour to complete. Over such a length of time, the possibility exists of the freestream velocity drifting. For all the tests in this study, the freestream velocity was held within 1.5% of the nominal value. This is a small enough amount that any drift of the freestream velocity was considered negligible. Furthermore, different tests were to be conducted at the same freestream velocity (for example, tests at 30 ft/s with reduced frequencies of $k = 0.10$ and 0.20). Between such tests, the wind tunnel could be set to within 2% of a given freestream velocity. For the Reynolds numbers ranged tested here, this corresponds to being able to set the Reynolds number within 10,000 of a given value.

4.3 Static Pressure Data

Static pressure data was recorded for three angles of attack and four Reynolds numbers. This data was taken to be used as a basis for comparison with the unsteady pressure data, as well as to compare with previous studies involving static delta wing pressure profiles. The four Reynolds numbers tested are the same used during the unsteady testing. The three angles of attack correspond to the low, mid-, and high end of the range of motion during the unsteady testing. Thus, Reynolds numbers of 250,000, 335,000, 420,000, and 500,000 were tested; at angles of attack of 29, 34, and 39 degrees. Table 2

contains a list of the static tests performed. The static data is presented in Figures 4.1-4.4. This data is also presented in tabular form in Appendix B for convenience. As with the unsteady pressures, the static pressure profiles consist of measurements from twelve chord locations from 35-90% along a 60% semi-span ray.

Figure 4.1 contains the static pressure at a Reynolds number of 250,000 (freestream velocity of 30 ft/s). Pressure coefficient is plotted as a function of chordwise location (x/c) for the three specified angles of attack. The static location of the vortex breakdown (from LeMay, 1988) is represented on each of the three curves by a vertical line. In addition, an error bands are shown on Figure 4.1. This error represents the uncertainty in the pressure coefficient, calculated by a method described by Kline (1985). These uncertainties can be found in tabular form in Appendix A. A discussion of this is included in section 3.5.

For each of the three curves in Figure 4.1, the pressure coefficient increases from 35% x/c to 45%, then decreases to 90%. As the angle of attack is increased from 29° to 39° , the curve maintains the same general shape with an increase in the pressure coefficient. As would be expected, an increase in angle of attack results in a increase in pressure coefficient. Also, the pressure coefficient is higher near the apex of the wing due to the increase in strength of the vortex core (the core rotational velocity is higher, and thus a lower pressure is generated). The effect of the vortex breakdown is not readily apparent from this figure; its effect on the pressure coefficient distribution along this ray appears to be negligible.

Figure 4.2 shows trends similar to Figure 4.1. Figure 4.2 contains the static pressure profiles for a Reynolds number 335,000 (40 ft/s). As with Figure 4.1, an uncertainty estimate is shown on the 35% data points. The uncertainty

at the 90% data points is less than the size of the symbol used on the figure. The 29° curve is very similar to that of Figure 4.1. And as in Figure 4.1, as the angle of attack is increased the magnitude of the pressure coefficients increases. The peak pressure coefficient for this case is slightly higher than for the 30 ft/s case. At 30 ft/s the 45% location has a coefficient of -4.03; at 40 ft/s this value is -4.67. Again, the vortex breakdown location is indicated, and appears to have little effect on the pressure profiles. Figures 4.1 and 4.2 also show a decrease in the pressure coefficient forward of the 45% location.

The drop in pressure coefficient is probably due in part to the location of the pressure taps. Due to the width of the bevel on the model (the model is beveled on both upper and lower surfaces), the 40% tap lies directly on the edge of the bevel and the top surface, while the 35% tap lies on the face of the bevel itself. Certainly the presence of the bevel is influencing the pressure field in some manner.

Figures 4.3 and 4.4 show the 50 ft/s and 60 ft/s cases, respectively. In each of these figures, the 29° and 34° curves are similar to the those at the two lower speeds. Both the shape of the curve (peaking at the 45% location) and the magnitude of the pressure coefficients are similar. However, at these two higher speeds, the pressure coefficients drop drastically as the angle of attack is further increased to 39°. In both Figure 4.3 and Figure 4.4, the 39° curve lies consistently below the 29° curve. This overall decrease in pressure coefficient indicates the possibility of a decrease in lift over the wing at this angle of attack. This fact in itself is not unusual; delta wings typically stall at such an angle of attack. The interesting point is that the pressure distribution did not decrease by 39° below 40 ft/s; but it did above 50 ft/s.

This could possibly be due to the testing procedure. When the static data was taken, the Reynolds number was held constant and the angle of attack was

varied. To examine this anomaly, selected static experiments were repeated. The same testing procedure was used; however, only four pressure taps were monitored, those at 45, 50, 55, and 75% x/c . The results from the 50 and 60 ft/s cases were very close to the first set of data. The values fall within 6.0% of the first set of data. However, the two low speed cases have larger discrepancies. At 29° angle of attack, both the 30 and 40 ft/s cases agree within 6-7% of the previous static data. However, for higher angle of attack, the difference is much more significant. In the first trial, the pressure coefficient increased with increasing angle of attack. During the second trial, the pressure coefficient remained roughly constant from 29-34°, and then decreased as the angle of attack increased to 39°. This indicates that at 39° angle of attack the pressure distribution had decreased for four freestream velocities during the second trial.

The fact that the previous 39° data at 30 and 40 ft/s indicates higher pressure coefficients is difficult to explain. McKernan (1983) noticed a decrease in pressure coefficient for a 70° sweep delta wing at 30 ft/s between 35 and 45 degrees angle of attack. It is possible that a static hysteresis in the breakdown location affects the flow over the wing in such a way that a decrease in pressure can be postponed to 39° or beyond. LeMay (1988) noted such an effect, but only at lower angles of attack 28-30°. An investigation with an 80° sweep delta wing by Arena (1989) noted that at an angle of attack of 40° there are two possible steady state flow conditions, one where vortex breakdown has occurred, and one where it has not occurred. It is possible that some similar type of static hysteresis is responsible for the difference in the decrease in pressure seen at 30 and 40 ft/s. In addition, a full distribution of pressures was not obtained during the second set of static tests. Only four of the twelve taps were monitored.

Figure 4.5 shows these static pressure coefficients compared to two other

studies. These two studies are McKernan (1983) and Visser (1989). Upon reviewing McKernan's literature it appears that the total pressure loss through the wind tunnel screens (see section 3.3.2) was not taken into account, thus his data has been corrected in Figure 4.5. All of these measurements were taken with a 70° sweep, 16 inch root chord delta wing at roughly 35° angle of attack and a Reynolds number of 225-250,000; however, wings of different thickness were used. The measurements were all taken at 60% of the local semi-span. Again, the effect of locating pressure taps on the bevel can be seen in Figure 4.5 by the difference of the curve slope near the leading edge. The measurements taken by Visser show the same magnitude of pressure coefficient, but McKernan's values are lower overall. Other differences in the curves can be attributed to differences in wing thickness, differences in bevel angle, and unsteadiness of the vortex flow.

4.4 Unsteady Pressure Data

Table 1 shows the unsteady pressure tests conducted. The angle of attack range used was consistently 29-40°. Twelve data sets comprise the bulk of the data; four Reynolds numbers with three reduced frequencies. There are three important quantities in each data set: pressure coefficient, chord location, and angle of attack. Hence a convenient way to present the data is in three-dimensional form. The pressure coefficient can then be displayed as a function of both chord location and oscillating angle of attack.

Each data set composes 1.1 cycles of motion, where one cycle consists of a pitch-up and a pitch-down maneuver. The pitching maneuver for each data

set is identical. The wing begins at 34.5° , pitches down to 29° , up to 40° , then down to roughly 32° (for 1.1 cycles). A schematic of this pitching maneuver is shown in Figure 4.6.

The twelve sets of data are presented in Figures 4.7-4.18. Figures 4.7-4.9 are for the 30 ft/s case, at reduced frequencies of 0.10, 0.20, and 0.30 respectively. Figures 4.10-4.12 are for the 40 ft/s cases at these same three reduced frequencies. Similarly, Figures 4.13-4.15 are for the 50 ft/s cases; and Figures 4.16-4.18 are for the 60 ft/s cases. Each of these figures is a plot of the pressure coefficient for a constant reduced frequency. These plots are organized with the pressure coefficient along the positive y-axis, the chord location along the positive x-axis, and the cycles of motion along the negative z-axis. A table with the instantaneous angle of attack throughout the pitching cycle is contained in Table 4. Since each data set spans 1.1 cycles of motion in fifty increments; this can be converted to instantaneous angle of attack with Table 4. Lines of constant chord location are also drawn on the pressure coefficient plots to help clarify the trends. These lines run roughly parallel to the cycles axis. In addition, the approximate location of vortex breakdown has been superimposed on the pressure coefficient plots.

LeMay (1988) obtained data on the dynamic location of the vortex breakdown at various reduced frequencies. He also found that the hysteresis loop of the breakdown position became larger with increasing reduced frequency. In addition, he found that the size of the hysteresis loop was relatively insensitive to a change in Reynolds number. Thus by using his data at the three reduced frequencies of 0.10, 0.20, and 0.30 (and for the same angle of attack range), the location of the vortex breakdown has been included in Figures 4.7-4.18. LeMay's data contains chordwise breakdown location as

function of instantaneous angle of attack for a given reduced frequency. By using this information in addition to the instantaneous angle of attack for the current data sets (see Table 4), the vortex breakdown through each cycle can be computed. For angles of attack in between LeMay's data points, the breakdown location has been linearly interpolated. Then, for each of the fifty incremental angles of attack, the corresponding chord location of breakdown has been marked on the pressure coefficient curve. These fifty points are then connected, resulting in the sinusoidal line drawn across Figures 4.7-4.18. This line does not denote a pressure coefficient; it is merely drawn to represent the chord location of vortex breakdown at that instantaneous angle of attack.

4.4.1 Tests at Reynolds Number 250,000

In Figure 4.7, the magnitude of the pressure coefficient increases with decreasing distance from the apex of the model. From the 90% location to the 60% location, the increase is approximately linear. However, there is a larger jump to the 50-55% locations, which have close values. An increase then occurs up to the 35% location. This type of behavior is expected, as the leading edge vortex is closer to the wing surface at the forward positions. The similarity of the pressure coefficients at 50% and 55% is not as easily explained, nor is the change in slope of the curve from the front half of the wing to the rear half. The leveling out of the curve forward of the 45% location may be the result of the placement of the pressure taps on the bevel.

The shape of this curve is consistent throughout the three $Re = 225,000$ cases (Figures 4.7-4.9). The linearity of the pressure coefficients from 90-60%,

the similarity of the the 50% and 55% locations, the increase forward of 50%, and the effect of the bevel on the 35% and 40% coefficients are all characteristics seen for all three reduced frequencies. In addition, the magnitude of the data is similar between these three cases.

The breakdown position is denoted by the sinusoidal wave superimposed on Figures 4.7-4.9. It should be noted that this is only an approximation of the vortex breakdown position. This data was obtained by LeMay (1988) for a thinner delta wing. In addition, this breakdown data was obtained for only a limited number of angles of attack in the range of motion (29-40°). For angles of attack in between these data points, the breakdown position had to be estimated from the nearest point. Subsequently, the breakdown location curve shown in Figures 4.7-4.18 is only an estimate of the breakdown location for the actual wing used during the tests conducted.

At lower angles of attack, when the vortex breakdown is near the trailing edge, the effect of the breakdown on the pressure field is not apparent. However, as the angle of attack increases and the breakdown moves upstream, an effect can be seen. In Figure 4.7, as the breakdown reaches the 45% chord location, a decrease in the pressure at the 45% tap can be seen. This decrease at the 45% pressure tap as the breakdown position reaches this point is also apparent in Figures 4.8 and 4.9 for $k = 0.20$ and $k = 0.30$ respectively. Figure 4.21 contains the $k = 0.30$ case, viewed from a different angle. Figure 4.21 is equivalent to looking at the three-dimensional plot in Figure 4.7 directly along the "chord location" axis (the x axis). Figure 4.21 shows the time response of each of the twelve pressure taps. The error bars on this figure represent the maximum uncertainty in the pressure coefficient (see section 3.5). The pressures from 35-45% can be seen to decrease during the first half of the

motion, then begin to increase, then decrease again. This second decrease occurs as the breakdown position is reaching the region of those pressure taps. Given the periodic pitching motion, as well as the periodic response of the lift coefficient (Bragg and Soltani, 1988), one might expect a periodic response of the pressure coefficient. Considering the size of the error bar for the 45% curve, it is possible that the decrease in pressure coefficient is not representing the physics of the flow. However, this decrease is also seen in the larger Reynolds numbers cases, where the error is not large enough to account for this. Furthermore, the error bars in Figure 4.21 represent the maximum; the consistency of the "dip" in the pressure coefficient curve seems to indicate that this is actually what is happening to the pressure field.

Figure 4.22 shows the 40% and 45% tap pressures from 4.21 ($U = 30$ ft/s, $k = 0.30$) on an expanded scale. The upper half of this figure shows the angle of attack time history of the model. During the first half of the motion, the pressure appears to follow the model motion; the pressure decreases and increases with the model motion. However, at roughly half the cycle of motion, the pressure decreases again, where it might be expected to continue increasing during the remainder of the pitch-up of the model. This expected pressure coefficient is shown on Figure 4.22 as a dotted line. It is during this part of the model motion that the vortex breakdown is nearest the leading edge of the model, thus nearest the two pressure taps shown in Figure 4.22. It appears that the vortex breakdown is affecting the pressures at the forward pressure taps. In addition, the 45% tap seems to be affected earlier than the 40% tap; the 45% pressures stop increasing earlier. This makes sense in that the breakdown is moving upstream at this point in the model motion.

Furthermore, it appears that some phase difference between the model position and the pressure coefficient may exist. Looking at Figure 4.22, the

minimum angle of attack and the minimum pressure coefficient appear to be shifted by approximately 0.05 cycles (18°), with the pressure coefficient lagging the angle of attack.

During the unsteady pitching motion, the model passes through 34° angle of attack on both an upstroke (angle of attack increasing) and a downstroke (angle of attack decreasing). Thus it is possible to compare these two instantaneous pressure distributions to the static 34° distribution. However, pressure data is not sampled at precisely 34° during the sinusoidal motion. On the upstroke, data is sampled at 34.2° , while on the downstroke data is sampled at 33.8° . However, considering the accuracy in measuring angle of attack, these two cases are still comparable to the static 34° data. The three $Re = 250,000$ (corresponding to a freestream velocity of 30 ft/s) are shown in Figures 4.25-4.27. These three figures are for reduced frequencies of $k = 0.10, 0.20,$ and 0.30 respectively. Pressure coefficient is plotted as a function of chord location for three cases: instantaneous 34° angle of attack on the upstroke and the downstroke, and static 34° angle of attack.

From Figure 4.25 it can be seen that the largest difference between the instantaneous and static distributions occurs at the forward pressure taps. From 35-45%, the downstroke pressures are slightly higher than the upstroke pressures. However, it should be noted that all three curves lie within the uncertainty of the pressure coefficient measurement. However, the characteristics of the curves will be discussed. There is a decrease in the 35% coefficient for the static curve, while for the two instantaneous curves, the coefficient continues to increase up to 35%. This is also seen in Figure 4.26, for a reduced frequency of $k = 0.20$. From 50-90%, the two instantaneous curves are very similar to each other and to the static curve. At the forward pressure

taps, the downstroke pressures are slightly higher. Again, the instantaneous pressures distributions increase up to 35%, while the static curve decreases at 35%.

For the reduced frequency of $k = 0.30$ (Figure 4.27), the largest difference between the instantaneous curves is again at the forward taps. However, there is a large discrepancy between the instantaneous curves and the static curve in the range of 65-85%. This difference could be explained by the uncertainty in the measurements. For the $k = 0.30$ case, as for the $k = 0.10$ and 0.20 cases, the downstroke pressures are slightly higher than the upstroke pressures. However, looking at Figures 4.25-4.23, there is no apparent consistency in the difference between the instantaneous pressures and the static pressure (and, as noted before, they are all within the uncertainty). The downstroke pressures are consistently higher than the upstroke pressures for the forward part of the wing.

By averaging the instantaneous pressure coefficients throughout the pitching motion, the mean pressure coefficient at each tap can be obtained. These values represent the mean distribution about which the pressure fluctuate during the cycle of motion. Figure 4.37 contains the mean pressure distributions for the three 30 ft/s cases. The static data for 30 ft/s and 34° angle of attack is also shown in this figure. The average pressure profiles at 30 ft/s and $k = 0.10$ and 0.20 are very similar. The peak pressure coefficient occurs at the 35% location. However, for the reduced frequency of 0.30 (see Figure 4.9), the pressure coefficient peaks at the 45% location, and also contains a slight decrease at the 60% location. Again, the bevel is affecting the pressures forward of the 45% location. The curve for $k = 0.30$ is shifted slightly from the other two reduced frequencies at the 65-85% taps. By comparing these mean

pressure profiles to the static profiles at 30 ft/s, it can be seen that the curves lie closest to the 34° static case. This appears to correspond to the mean angle of attack throughout the pitching motion (the model is pitched from 29-39°). The case of $k = 0.30$ has the largest deviation from the 34° static curve.

From Figures 4.7-4.9 it appears that the effect of the pitching motion is most pronounced near the apex of the model. However, the pressures vary by roughly the same percentage across the length of the model; the trailing edge pressures appear more constant due to the scale of the plot. Table 5 contains the percent variation of the instantaneous pressures from the mean pressure, at each chord location and for all three 30 ft/s cases. For the three reduced frequencies (0.10, 0.20, 0.30), the largest percent variation from the average pressure coefficient occurs at the 40% tap. In addition, the smallest variation occurs between 55% and 65%. In general, the variations are similar for all twelve pressure taps; the percent variations range from 2.0% to 5.2% (this maximum occurring for $k = 0.20$). For the 30 ft/s static data, the pressure coefficients vary by approximately 10% along the length of the wing. By averaging the percent variation at all twelve taps, an average variation for each reduced frequency can be obtained. This average variation increases slightly from 3.3% to 3.6% as the reduced frequency increases. However, looking at Figure 1.3, the lift curve for a delta wing of similar geometry, it can be seen that the lift coefficient varies by less than 10% about a mean value for the angle of attack used in this research. This implies similarly small fluctuations of pressure field over the wing, and thus the pressure along a line at 60% of the semi-span.

Looking at Figure 4.7, as the model pitches down, the pressure coefficients decrease. The model reaches its low point of travel and begins

pitching upwards. The pressure coefficients respond in a similar pattern. During the pitch-down, the pressures decrease, and during the pitch-up the pressures increase. This oscillation appears to be occurring at roughly the same frequency as the model motion. Upon performing a Discrete Fourier Transform on the data (see section 3.5), it was seen that the dominant frequency of the unsteady pressure was near the pitching frequency.

4.4.2 Tests at Reynolds Number 335,000

Figure 4.10-4.12 contain the three-dimensional plots of the pressure coefficient as a function of time and chord location for the $Re = 335,000$ cases of $k = 0.10, 0.20,$ and 0.30 (respectively). These three cases show characteristics similar to the $Re = 250,000$ cases, but with a much stronger decrease in pressure coefficient at the 35 and 40% locations. The curves are approximately linear from 90-60% of the chord. The pressure coefficient then increases abruptly to the 50 and 55% taps. This is followed by another increase to the 45% location, which is the suction peak for all three of the $Re = 335,000$ (corresponding to a freestream velocity of 40 ft/s) cases. The effect of the bevel then results in a decrease forward of this peak.

As the reduced frequency is increased from 0.10 to 0.30 (corresponding to pitch rates of 0.466 and 1.400 Hz), the variation of the pressure coefficient increases. By looking at the 45% tap in Figures 4.10, 4.11, and 4.12, the increase in fluctuation with increasing reduced frequency is apparent.

The approximate vortex breakdown position is again indicated on

Figures 4.10-4.12 by the line superimposed on the plot. As with the 30 ft/s cases, the breakdown position appears to affect the pressures at the 40% and 45% locations by creating a decrease in the pressure coefficient during the pitch-up part of the model motion (when an increase in pressure might be expected). This effect is most pronounced at the 45% tap, and most visible in Figure 4.12, for $k = 0.30$. As the breakdown reaches its closest position to the leading edge, the pressure at the 45% location decreases. Figure 4.23 shows an expanded view of the pressures at the 40% and 45% taps, for $k = 0.30$. This figure is arranged similarly to Figure 4.22, with the pressure time history on the bottom half, and the angle of attack time history on the top half. The pressure appears to follow the model motion, but a dip occurs in the pressure distribution in the range of 0.6-1.0 cycles. This is at the high angles of attack, where the breakdown is near the apex and the forward pressure taps. As with the 30 ft/s case, the error bars indicate an uncertainty sufficient to account for the decrease. However, the decrease seems to be too consistent to be attributed to uncertainty in the pressure measurements.

The possible phase difference noted in Figure 4.22 (for the 30 ft/s case) is again visible in Figure 4.23, for the 40 ft/s case. The minimum angle of attack and the minimum pressure coefficient appear to be shifted by roughly 18° . The minimum for the two different chord positions appears to be the nearly the same; however, the decrease probably due to breakdown occurring at the 45% location before it occurs at the 40% location.

Figures 4.28-4.30 contain plots of the instantaneous pressure distributions for 34° angle of attack compared to the static 34° distribution. These three figures are for the freestream velocity of 40 ft/s and reduced frequencies of 0.10, 0.20, and 0.30 respectively. The characteristics of these

three figures are similar to those of 4.25-4.27. From 60% to 90%, the difference between the upstroke and downstroke pressures is very small. For chord locations forward of this, the downstroke pressures are higher than the upstroke pressures. There is no apparent consistency in the value of the instantaneous pressures relative to the static curve. The same general shape of the pressure distribution exists, but the instantaneous pressures are not consistently less than or greater than the static curve. Furthermore, although the uncertainty is less for this Reynolds number, the curves are all within the amount of uncertainty of each other, for all three reduced frequencies.

As with the 30 ft/s cases, the 40 ft/s cases can be averaged with respect to time to yield an average pressure distribution through the pitching cycle. As with the average 30 ft/s cases, the average 40 ft/s cases are very similar. In addition, they are very similar to the 40 ft/s static curve at 34° angle of attack, the mean of the unsteady motion. In general, the average 40 ft/s cases do not yield any new information, and have not been included for this reason. The average 30 ft/s cases (Figure 4.33) are representative of all the 40 ft/s cases as well.

Table 6 contains the percent variation of the fluctuating pressure from the mean value for each chord location, and the overall variation from the mean pressure. For the reduced frequency of $k = 0.10$, the largest variation occurs at the 40% location (as for all three of the 30 ft/s cases). However, for $k = 0.20$ and 0.30 , the largest variation occurs at 35%, with the second largest at 40%. The overall fluctuation increases from 2.5% to 3.3% to 4.7% as the reduced frequency increases from 0.10 to 0.30. This increase was also seen for the 30 ft/s cases, although it was smaller. The static data at 40 ft/s varies about a mean value by approximately 12-18%. The difference in location of the peak

fluctuation (from 40% to 35%) could be due to the position of the vortex core. The vortex core does not necessarily lie along a straight line from the apex to the trailing edge; if it is curved line, it could be crossing the line of pressure taps at a different chord locations depending on the test.

4.4.3 Tests at Reynolds Number 420,000

The three cases at $Re = 420,000$ are shown in Figure 4.13-4.15; these are for reduced frequencies of 0.10, 0.20, and 0.30 respectively. This Reynolds number corresponds to a freestream velocity of 50 ft/s. The characteristics of these three plots are similar to those of the two lower speed cases, 30 and 40 ft/s. The plateau in the curve at the 50-55% location is still evident, as is the peak in the curve at the 45% location. The pressure coefficients decrease forward of the peak at 45%, although the decrease is less severe than in the 40 ft/s cases. The general reaction of the pressure to the model oscillation is still the same; the pressure decrease with a decrease in angle of attack, and increase with increasing angle of attack; all at roughly the same frequency as the model pitching frequency.

The vortex breakdown location is superimposed on Figure 4.13-4.15. The most significant effect of the breakdown appears to occur near the apex of the wing. The pressures at the 45% tap decrease as the vortex breakdown reaches that chord position during the pitch-up part of the motion. This was also seen for the two lower Reynolds number cases. The effect is most apparent in Figure 4.13, for $k = 0.10$; but it can be seen to some extent in all three of the 50

ft/s cases. The breakdown appears to cause a decrease in the pressure coefficient as it reaches 40-45% of the chord.

The instantaneous pressure distributions for the 50 ft/s cases at 34° angle of attack are shown in Figures 4.31-4.33. These three figures are arranged in order of increasing reduced frequency. As with the previous figures showing the instantaneous pressure distributions, the difference between the upstroke and downstroke values for the 50 ft/s cases is very small from 60-90% of the chord. The uncertainty is smaller than for the previous cases, but the curves are closer. From 35-55%, the upstroke pressure is sometimes higher than the downstroke pressure, and sometimes lower. For all three reduced frequencies the downstroke pressure is higher for the 35% and 40% locations. However, for $k = 0.10$ and 0.20 (Figures 4.31 and 4.32), the 45% upstroke pressure is higher than the downstroke pressure. But for $k = 0.30$ (Figure 4.33), the downstroke pressure is again higher. As with the lower speed cases, there appears to be no consistent trend involving the location of the instantaneous pressures relative to the static pressures.

As with the preceding data, the average distributions for the 50 ft/s cases are very similar for all three reduced frequencies. Furthermore, they are also very similar to the 50 ft/s static curve at 34°. As with the 40 ft/s average cases, no new information is contained in these average distributions.

The percent variation from the mean pressure for each chord location is shown in Table 7. For $k = 0.10$ and $k = 0.20$, the largest variation from the mean occurs at the 35% location; for $k = 0.30$ this maximum occurs at 40% of the chord. For the static data at 50 ft/s, the pressure coefficients vary from 2-15% of

the mean static value. The overall fluctuation for the three dynamic cases varies from 3.1% for $k = 0.10$, to 4.1% for $k = 0.20$, to 3.5% for $k = 0.30$. A slight decrease in the overall percent variation occurs from $k = 0.20$ to $k = 0.30$. For the 30 and 40 ft/s cases, the variation increased with increasing reduced frequency.

4.4.4 Tests at Reynolds Number 500,000

The three-dimensional plots for the three $Re = 500,000$ cases (corresponding to a freestream velocity of 60 ft/s) are shown in Figures 4.16-4.18. These figures are for $k = 0.10$, 0.20, and 0.30, respectively. As with the other three freestream velocity cases shown in Figures 4.7-4.15, the prevailing characteristics are the approximate linearity of the curves from 60-90%, the similarity of the 50 and 55% coefficients, and the peak at or near the 45% location. However, the peak at 45% is only clearly defined in the $k = 0.20$ case (Figure 4.17). For $k = 0.10$ and $k = 0.30$, the decrease forward of the 45% location is slightly less. However, there appears to be no significant difference in the curves due to an increase in reduced frequency (comparing Figures 4.16, 4.17, and 4.18). There appears to be a decrease in the pressure coefficient at the 60% location that increases as k increases. Looking at Figure 4.16, the curve is roughly linear up until the sudden increase to 55%. However, as reduced frequency is increased, a slight dip in the curve appears at 60%. In Figure 4.16, the curve contains a trough at 60% of the curve. This characteristic is also apparent in the 30 ft/s cases, but not as much so in the 40 and 50 ft/s cases.

As with the previous three Reynolds number cases, the approximate vortex breakdown position has been superimposed on Figures 4.16-4.18. As with the previous cases, the breakdown appears to be causing a decrease in the pressure coefficient at the 40% and 45% locations. This occurs during the portion of the pitching motion when the model is at the high angles of attack, placing the breakdown near the 40-45% chord position. Figure 4.24 shows the angle of attack time history in the upper half, and the pressure coefficient time history for the 40 and 45% taps in the bottom half. This figure more clearly shows the decrease of pressure at the high angles of attack, although not as clearly as it was seen for the two lower Reynolds numbers in Figures 4.22 and 4.23. Figure 4.24 shows the pressure coefficient at 40-45% decreasing as the model reaches its highest angle of attack and begins pitching down. Again, this is when the vortex breakdown is farthest upstream, near the 40-45% chord location.

The instantaneous 34° pressure distributions for the 60 ft/s cases are shown in Figures 4.34-4.36, along with the static 34° distribution. Error bars are not present on these three figures because for this Reynolds number, the uncertainty is less than the width of the symbols used in the figures. For $k = 0.20$ (Figure 4.35) the downstroke pressures are consistently higher than the upstroke pressures. For $k = 0.10$ and 0.30 , the upstroke and downstroke pressures are similar from 60-90%. The increase in the downstroke pressure at 35%, seen for the previous freestream velocities, is also seen in all three of the 60 ft/s cases. However, at 45% of the chord, the downstroke pressure is higher only for $k = 0.20$. For all three of the reduced frequencies at 60 ft/s, the instantaneous pressures at the 35-50% locations are consistently lower than

the static values.

The trends in the average pressure distribution at this Reynolds number are similar to those seen at the three lower Reynolds numbers. No significant difference exists between the distributions of different reduced frequencies; and all three are within experimental error of the 60 ft/s static case at 34° angle of attack.

Table 8 contains the percent variation from the time averaged value of the pressure coefficient at each chord location. For $k = 0.10$, the maximum fluctuation occurs at 40 % of the chord. For $k = 0.20$ the maximum is located at 65%; for $k = 0.30$ the maximum is at 40%. For the lower speed experiments, the maximum was typically located at the 40% tap as well. However, the $k = 0.20$ case is the only case with the 65% position as the maximum fluctuation. The average percent variation for all twelve taps is 3.9% for $k = 0.10$; 5.0% for $k = 0.20$; and 4.9% for $k = 0.30$. As with the 50 ft/s cases, there is a slight decrease in overall variation as the reduced frequency increases from 0.20 to 0.30. The static data at 60 ft/s fluctuates by 7-11% about a mean value in the range of 29°-40°.

4.5 Additional Pressure Data

The data sets discussed above, for four freestream velocities and three reduced frequencies, compromise the bulk of the unsteady pressure data. However, during the course of this research, additional unsteady pressure data

was obtained. The most interesting of this data will be presented in this section, and characteristics relevant to the primary pressure data will be pointed out.

The first set of data to be presented includes two pressure profiles obtained from the right side of the delta wing model (as opposed to the left side, where the primary pressure data was obtained). Next, some of the data taken at the reference pressure tap (the tap monitored during each experiment) will be presented.

4.5.1 Right Side Pressure Data

The twelve data sets discussed above were all obtained on the left side of the delta wing model, where left and right are spanwise directions relative to the root chord of the model. In addition to that data, two pressure profiles were obtained from the right side of the model. The pressure taps were located in the same positions; taps were set at 5% increments from 35% of the root chord to 90%. These taps were also placed along a ray at 60% of the local semi-span. These two profiles were both for a reduced frequency of $k = 0.10$, and for two Reynolds numbers of 250,000 and 335,000 (30 ft/s and 40 ft/s). These profiles are shown in Figures 4.19 and 4.20.

In general, these two pressure distributions have similar characteristics to the pressure profiles obtained from the left side of the model (see Figures 4.7-4.18). The general shape as well as the magnitude of the pressure coefficients is similar. The similarity of the pressure coefficient at the 50 and 55% locations is also apparent in Figures 4.19 and 4.20. However, there is a difference at the 45% pressure tap. Throughout the left side pressure profiles, the 45% pressure

was one of the highest pressure coefficients. However, looking at Figure 4.19 or 4.20, the 45% location has a value similar to the 50 and 55% locations; while the 40% tap is the suction peak. The decrease in the 35% coefficient due to the bevel is again evident.

As the freestream velocity is increased from 30 ft/s to 40 ft/s, there are two effects apparent in Figures 4.19 and 4.20. First, the peak at 40% becomes more definitive; and second, the values in the range of 45-55% become more constant. Apparently, the pressure coefficient has decreased from the 40% tap to the 45% tap on the right side, while increasing on the left side.

This difference is not easily explained. The tests on the right side of the model were not conducted at the same time as the tests on the left side. It is possible that some type of hysteresis resulted in a different flow state existing during the two tests. Furthermore, a small amount of yaw angle in the model position could cause this asymmetric pressure coefficient at the 45% tap.

It is also possible that the location of the vortex core is partially responsible. If through the angle of attack range of 29-40° the vortex core location is not symmetric about the root chord; the pressure field along the two 60% semi-span rays could possibly be different. Asymmetry of the vortex breakdown location could also be responsible for this. Asymmetry of the vortex cores has been noted for a delta wing of 80° leading edge sweep (Lowson, 1964). Furthermore, in 1968 Wentz tested delta wings of leading edge sweep angles from 75-85° and found that the breakdown position was extremely sensitive to yaw angle. The yaw angle (as well as the pitch angle) could only be measured to within 0.5°; such a deviation could possibly have resulted in asymmetric vortices.

However, the effect of the vortex breakdown appears to be similar on both sides of the model. The data from the left side indicated that the presence

of vortex breakdown was causing a decrease in the pressure coefficient at the 40% and 45% locations. This decrease can also be seen in Figures 4.19 and 4.20. The data from LeMay (1988) was obtained for vortex breakdown on the left side of the model. Considering the difference in wing thicknesses, it may not be appropriate to assume that the breakdown location on the right side of the current model is the same as the location on the left side of LeMay's model. However, the 45% tap pressure distribution in Figures 4.19 and 4.20 show the same decrease in pressure during an increase in angle of attack that was seen in the left side data.

Table 9 contains the percent variation of each chord location from the mean pressure coefficient. For both of the right side cases (30 ft/s and 40 ft/s), the maximum variation occurs at 40% of the chord. This was also the position of the maximum variation from the mean for both of the left side cases. The overall percent variation is slightly higher for each of the right side cases as compared to the left side cases.

The standard deviation for the right side pressure profiles (see Section 3.5 for more information on the standard deviation) is comparable to the that for the left side cases. For the 30 ft/s right side case, the standard deviation was 0.045 psi; for the 40 ft/s case it was 0.079 psi. For the corresponding left side case, the standard deviations were 0.040 and 0.081 psi.

4.5.2 Reference Pressure Port Data

Throughout the unsteady pressure experiments performed during this research, one pressure tap was sampled during each test. This was done as a way of checking for any change in the flow conditions between tests that should have been conducted under the same conditions. This pressure tap was located at 90% of the root chord and 60% of the local semi-span, on the right side of the model centerline. For each pressure profile (specific velocity and reduced frequency), twelve individual tests were conducted; one at each chord location. In theory, the pressures recorded by the reference tap should be similar for each of these twelve tests.

During each static test (specific Reynolds number and angle of attack), twelve data records were made from the reference tap. By taking the average of each of these sets of twelve data records, it is possible to examine the difference in the pressures at this tap. Figure 4.38 shows the reference pressures from one test. Twelve curves are shown in this figure: each one taken at the same pressure tap, but during a separate test (as the twelve pressure taps on the left side of the model were being alternately sampled). Figure 4.38 is a typical case. The reference pressure vary by less than 5% between tests. Considering that the uncertainty in the pressure coefficient for most of the tests is also in this range, the pressures from the reference tap indicate nothing unusual for the static tests.

For each of the unsteady pressure tests conducted, the reference pressure port was monitored in an identical fashion. Similar to the static tests, the reference pressures from the dynamic tests show no unusual behavior.

The difference in the pressures is consistently less than the amount of uncertainty in the measurement.

V CONCLUSIONS AND RECOMMENDATIONS

5.1 Conclusions

This research has been designed not only as a means of obtaining unsteady pressure information over the surface of a delta wing; but also as a means of evaluating the technique for making this type of measurement. As such, the conclusions from this work fall into two categories: first, conclusions from the actual data on the flow field physics. This includes the significant trends observed, the apparent effect of the pitching motion, and the interaction of the vortex flow with the pressure field. Second, conclusions can be drawn on the testing procedure and the validity of making unsteady pressure measurements. This includes the advantages of the current testing procedure as well as methods that could be improved in future research.

5.1.1 Unsteady Pressure Data

One of the most readily apparent trends seen throughout the unsteady data involves the reaction of the pressure field to the sinusoidal pitching motion. For all the freestream velocities and reduced frequencies tested, the pressure field reacted in a very similar way. Furthermore, the pressure fluctuations were

relatively small. Also, the percentage of the pressure fluctuation was similar for each of the twelve chord positions tested, typically with a slight increase for the forward positions. The maximum fluctuation was typically at the 40-45% chord location. This fluctuation was typically less than 10% about the mean value. This amount is similar to the amount of fluctuation in the lift found by McKernan (1983) for a delta wing of similar geometry. Figure 1.3 shows this lift curve. From 29-40° angle of attack, the lift coefficient changes by less than 10%. Jarrah (1988) examined the effect of a periodic pitching motion on the aerodynamic coefficients for a 76° sweep delta wing. He reported fluctuations up to 40% for a much larger range of motion of 20-60° and a Reynolds number of 450,000. Over this angle of attack range the change in lift coefficient is much greater.

For the pressure taps near the trailing edge, from 70-90% of the chord, the frequency of the pressure fluctuations was nearly the same as the pitching frequency. However, at the 40-50% chord locations, the surface pressures fluctuated at close to twice the pitching frequency (see Figure 4.22). This is possibly due to the increased effect of vortex breakdown at these chord locations.

It was also consistently seen that the average pressure distribution throughout an unsteady cycle of motion was similar to the static distribution corresponding to the average angle of attack throughout the motion. Specifically, for the pitching motion from 29-40°, the average pressure distribution corresponded to the static curve for 34°. This was especially true when the uncertainty of the pressure measurements was taken into consideration.

Another characteristic seen through the data sets was an effect on the pressure coefficient curve due to the bevel of the model. As stated before, a pressure tap was placed on the face of the bevel, as well as on the corner of the bevel and the top surface. The pressure coefficient would increase over the two bevel taps; from 35% to 45%. The pressures would then decrease downstream to the trailing edge. The peak pressure coefficient would be expected near the primary vortex, where the flow velocity is the greatest. Near the leading edge (and thus on the bevel), the leading edge separation, the secondary vortex, and secondary reattachment are all occurring, effecting the pressure field, possibly resulting in a smaller pressure coefficient at the bevel taps.

The pressure field above the wing was seen to be most sensitive to vortex breakdown at the forward locations. The pressure taps located at 40% and 45% of the chord were seen to react to the varying location of vortex breakdown through the pitching cycle. At the low angles of attack, the pressure at these two taps follows the model motion; the pressure decreases with decreasing angle of attack, then increases as the wing begins pitching up. However, as the angle of attack continues increasing, the pressure coefficients decrease at the 40% and 45% locations. This is probably due to the position of the vortex breakdown near these chord locations during that portion of the pitching cycle. Furthermore, the decrease in pressure occurs at the 45% tap slightly before occurring at the 40%; this could be a result of the upstream movement of the breakdown during the pitch-up.

In addition, a phase lag between the model motion and the pressure distribution was seen. The minimum angle of attack and the minimum pressure coefficient appeared to be shifted by approximately 15-20°. The maximum pressure coefficient could not be correlated to the maximum angle of attack

because for this angle of attack the upstream chord positions were affected by the vortex breakdown; and the downstream positions did not have fluctuations large enough to clearly identify peak values.

However, considering the drastic change in the vortex flow structure after breakdown occurs, it would seem that the pressure field forward of breakdown would be significantly different than downstream of breakdown. However, no such drastic effect was seen for the Reynolds numbers and pitch rates tested.

First, it is possible that the pressure taps were not located in the appropriate place to register some effect of the vortex breakdown. It is possible that the breakdown was not consistently occurring at 60% of the local semi-span. Furthermore, the vortex core may not behave as a straight line; it may be curved along the upper surface of the model, only intersecting the 60% semi-span line at some positions.

A second possibility is that the vortex breakdown is just not substantially affecting the surface pressures. The vortex core lies a certain distance above the surface of the wing; this distance changes with angle of attack. Right at the surface of the wing, reattachment and secondary separation are also occurring (see Figure 1.2). While the vortex core has been seen to affect the surface pressure in spanwise studies (McKernan, 1983), it may be possible that the effect of the vortex breakdown is not substantial enough to be apparent in the 60% semi-span region. The forward chord location pressures (40-45%) were affected by the breakdown, but not in such a way that the location of vortex breakdown could be inferred from the pressure data alone.

However, the location of the vortex core may be apparent in the pressures at the forward positions. As stated before, the pressures at the taps

located on the bevel (35% and 40%) were typically lower than at the 45% tap. However, this was not true for several cases : the dynamic cases of 30 ft/s and $k = 0.10$ and 0.20 ; and the static cases of 39° angle of attack and freestream velocities of 50 and 60 ft/s. In these four cases, the pressure coefficient continued increasing up to the 35% location. This could be an indication of a difference in the vortex core position relative to the other cases. Perhaps for these high speed static cases and the low speed dynamic cases, the vortex core lies closer to the leading edge. Assuming that a low pressure is associated with a high velocity and thus with the vortex core, then the variation of the bevel pressure coefficients may be indicative of the core position. This would mean that the vortex core moves laterally as the angle of attack changes; and in the static tests, the possible onset of stall by 39° angle of attack (implied by the decrease of the pressure coefficients) has moved the core onto the bevel.

Obviously, the unsteady pressure field has some complex characteristics. The pressure profiles obtained for the right side of the model showed similar characteristics, although with their own peculiarities. Nevertheless, this right side data helps to confirm that the pressure field is behaving in a complicated fashion and that it is not just a case of damaged pressure taps. The similarity of the 50% and 55% taps, the behavior of the pressures over the bevel, and the unusual behavior seen in the static data are all typical of the unexpected trends observed.

In addition, this type of unsteady data can be difficult to effectively present. Three dimensional figures were necessary to include all the important parameters. However, with this type of figure only the gross features can be distinguished; subtleties are difficult to see. Certain trends are readily apparent in the data, but finding the most effective form of viewing the data such that the

physics of the flow can be partially explained is a difficult problem.

For the angle of attack range used during this testing, the vortex breakdown played a small part in the overall pressure field on the suction side of the delta wing model. Breakdown can be a drastic visual phenomenon. However, the general form of the flow field remains the same; two separated but stable vortices exist over the wing. Flow separation over a rectangular wing with a Joukowski-type airfoil causes a significant effect on the pressure field as well as the lift and aerodynamic loads. Vortex breakdown, while being a similarly significant visual effect, is not the same as flow separation. At high angles of attack, the flow field over a delta wing is constantly separated; the breakdown is only a change in the vortex parameters. As such, its effect on the surface pressures (at the high angles of attack currently under investigation) is small; the most significant effect is caused by the vortex core. Both the location and the shape of the vortex core change through the unsteady pitching motion; these changes affected the surface pressures as much as the change in breakdown location did.

5.1.2 Acquisition of Unsteady Pressure Data

In general, this type of unsteady pressure research demands a great deal of attention to analysis of the data. Considering the complex nature of both the vortex flow and the reaction of the pressure measuring equipment to the unsteadiness, the data needs to be examined as closely as possible to determine what phenomenon is being reflected. Certainly, additional research in this area is needed: a highly complicated and unsteady pressure field has

been seen to exist. This project has been attempted to identify some of the major characteristics of the field, as well as the major difficulties associated with obtaining data of this nature.

Ideally, the unsteady pressures should be sampled right at the surface, and at all chord locations simultaneously. Such an experimental procedure would often be impractical. Thus compromises must be made. The effect of using remotely positioned pressure transducers and a length of connecting tubing seems justified from the results of this research. The effect of the tubing was seen to be relatively small in the frequency range of interest.

However, the difficulty involved in only sampling three chord locations at a time was substantial. By reconfiguring the pressure taps during each test, the possibility of disturbing or altering the flow field existed. However, certain consistent trends seen in the pressure distribution shape (for example, the similarity of the 50% and 55% locations) can not be explained by the testing procedure. Considering that a different set of three chord locations had lines attached during each test, the consistency of the pressure distributions would rule out the testing procedure as the cause. However, by attaching all twelve pressure lines to the model at once, the possibility of this could have been eliminated. Of course, that would then create the possibility of crimping a tube inside the model (due to the large number of tubes), or disturbing the flow further by the large bundle of twelve lines coming from the model. A test could be conducted with each configuration to determine the difference, if any.

An additional conclusion involves the amount of data obtained. There are several parameters to be simultaneously sampled: angle of attack, chord

location, freestream dynamic pressure, and surface pressure. Typically many sets of data will be taken and then averaged for a test. During this research, fifty sets of fifty points were taken during each cycle and then averaged. Although this constitutes a great deal of data, additional points should be taken. By taking more data points through the pitching cycle, it may be possible to do a more detailed Fourier analysis on the data to extract dominant frequencies. By sampling more cycles, lower frequencies can be resolved. This effort was not successful in the current research due to the relatively small number of data points. Emphasis should be placed on obtaining information on the frequency of the pressure fluctuations as well as the magnitude.

5.2 Recommendations

During the course of this research, several questions were raised that could not be satisfactorily answered. Data sets that were difficult to explain were seen, and tangent areas of interest were discovered. Hopefully future research in this area will be able to address some of these issues.

As far as making recommendations for such future research is concerned, this will be limited to areas of study, as opposed to specifics of the experimental procedure. Certainly, due to research funds, time constraints, and equipment availability, some shortcomings existed in the experimental procedure. Considering the current rate of technological advance, any given piece of equipment used during this study could probably have been replaced with one better. But belaboring equipment is pointless; this research has been designed to study flow phenomenon, not machine design or systems

integration. The unlimited availability of state-of-the-art equipment is a tremendous but unreasonable research advantage; how close a particular study can come to achieving this is up to each researcher.

Recommendations for future research areas include :

1. Initially, any future study on unsteady pressures that opts to use remote pressure sensing device and connecting tubing should do a more in depth examination of the tubing effects. This way it may be possible to tailor the specific dimensions of the tubing to provide a desirable amplitude attenuation or phase shift for the frequency range of interest. For example, the tubing could be sized to provide an amplification of a certain frequency range of interest, with a desirable phase shift. In addition, the transfer functions for both the freestream dynamic pressure and the unsteady model pressures could possibly be matched. It may also be possible, knowing the transfer functions, to correct the unsteady pressure data during the actual data acquisition process.

2. A study of the spanwise location of vortex breakdown for both static angle of attack and a sinusoidal pitching motion. This study, as well as other pressure investigations, locates the line of pressure taps at the 60% local semi-span under the assumption that that this is where the vortex core exists. This assumption stems from previous pressure data showing a suction peak at the 60% location. This is hardly a definitive reason for assuming the location of the vortex core. In fact, LeMay (1988) noted that the spanwise location of the vortex changed with both angle of attack and pitching frequency. By assuming an average location of 60%, important information could be overlooked.

3. A more comprehensive study of the static pressure distribution for

delta wings. This should include such specific parameters as wing thickness, bevel angle, and vertical location of the model in the wind tunnel. Certainly, this would be a monumental amount of data, but such a data base would be extremely useful. Having a "standard" set of static pressure data would be useful in comparing the validity of future and past studies.

4. A much more detailed study into static breakdown location hysteresis; and static pressure distribution hysteresis. Most studies on unsteady delta wings encounter this phenomenon, yet little factual data exists on the static hysteresis. The effect of a breakdown or pressure hysteresis can be substantial; more research needs to be done in order to quantify the parameters involved. It is possible that different static flow conditions exist for certain delta wings; knowing the procedure for reaching a given condition would be helpful.

5. A study of the effect that the flow on the pressure side of the wing has on the flow on the suction side. This should include an examination of any difference in flow patterns due to the location of the sting. The leading edge vortex is caused by the separation of the flow as it impinges on the bottom of the wing and moves toward the leading edges. By mounting the sting on the bottom of the wing (as opposed to a tail mount, for example), it is possible that some interference with the feeding sheet is occurring.

6. A study on unsteady pressure distributions for a delta wing undergoing transient pitching motions. Maneuvering flight involves transient motions; as such the effect of a transient motion on the pressure field would be of interest. Such a study should include the time lag for the pressure field to return to static conditions, as well as any hysteresis involved.

TABLE 1
LIST OF DYNAMIC TESTS PERFORMED

FREESTREAM VELOCITY (ft/s)	REYNOLDS NUMBER	REDUCED FREQUENCY	PITCHING RATE (Hz)	SAMPLING RATE (Hz)
30	250,000	0.10	0.350	15.90
		0.20	0.700	31.81
		0.30	1.050	47.71
40	335,000	0.10	0.467	21.20
		0.20	0.933	42.41
		0.30	1.400	63.62
50	420,000	0.10	0.583	26.50
		0.20	1.166	53.01
		0.30	1.750	79.52
60	500,000	0.10	0.700	31.81
		0.20	1.400	63.62
		0.30	2.100	95.43

TABLE 2
LIST OF STATIC TESTS PERFORMED

FREESTREAM VELOCITY (ft/s)	REYNOLDS NUMBER	ANGLE OF ATTACK (deg)
30	250,000	29
		34
		39
40	335,000	29
		34
		39
50	420,000	29
		34
		39
60	500,000	29
		34
		39

TABLE 3

**STANDARD DEVIATION OF THE 50 SETS OF PRESSURE DATA
AVERAGED FOR EACH TEST**

STATIC TESTS :

FREESTREAM VELOCITY	ANGLE OF ATTACK	STANDARD DEVIATION (psi)
30 ft/s	29°	0.0128
	34°	0.0129
	39°	0.0140
40 ft/s	29°	0.0225
	34°	0.0244
	39°	0.0269
50 ft/s	29°	0.0202
	34°	0.0308
	39°	0.1031
60 ft/s	29°	0.0257
	34°	0.0413
	39°	0.1177

UNSTEADY TESTS :

FREESTREAM VELOCITY	REDUCED FREQUENCY	STANDARD DEVIATION (psi)
30 ft/s	0.10	0.0401
	0.20	0.0366
	0.30	0.0403
40 ft/s	0.10	0.0806
	0.20	0.0712
	0.30	0.0678
50 ft/s	0.10	0.1215
	0.20	0.1188
	0.30	0.1073
60 ft/s	0.10	0.1721
	0.20	0.1446
	0.30	0.1409

TABLE 4
CORRESPONDENCE OF CYCLES OF MOTION TO ANGLE OF ATTACK

Point	Cycles	Angle of Attack	Point	Cycles	Angle of Attack
1	0.022	33.50	26	0.572	37.12
2	0.044	32.76	27	0.594	37.76
3	0.066	32.06	28	0.616	38.34
4	0.088	31.41	29	0.638	38.85
5	0.110	30.81	30	0.660	39.27
6	0.132	30.28	31	0.682	39.60
7	0.154	29.84	32	0.704	39.83
8	0.176	29.48	33	0.726	39.97
9	0.198	29.22	34	0.748	40.00
10	0.220	29.06	35	0.770	39.92
11	0.242	29.00	36	0.792	39.74
12	0.264	29.05	37	0.814	39.46
13	0.286	29.20	38	0.836	39.09
14	0.308	29.45	39	0.858	38.62
15	0.330	29.80	40	0.880	38.08
16	0.352	30.24	41	0.902	37.47
17	0.374	30.76	42	0.924	36.81
18	0.396	31.35	43	0.946	36.10
19	0.418	32.00	44	0.968	35.36
20	0.440	32.71	45	0.990	34.60
21	0.462	33.44	46	1.012	33.84
22	0.484	34.19	47	1.034	33.10
23	0.506	34.95	48	1.056	32.38
24	0.528	35.70	49	1.078	31.70
25	0.550	36.43	50	1.100	31.07

C-2

TABLE 5

PERCENT VARIATION OF INSTANTANEOUS PRESSURE
COEFFICIENT FROM MEAN VALUE : $RE = 250,000$, $U = 30$ FT/S

CHORD LOCATION (% x/c)	PERCENT VARIATION FROM MEAN C_p :		
	$k = 0.10$	$k = 0.20$	$k = 0.30$
35	3.4%	3.5%	3.6%
40	4.6	4.7	5.2
45	4.1	3.2	3.8
50	3.9	2.5	3.4
55	2.3	4.6	2.6
60	2.9	2.4	2.7
65	2.5	3.2	3.1
70	3.0	2.8	4.1
75	2.8	3.5	4.1
80	3.7	3.0	3.7
85	2.7	5.2	3.5
90	3.7	4.1	3.2
AVERAGE	3.30	3.56	3.58

TABLE 6

PERCENT VARIATION OF INSTANTANEOUS PRESSURE
COEFFICIENT FROM MEAN VALUE : $RE = 335,000$, $U = 40$ FT/S

CHORD LOCATION (% x/c)	PERCENT VARIATION FROM MEAN C_p :		
	$k = 0.10$	$k = 0.20$	$k = 0.30$
35	2.5%	4.9%	9.2%
40	3.4	4.0	7.2
45	3.1	3.6	5.0
50	3.2	4.0	5.2
55	2.6	1.7	4.4
60	2.5	2.4	3.4
65	2.0	2.7	5.2
70	2.2	3.8	3.3
75	2.0	2.5	3.6
80	1.4	3.5	2.9
85	1.9	3.5	3.9
90	3.2	3.4	2.8
AVERAGE :	2.50	3.33	4.68

TABLE 7

PERCENT VARIATION OF INSTANTANEOUS PRESSURE
COEFFICIENT FROM MEAN VALUE : $RE = 420,000$, $U = 50$ FT/S

CHORD LOCATION (% x/c)	PERCENT VARIATION FROM MEAN C_p :		
	k = 0.10	k = 0.20	k = 0.30
35	4.5%	5.8%	4.4%
40	4.4	4.6	5.3
45	4.0	4.9	3.8
50	2.5	3.4	2.5
55	2.6	5.2	2.7
60	2.1	4.4	3.5
65	4.7	3.8	3.2
70	2.0	2.1	3.6
75	2.2	2.3	3.2
80	2.9	4.3	3.8
85	3.1	4.8	2.7
90	2.5	3.4	3.6
AVERAGE	3.13	4.08	3.53

TABLE 8

PERCENT VARIATION OF INSTANTANEOUS PRESSURE
COEFFICIENT FROM MEAN VALUE : $RE = 500,000$, $U = 60$ FT/S

CHORD LOCATION (% x/c)	PERCENT VARIATION FROM MEAN C_p :		
	$k = 0.10$	$k = 0.20$	$k = 0.30$
35	4.7%	4.7%	3.0%
40	6.8	4.2	10.9
45	3.6	4.5	6.7
50	3.7	5.1	3.1
55	2.8	3.6	3.1
60	3.3	3.7	4.0
65	3.3	7.1	4.0
70	3.7	4.7	3.2
75	3.0	3.7	3.0
80	4.3	5.8	7.8
85	4.9	6.0	4.1
90	2.9	6.4	5.8
AVERAGE :	3.92	4.96	4.89

TABLE 9

PERCENT VARIATION OF INSTANTANEOUS PRESSURE COEFFICIENT
FROM MEAN VALUE FOR RIGHT SIDE DISTRIBUTIONS : RE = 250,000
AND 335,000 , U = 30 AND 40 FT/S , k = 0.10.

CHORD LOCATION (% x/c)	PERCENT VARIATION FROM MEAN C_p :	
	U = 30 ft/s	U = 40 ft/s
35	7.1%	4.6%
40	8.0	5.2
45	6.9	4.9
50	2.1	2.7
55	2.4	3.1
60	4.8	2.8
65	3.1	2.0
70	3.2	4.2
75	4.3	3.1
80	2.8	2.3
85	2.2	3.7
90	3.9	3.8
AVERAGE :	4.23	3.53

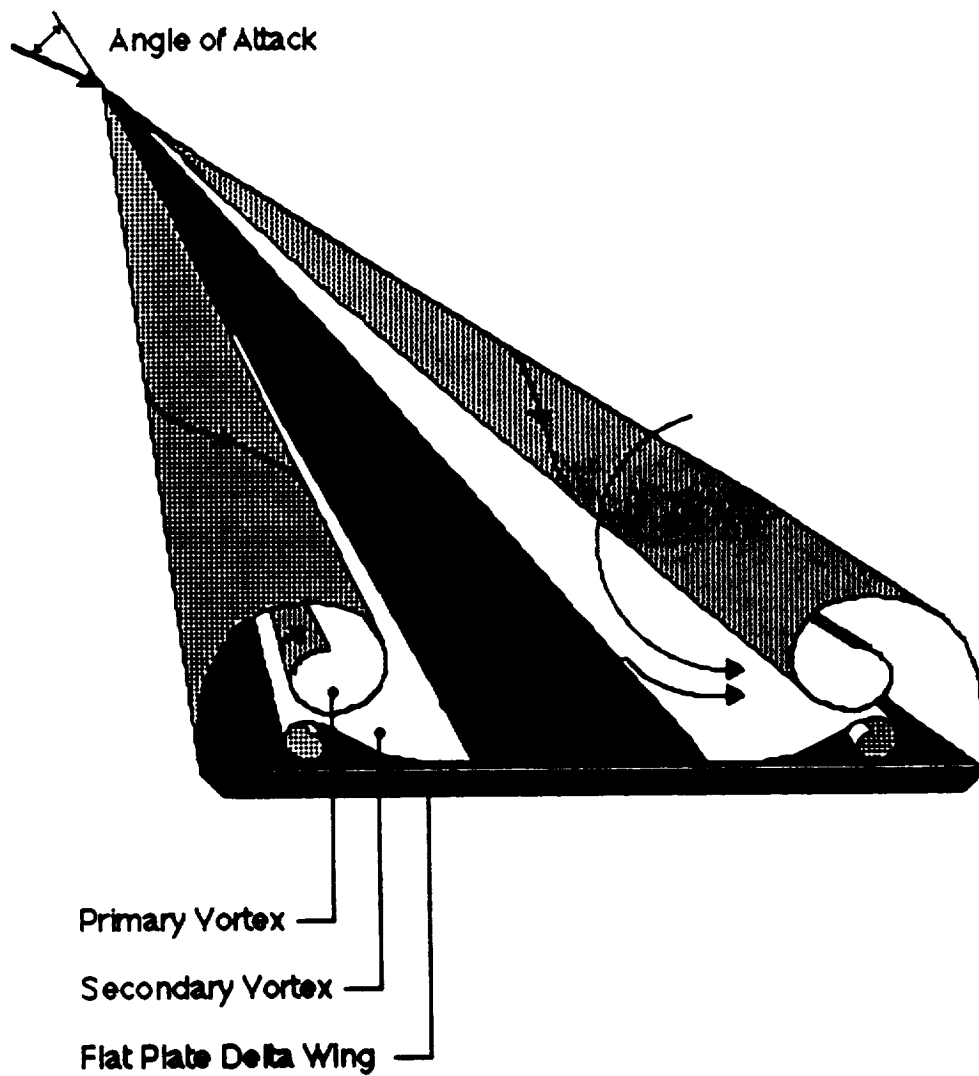


Figure 1.1

Delta Wing Leading Edge Vortex Flow.
(Adapted from Payne 1987)

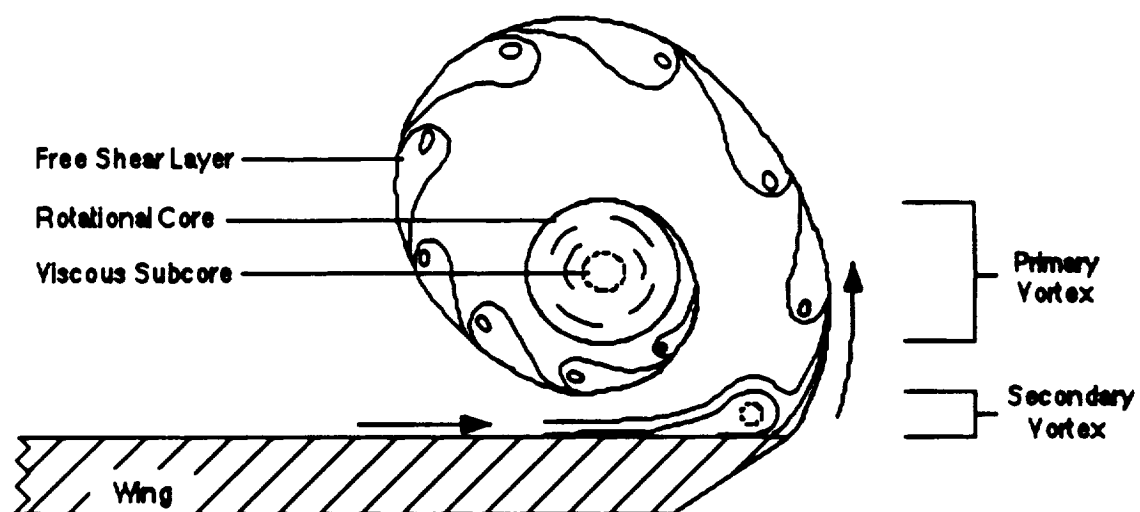


Figure 1.2

Leading Edge Vortex Cross Section.
(Adapted from Payne 1987)

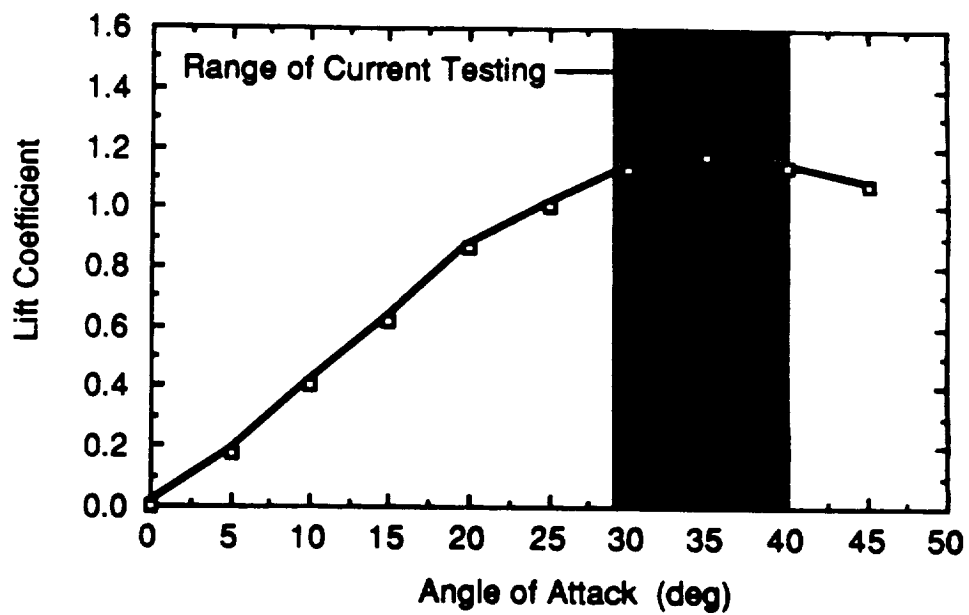


Figure 1.3

Lift Coefficient as a Function of Angle of Attack for a 70° Leading Edge Sweep Delta Wing. Courtesy of McKernan, 1983.

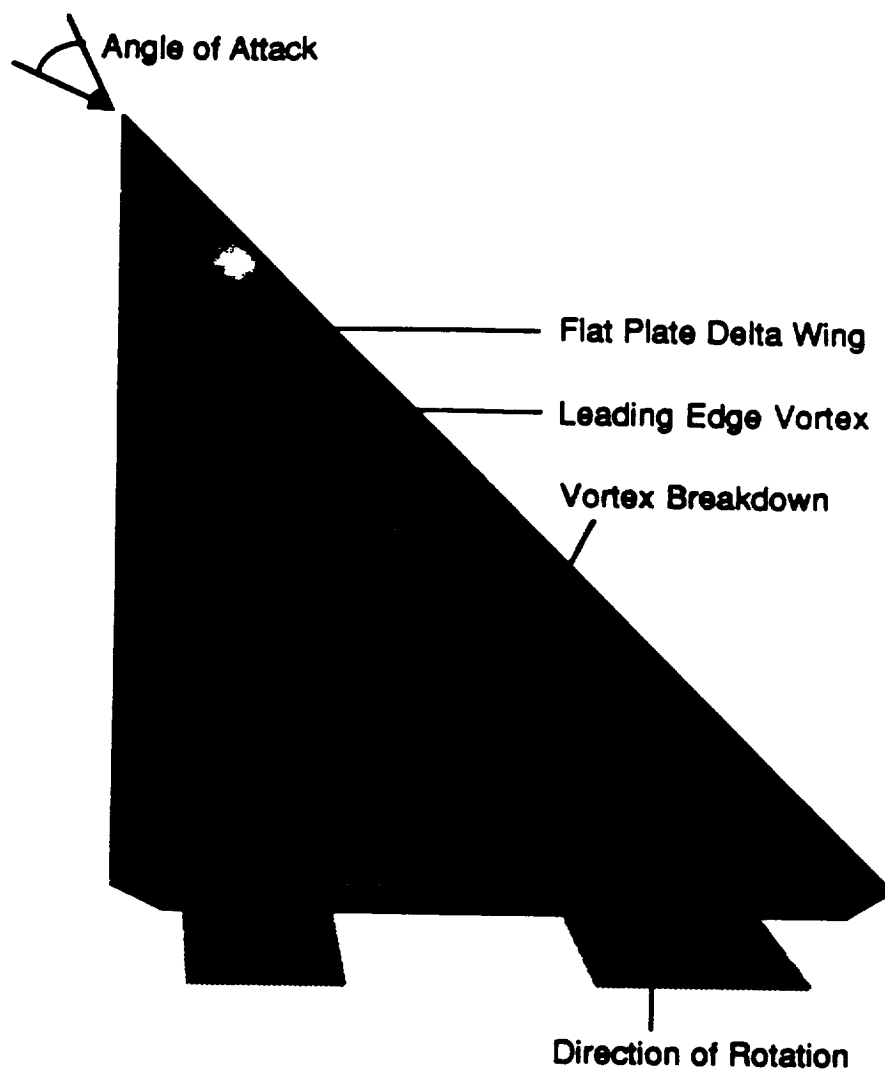


Figure 1.4

Schematic of Leading Edge Vortex Breakdown.

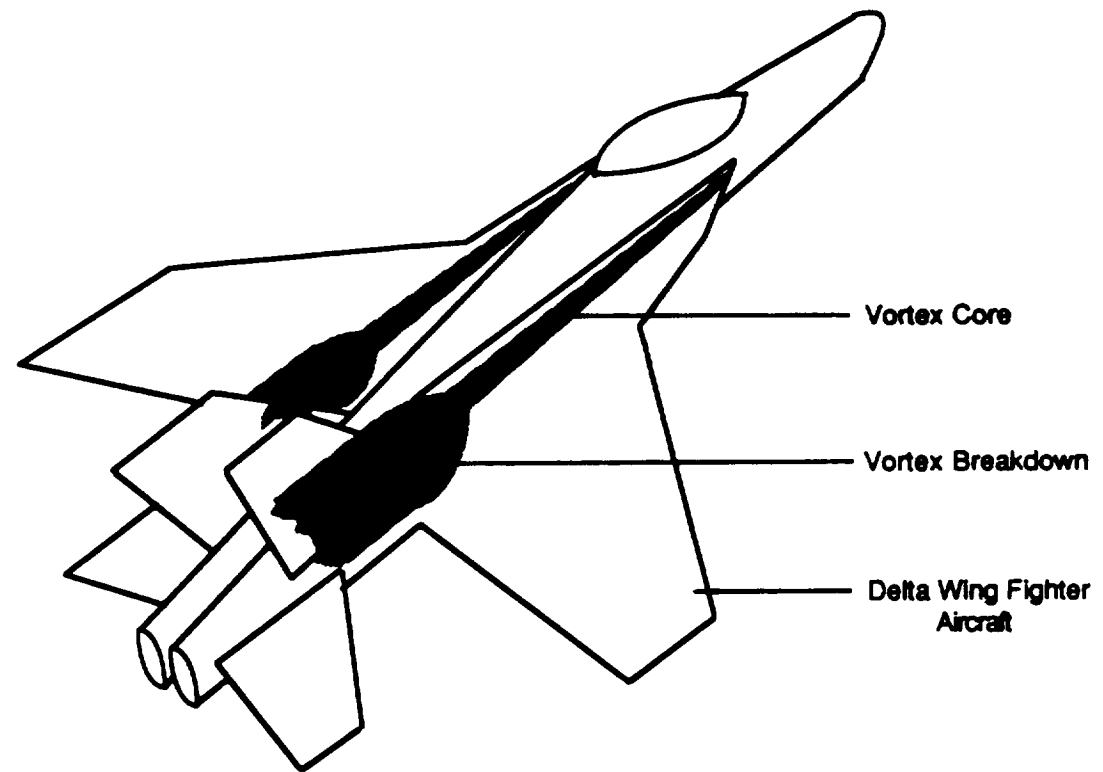


Figure 1.5

Vortex Breakdown Occuring on Delta Wing Fighter Aircraft.

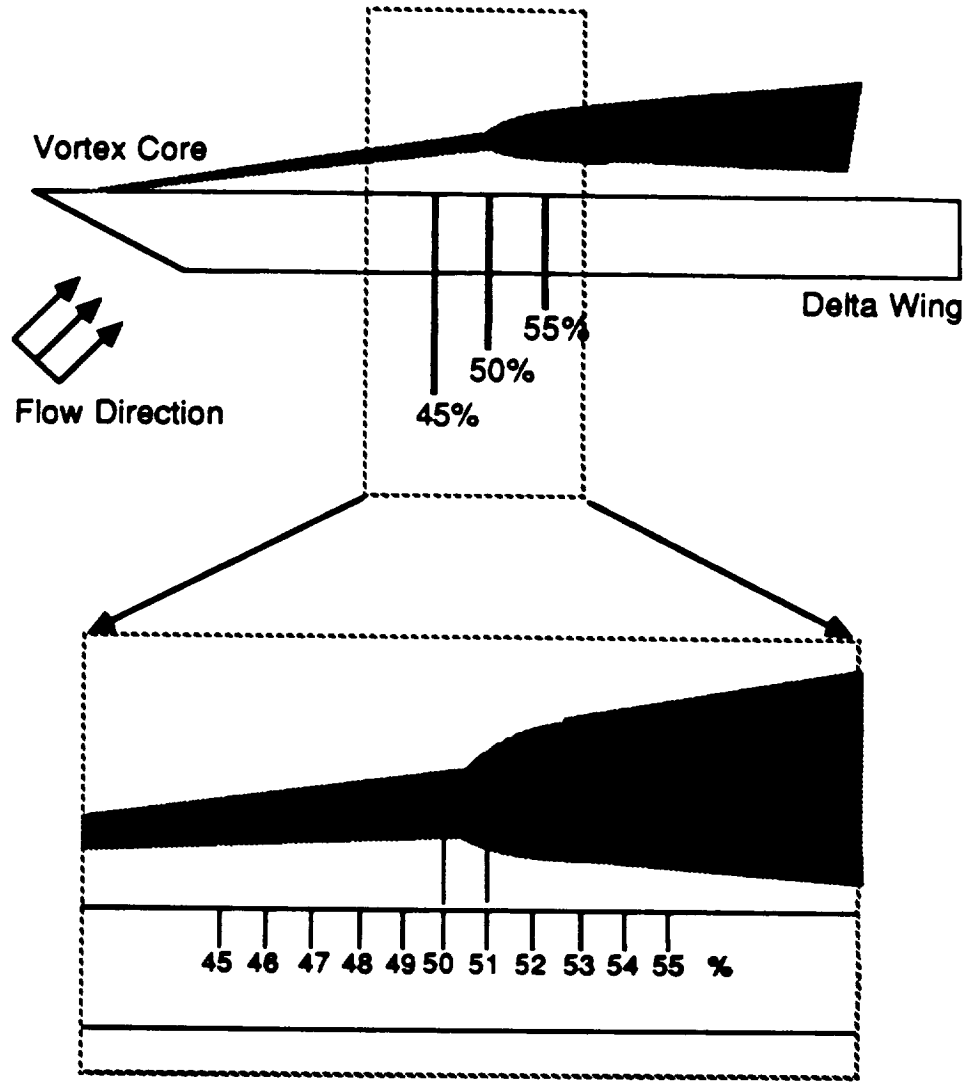


Figure 1.6 Schematic of Vortex Breakdown Area

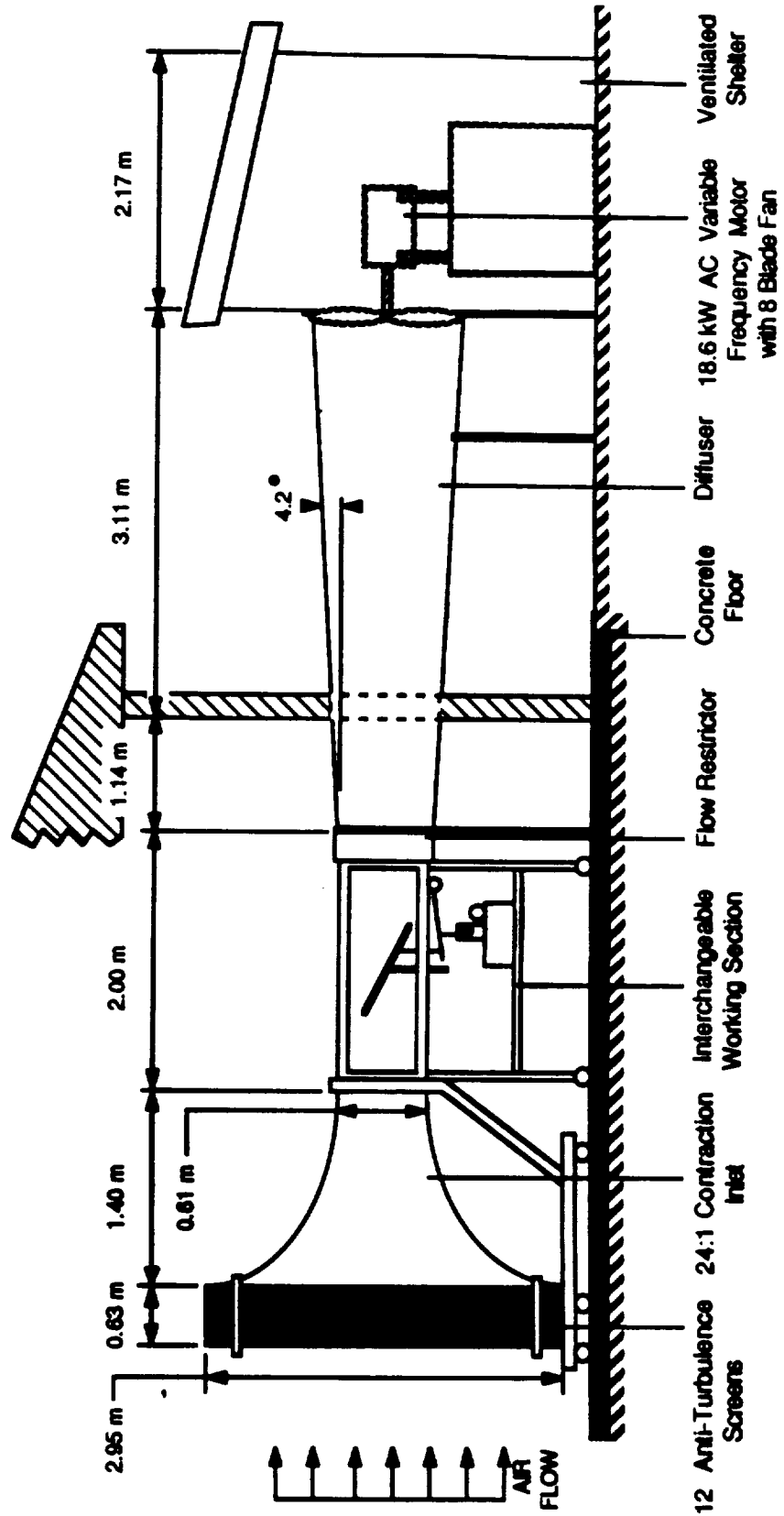


Figure 2.1 Low Speed Wind Tunnel Facility.

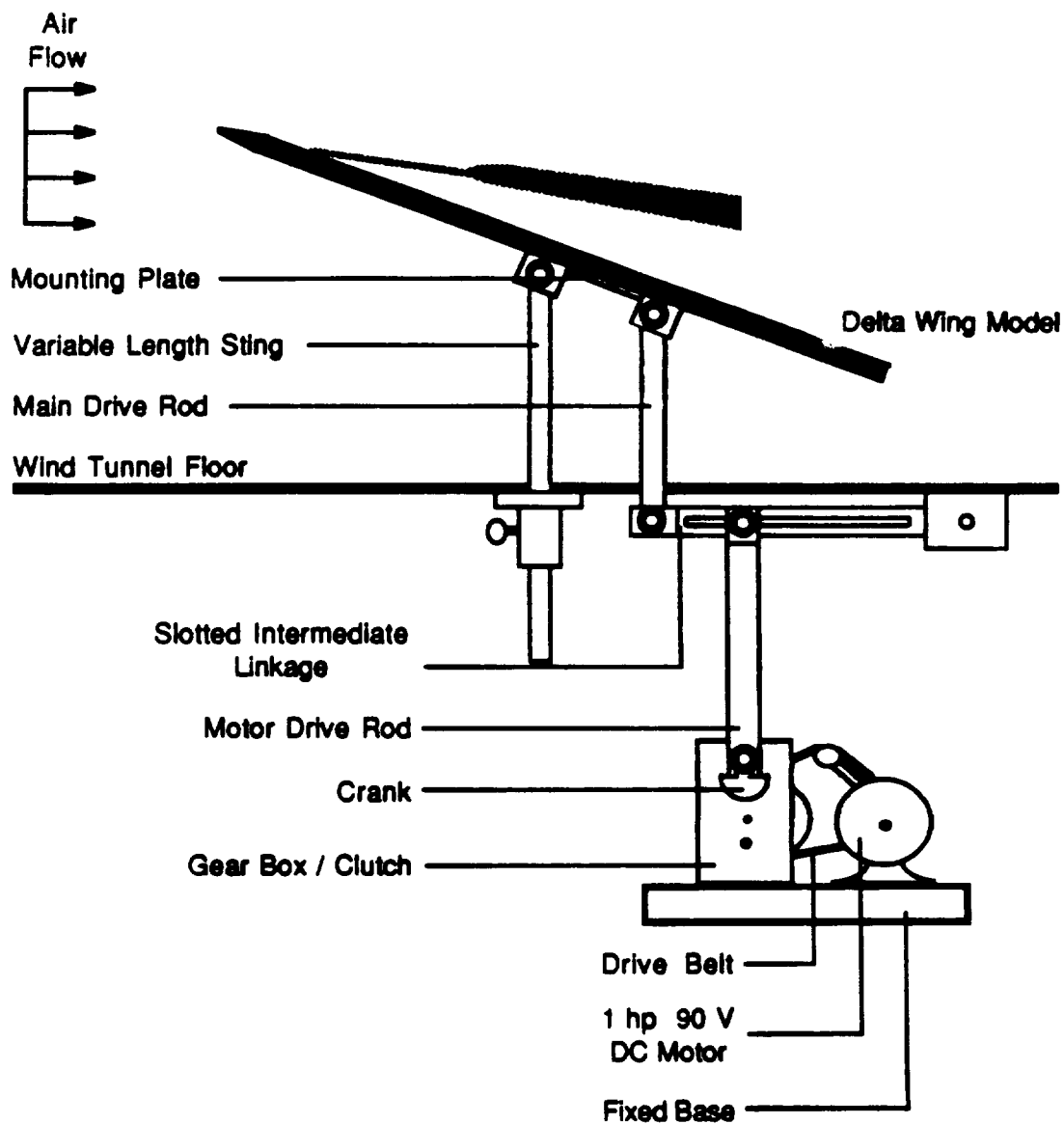


Figure 2.2

Unsteady Pitching Mechanism.
(Adapted from LeMay 1988)

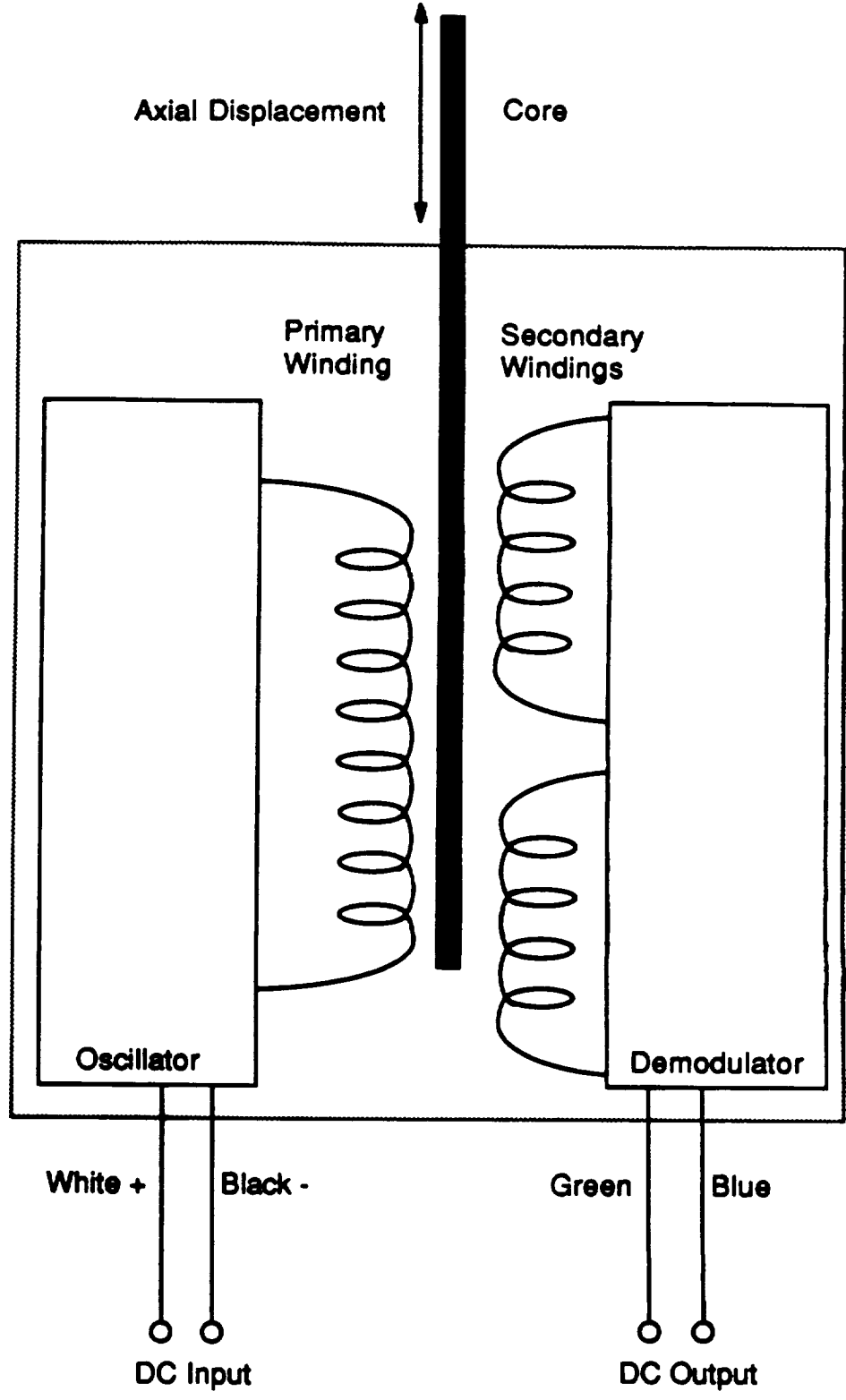


Figure 2.3 Displacement Transducer : Schematic.

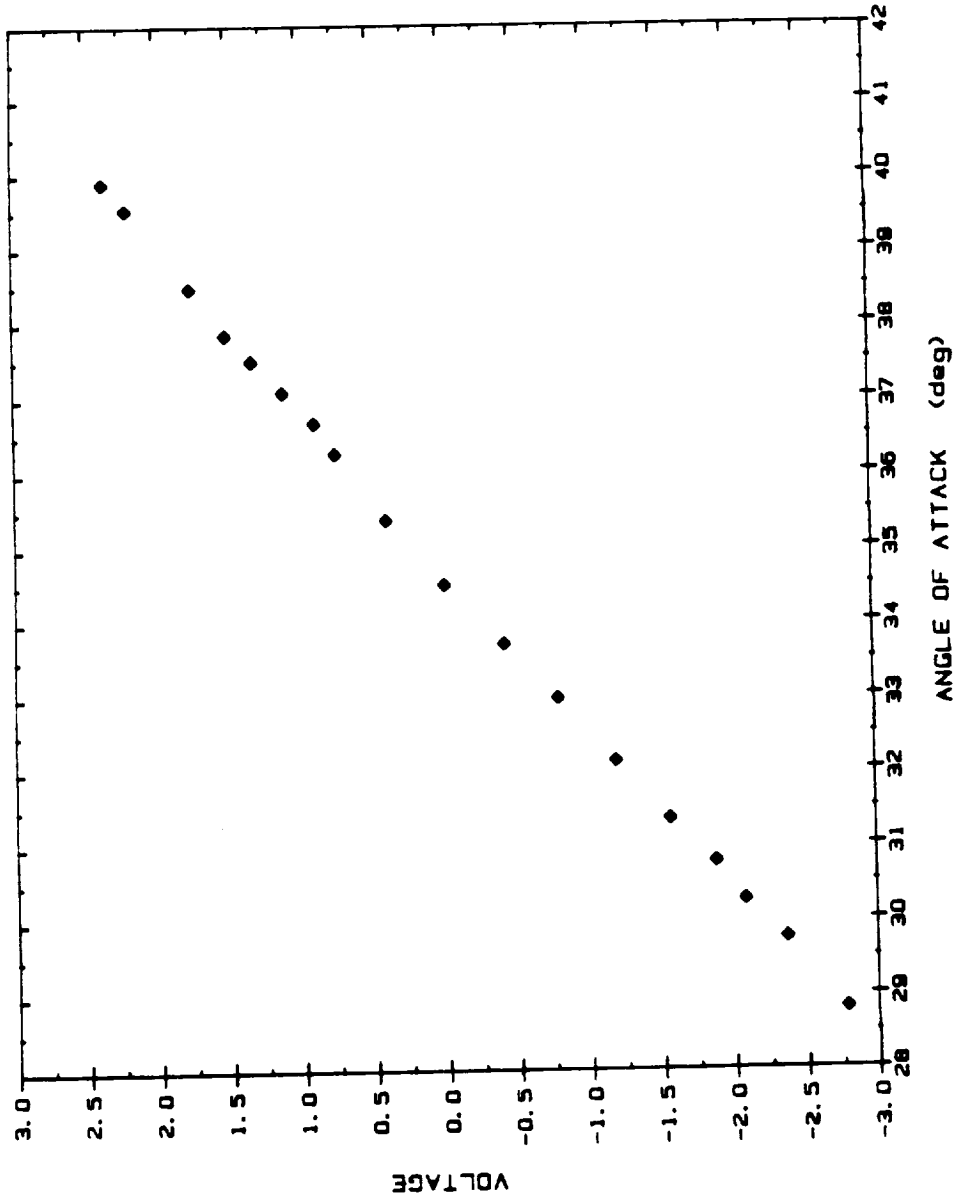


Figure 2.4 Displacement Transducer Calibration Curve.

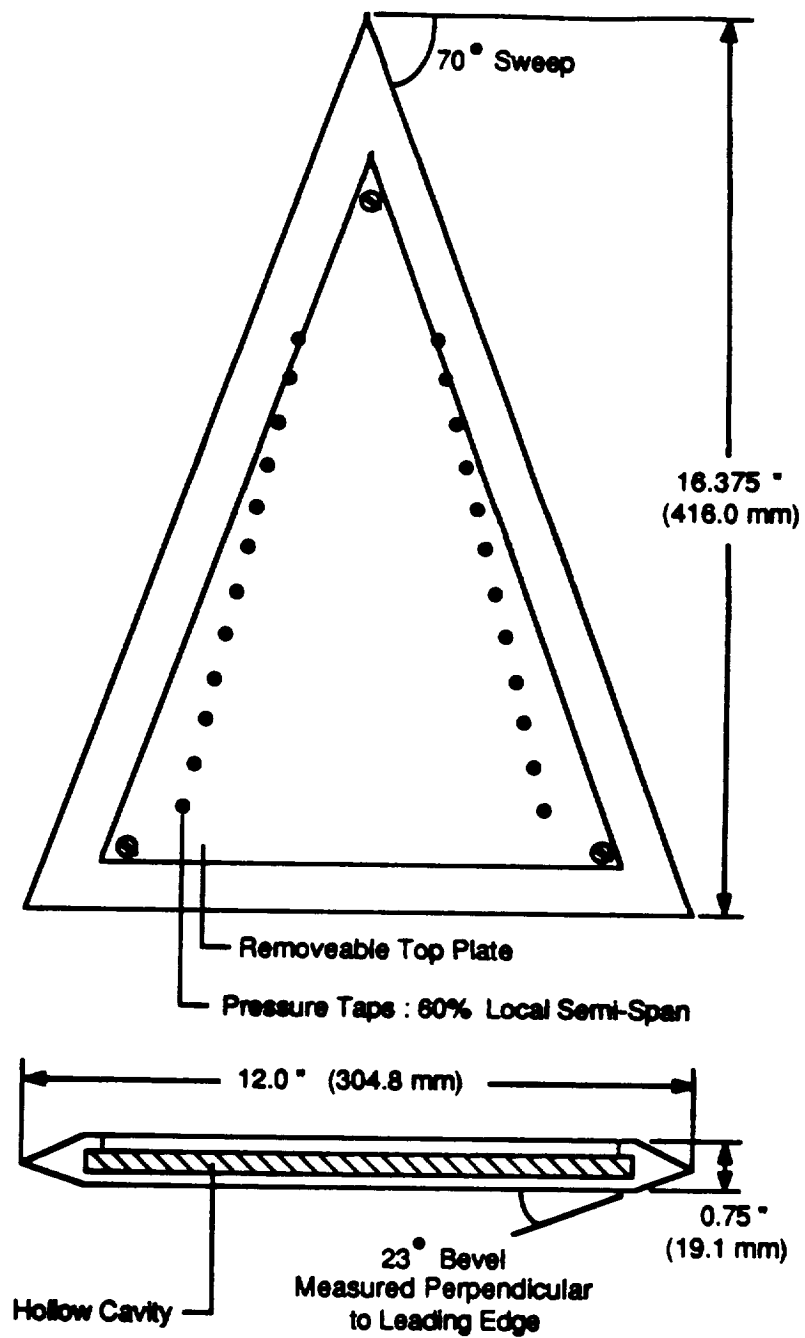


Figure 2.5

Delta Wing Pressure Model.

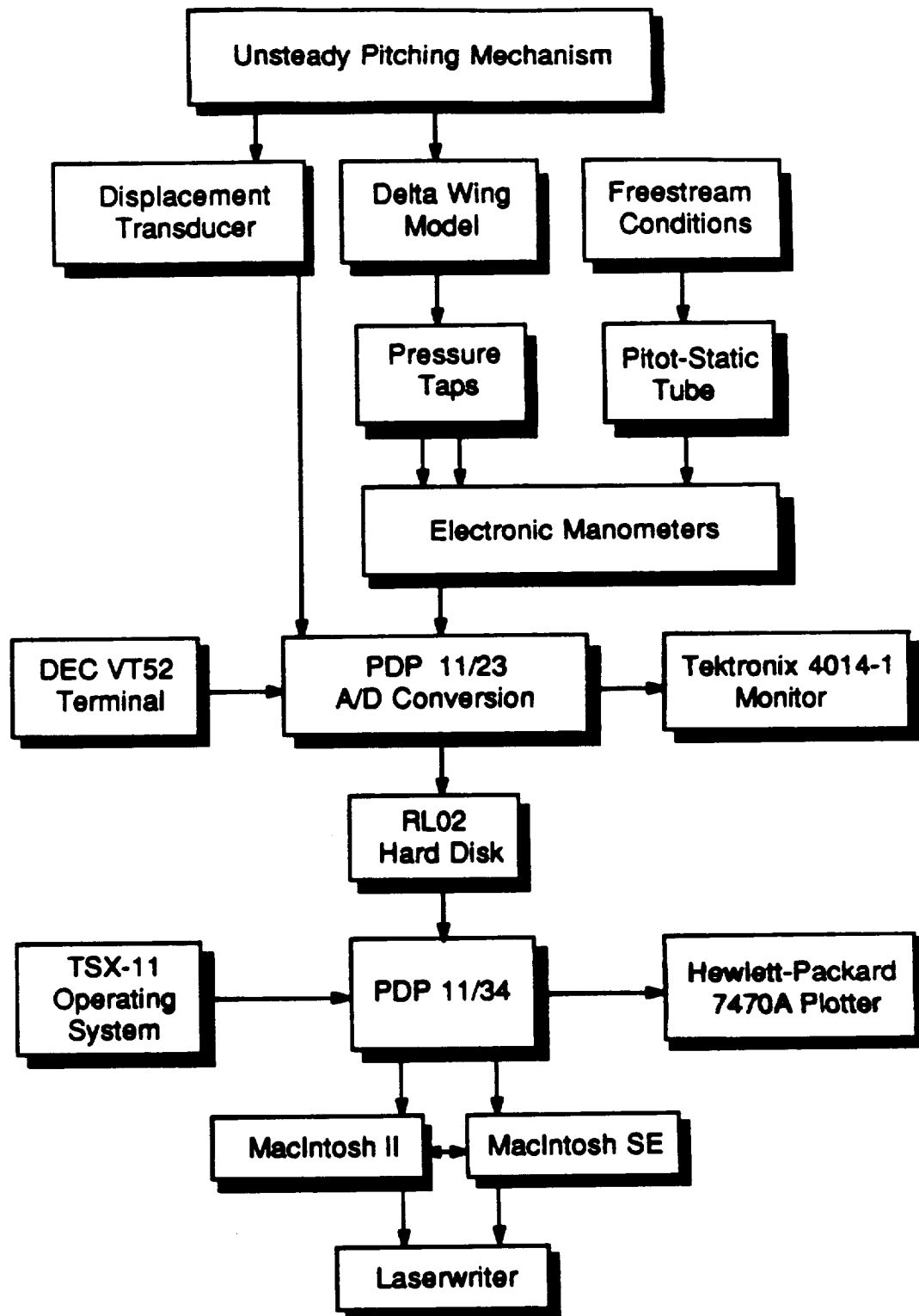


Figure 2.6

Data Aquisition Flowchart.

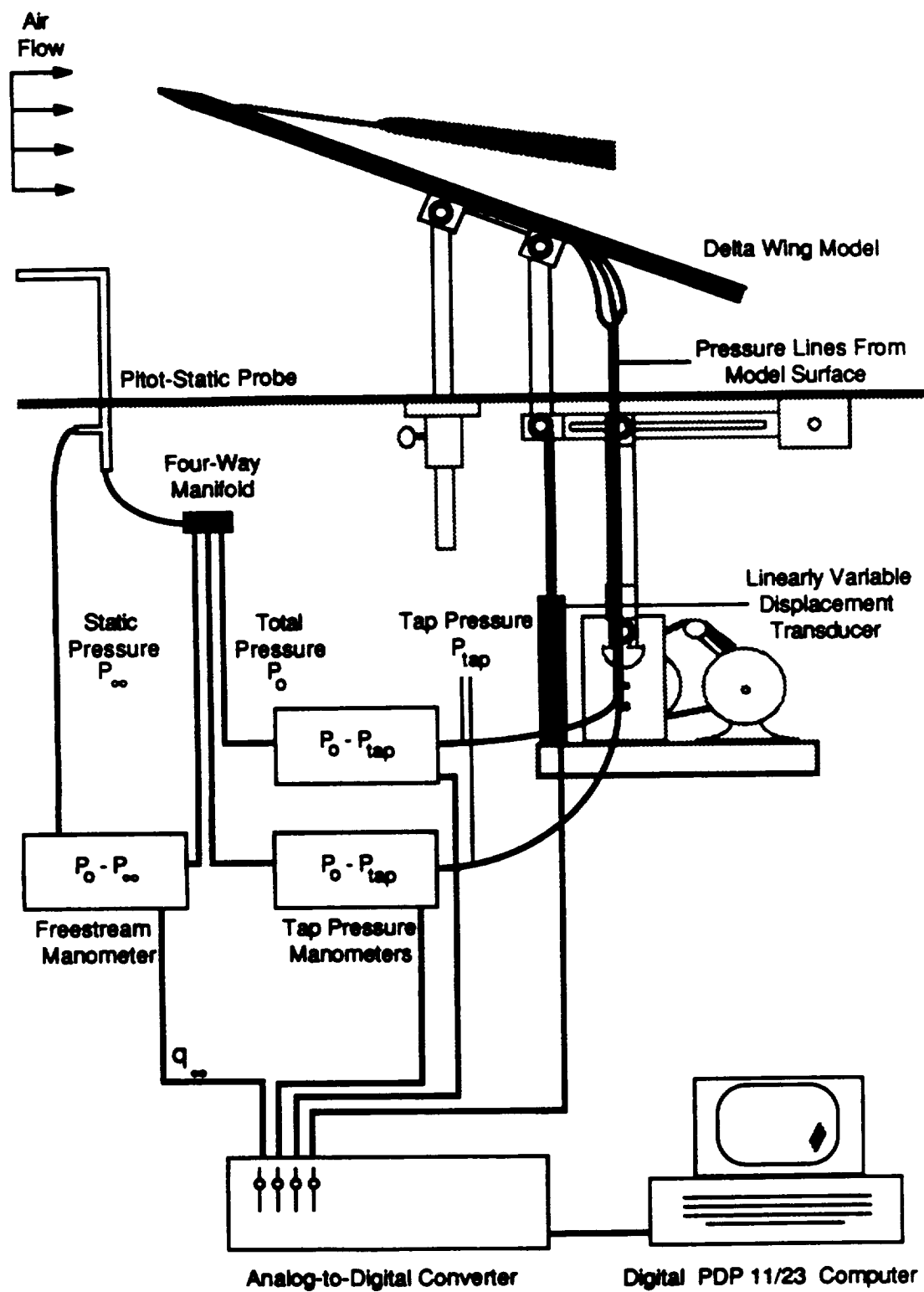
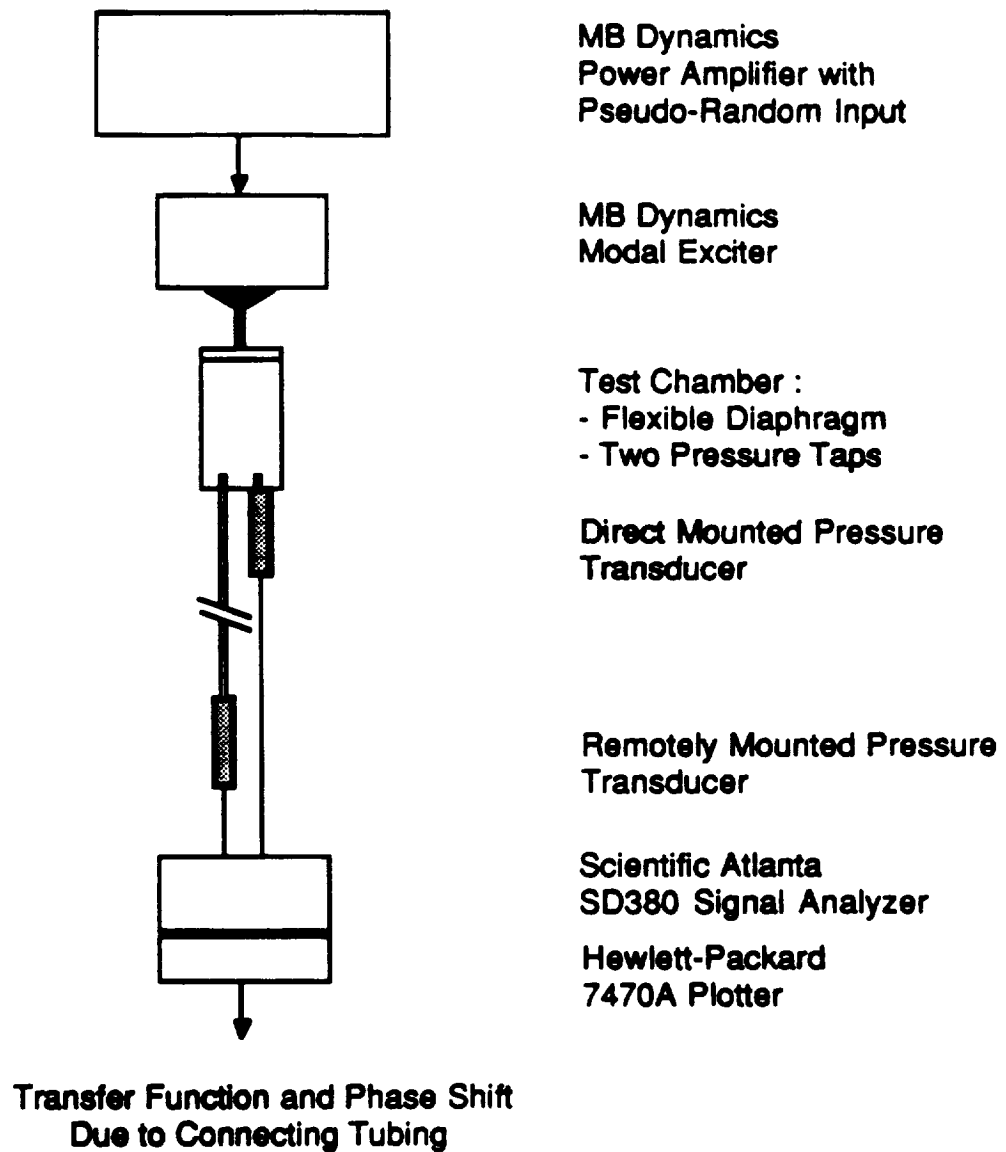


Figure 3.1

Experimental Set-Up.



**Figure 3.2 Experimental Set-Up for Preliminary Tubing
Transfer Function Analysis.**

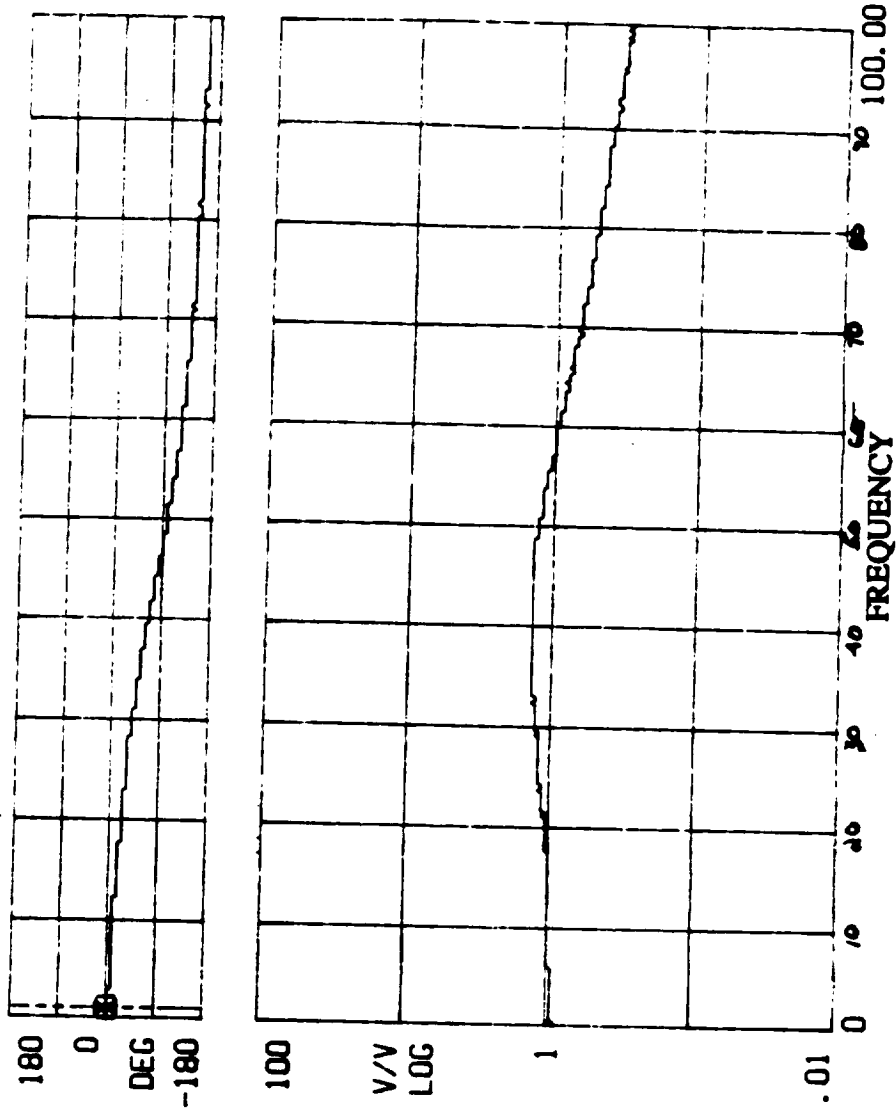


Figure 3.3 Frequency Response for Manometers and Tubing Used to Measure Fluctuating Surface Pressures : Transfer Function and Phase Shift up to 100 Hz.

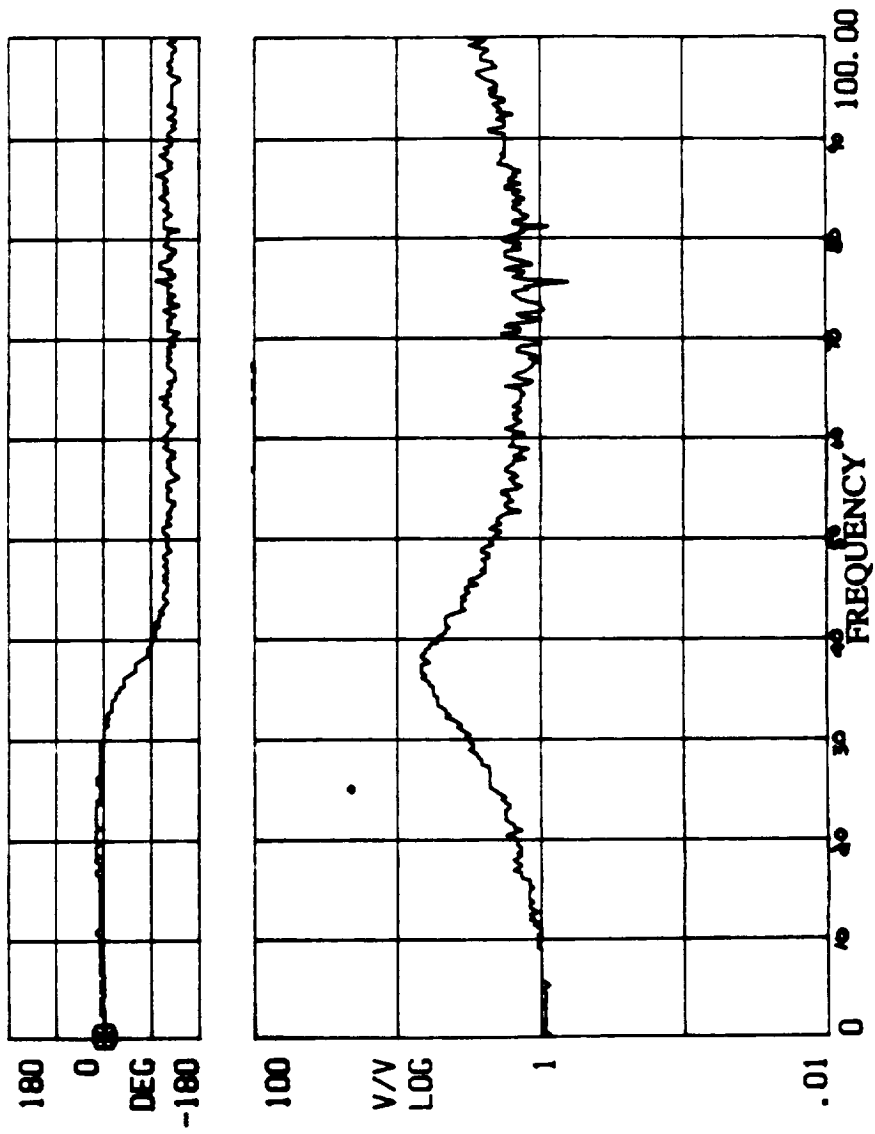


Figure 3.4 Frequency Response for Manometers and Tubing Used to Measure Freestream Dynamic Pressure : Transfer Function and Phase Shift up to 100 Hz.

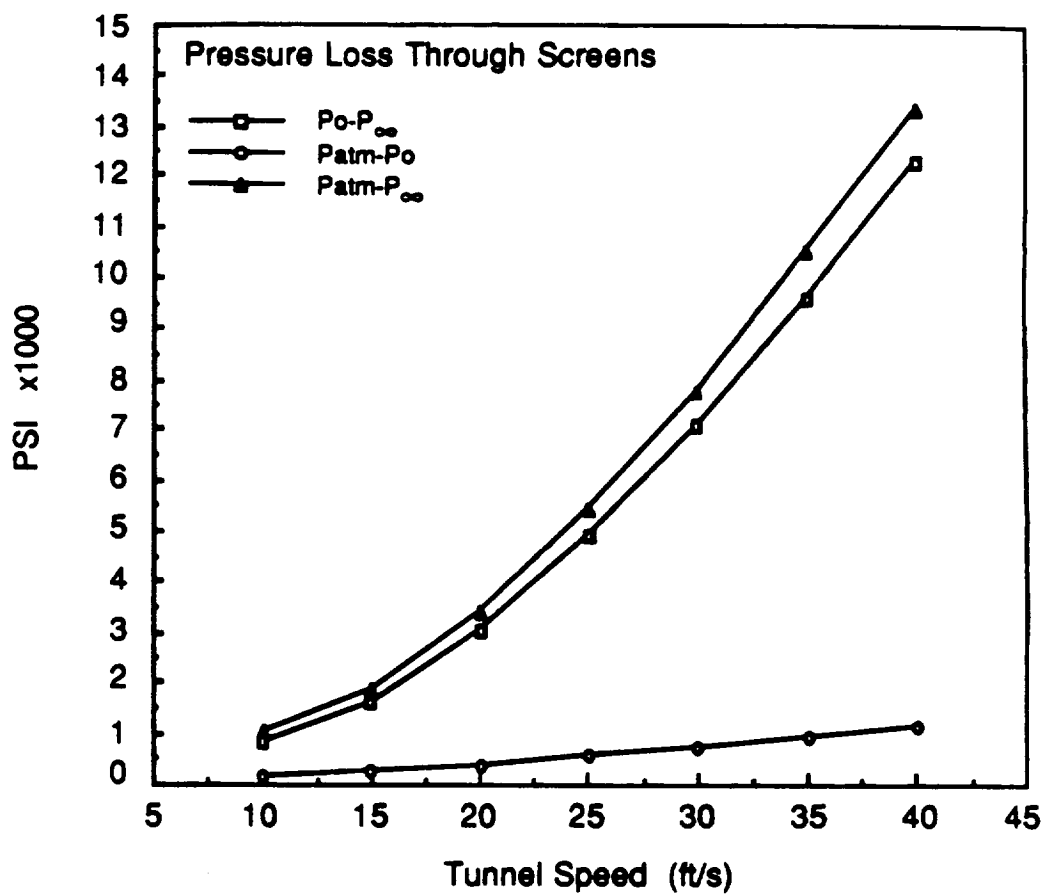


Figure 3.5

Dynamic Pressure Loss Through Wind Tunnel Screens.

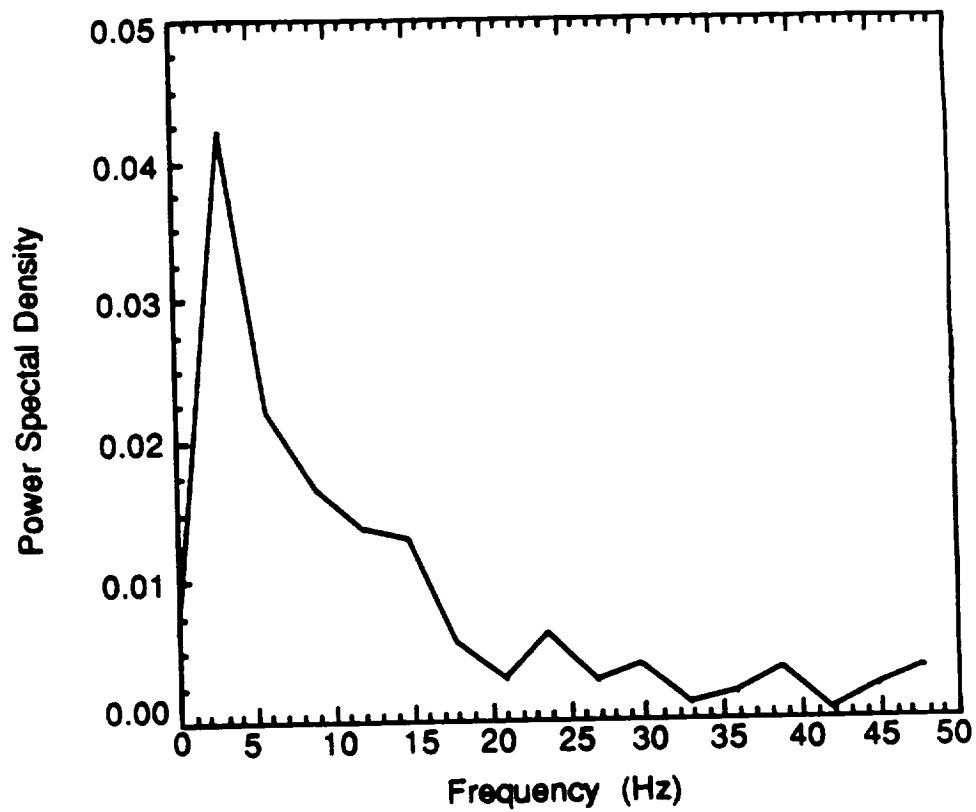


Figure 3.6

Discrete Fourier Transform of Unsteady Pressure
Data : $Re = 500,000$, $U = 60$ ft/s , $k = 0.30$.

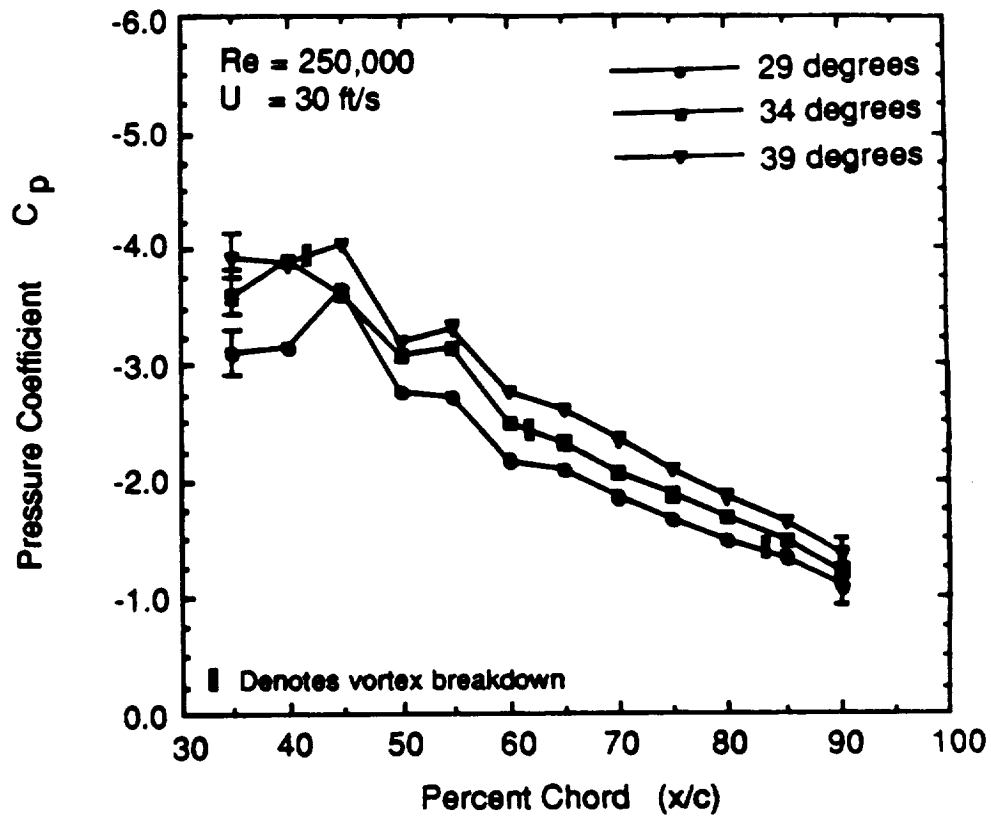


Figure 4.1

Static Data : U = 30 ft/s , $\alpha = 29^\circ, 34^\circ, 39^\circ$

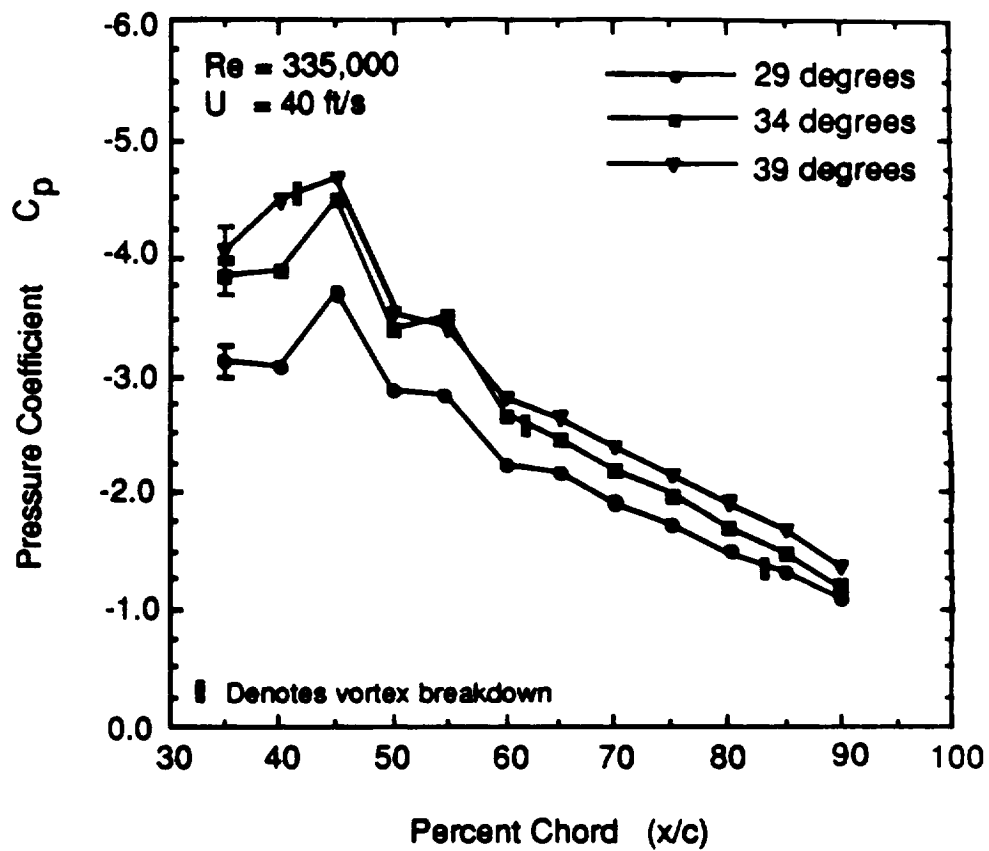


Figure 4.2

Static Data : U = 40 ft/s , $\alpha = 29^\circ, 34^\circ, 39^\circ$

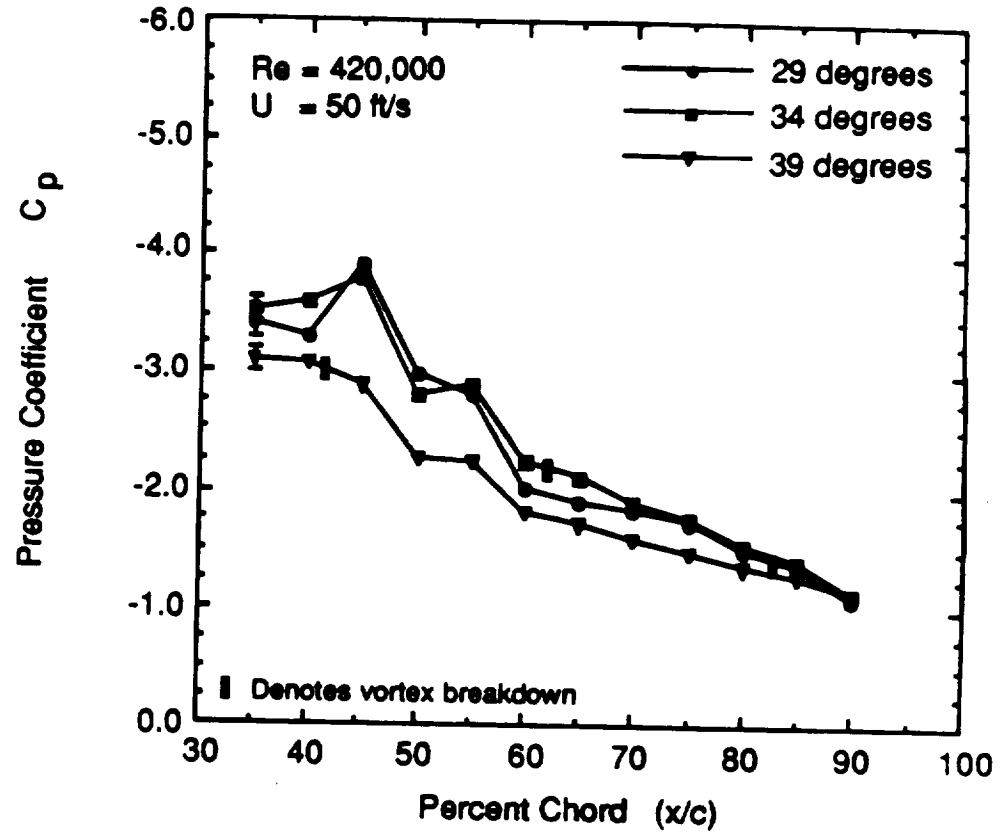


Figure 4.3

Static Data : $U = 50 \text{ ft/s}$, $\alpha = 29^\circ, 34^\circ, 39^\circ$

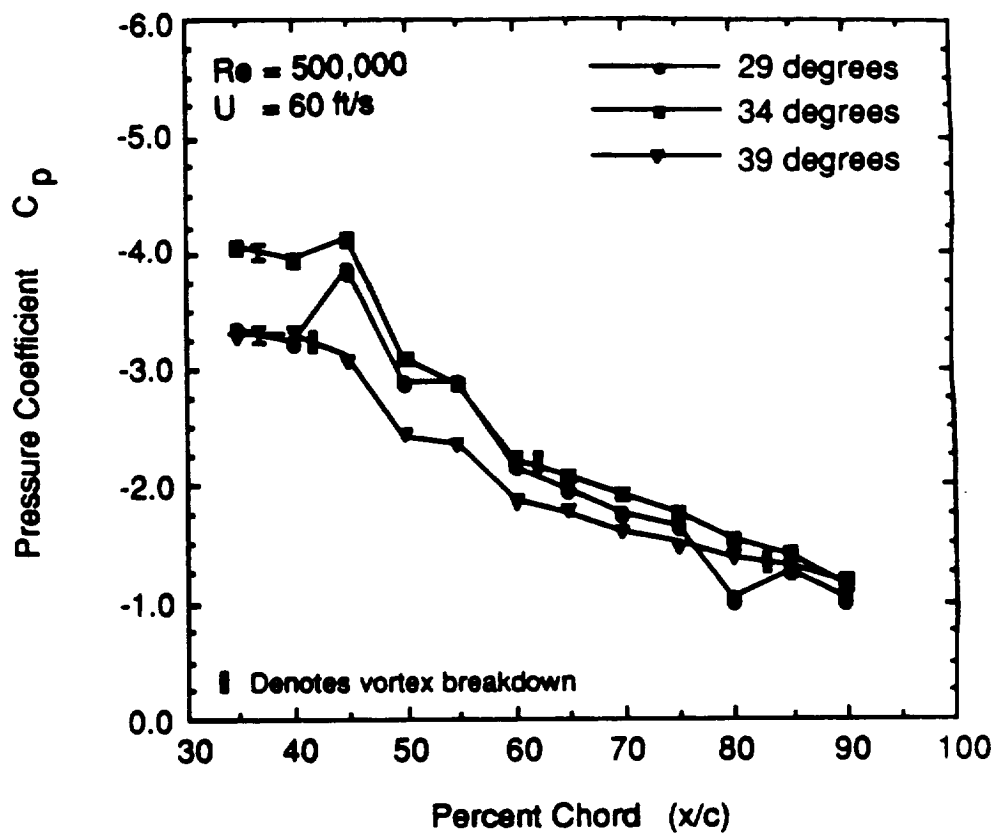


Figure 4.4

Static Data : $U = 60 \text{ ft/s}$, $\alpha = 29^\circ, 34^\circ, 39^\circ$

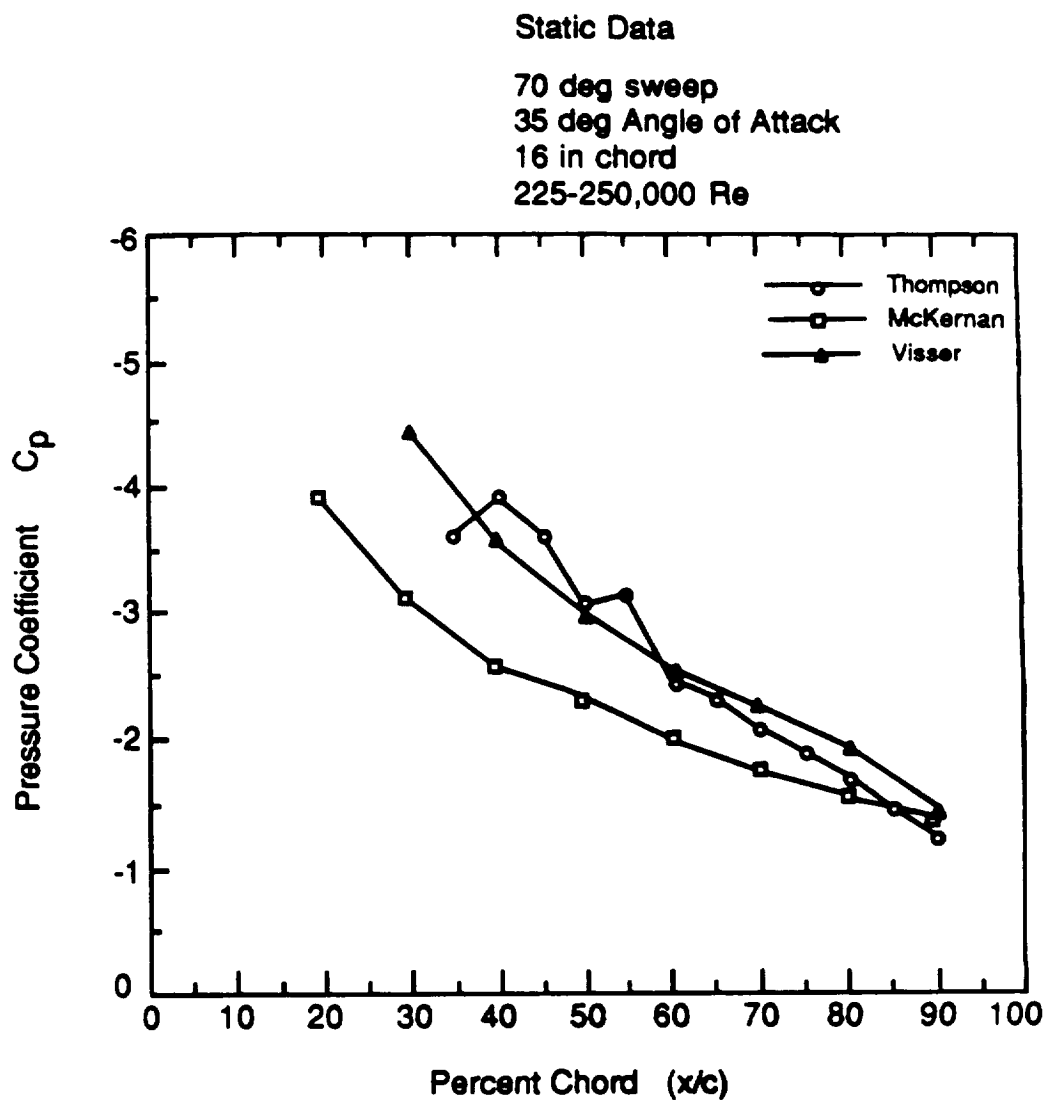


Figure 4.5

Comparison Between Current Static Data and McKernan (1983) and Visser (1989).

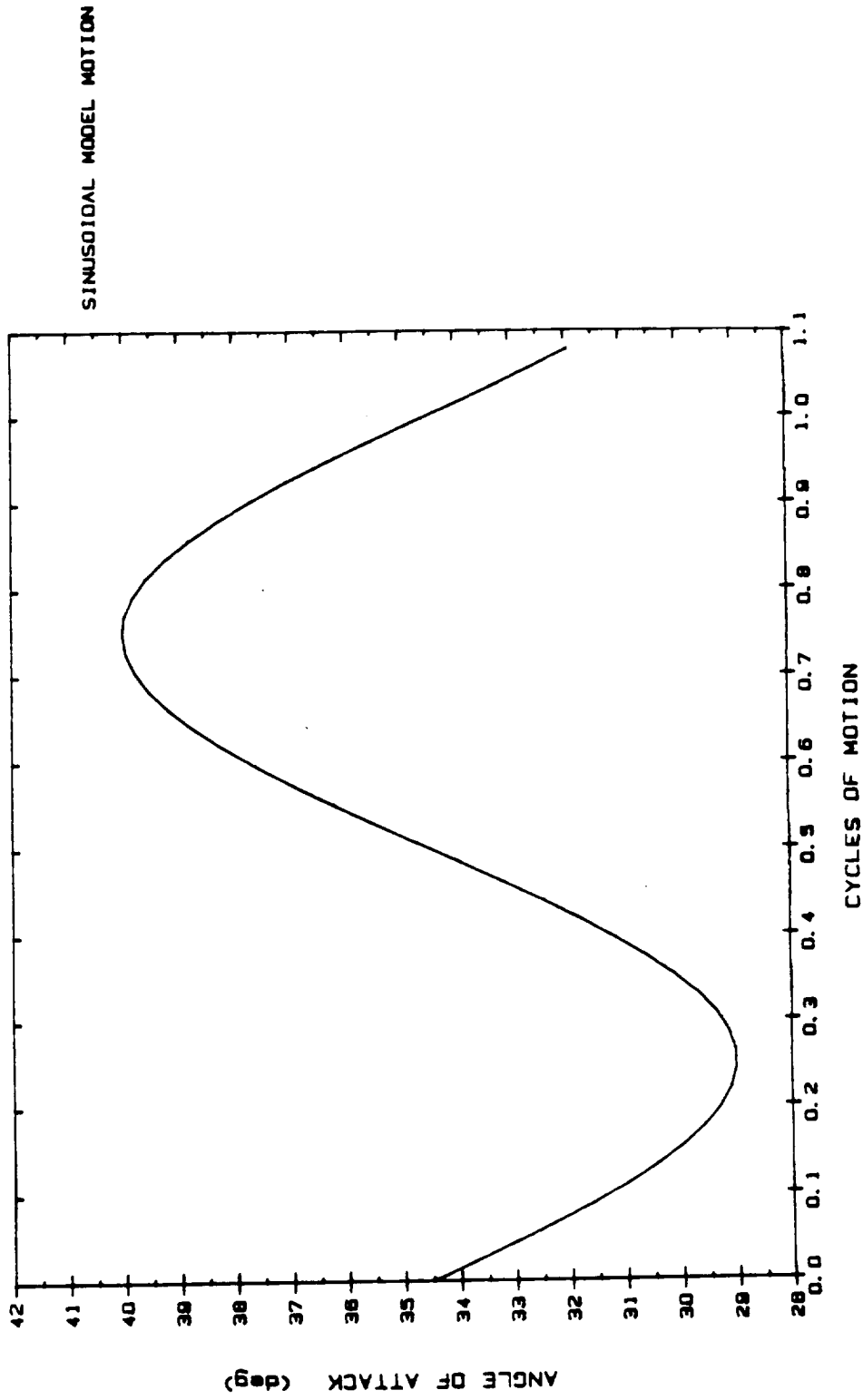
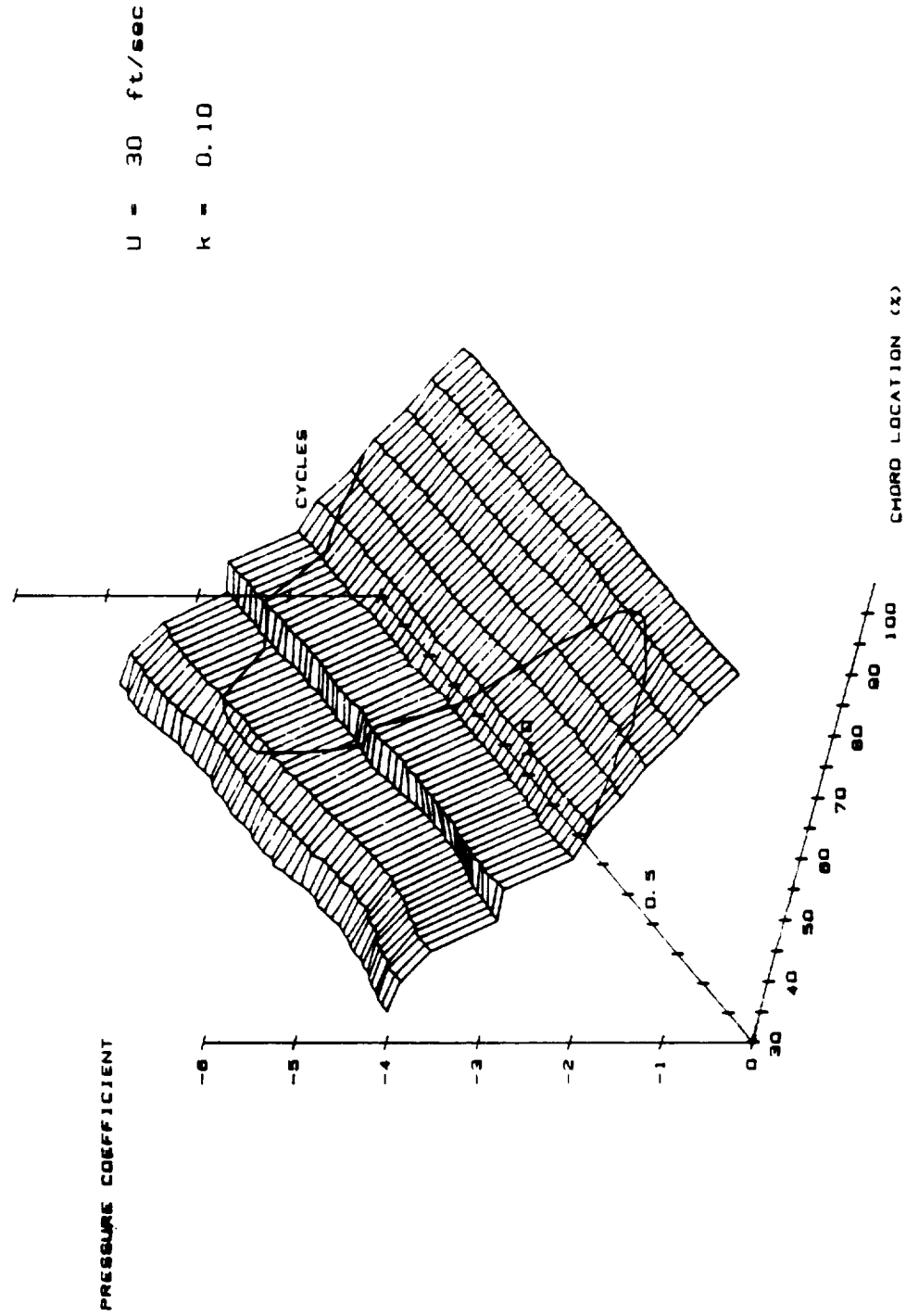
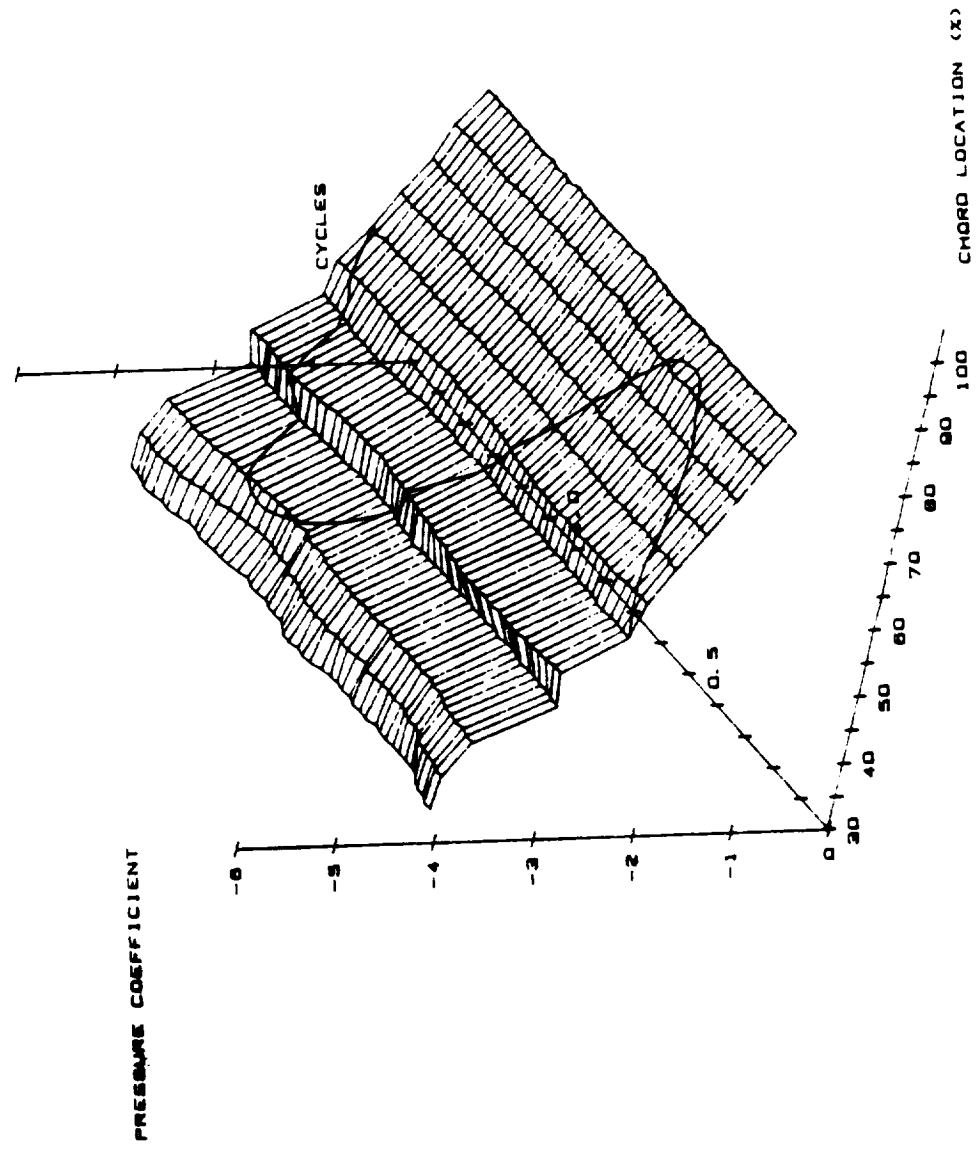


Figure 4.6 Angle of Attack Time History for Unsteady Model Motion.



$U = 30 \text{ ft/sec}$
 $k = 0.20$



Unsteady Pressure Data : Pressure Coefficient as a function of Time and Chord Location. $Re = 250,000$, $U = 30 \text{ ft/s}$, $k = 0.20$

Figure 4.8

$U = 30 \text{ ft/sec}$
 $k = 0.30$

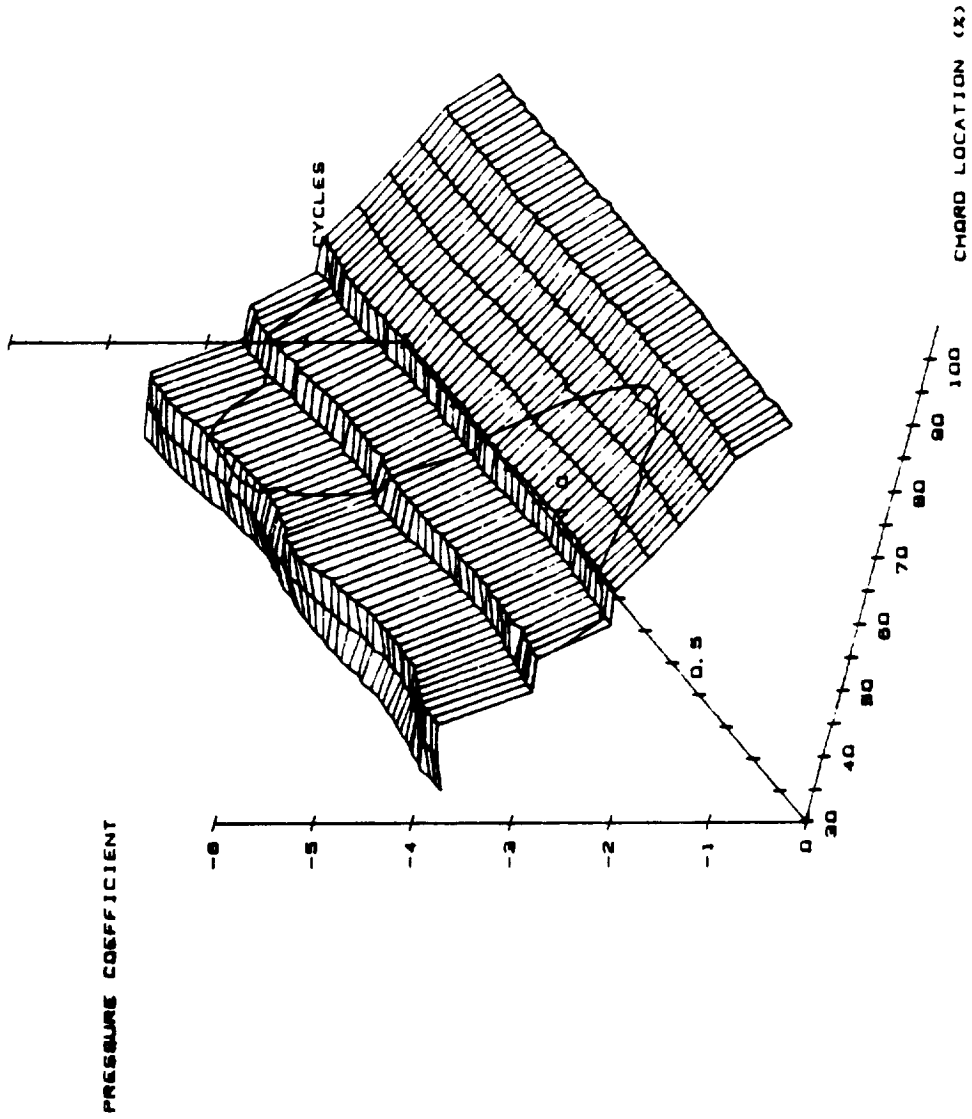


Figure 4.9 Unsteady Pressure Data : Pressure Coefficient as a function of Time and Chord Location. $Re = 250,000$, $U = 30 \text{ ft/s}$, $k = 0.30$

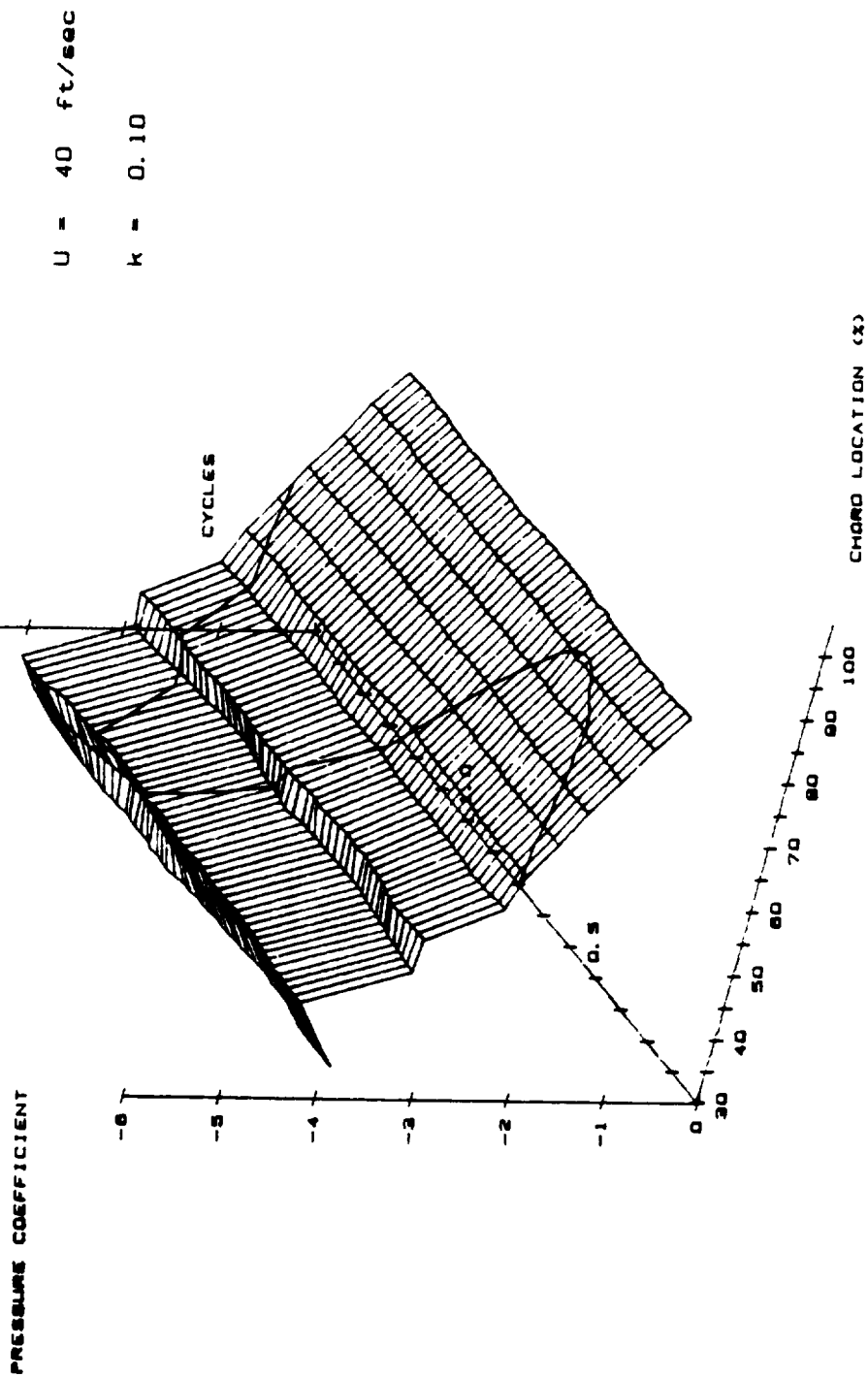


Figure 4.10 Unsteady Pressure Data : Pressure Coefficient as a function of Time and Chord Location. $Re = 335,000$, $U = 40 \text{ ft/s}$, $k = 0.10$

U = 40 ft/sec
 k = 0.20

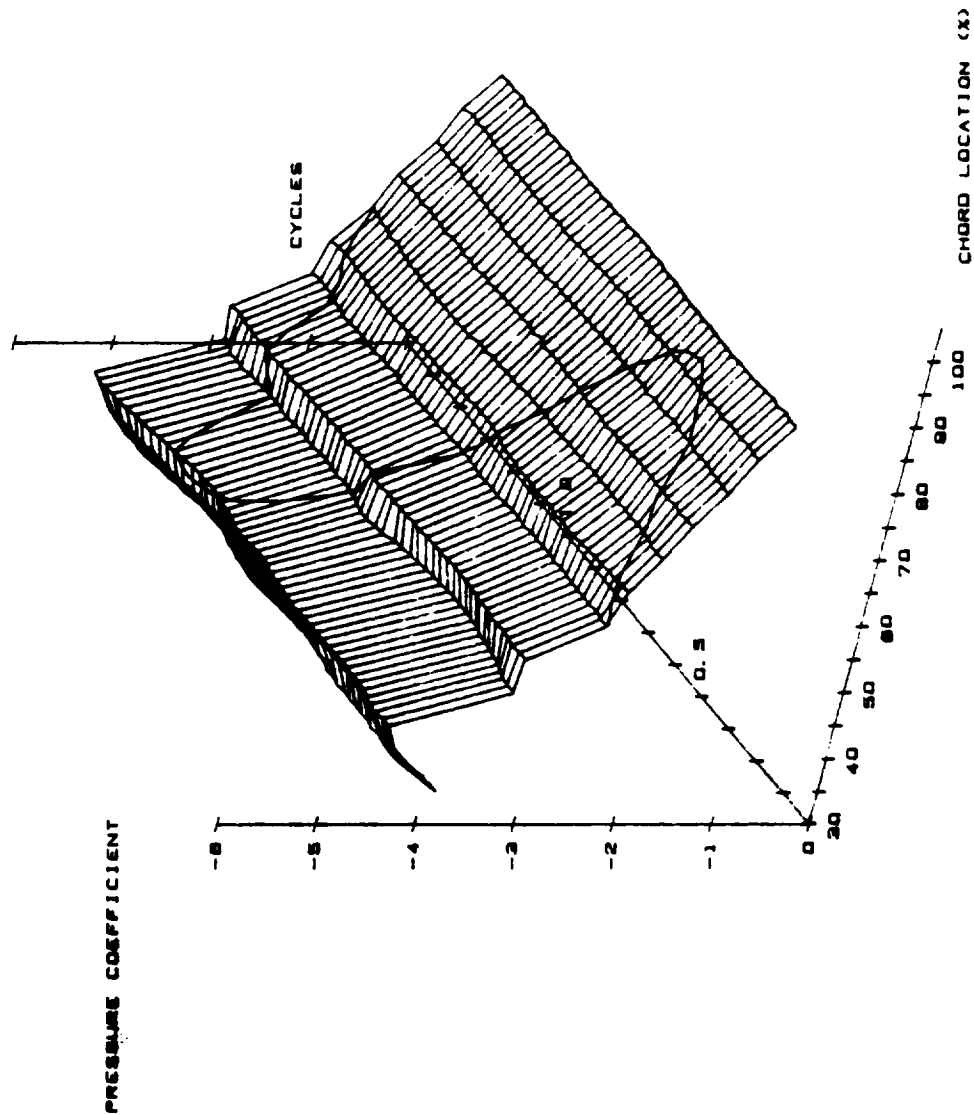


Figure 4.11 Unsteady Pressure Data : Pressure Coefficient as a function of Time and Chord Location. $Re = 335,000$, $U = 40$ ft/s, $k = 0.20$

$U = 40 \text{ ft/sec}$
 $k = 0.30$

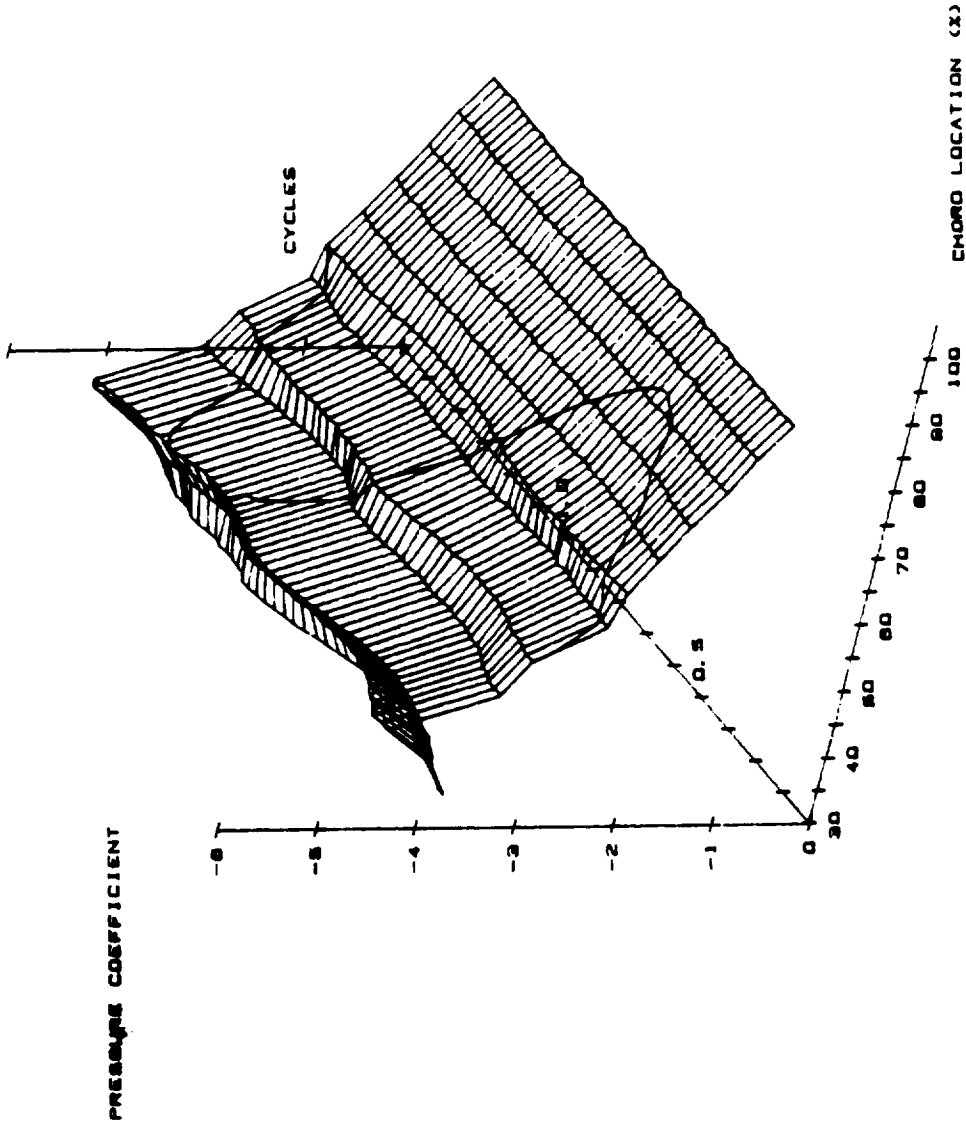


Figure 4.12 Unsteady Pressure Data : Pressure Coefficient as a function of Time and Chord Location. $Re = 335,000$, $U = 40 \text{ ft/s}$, $k = 0.30$

$U = 50 \text{ ft/sec}$
 $k = 0.10$

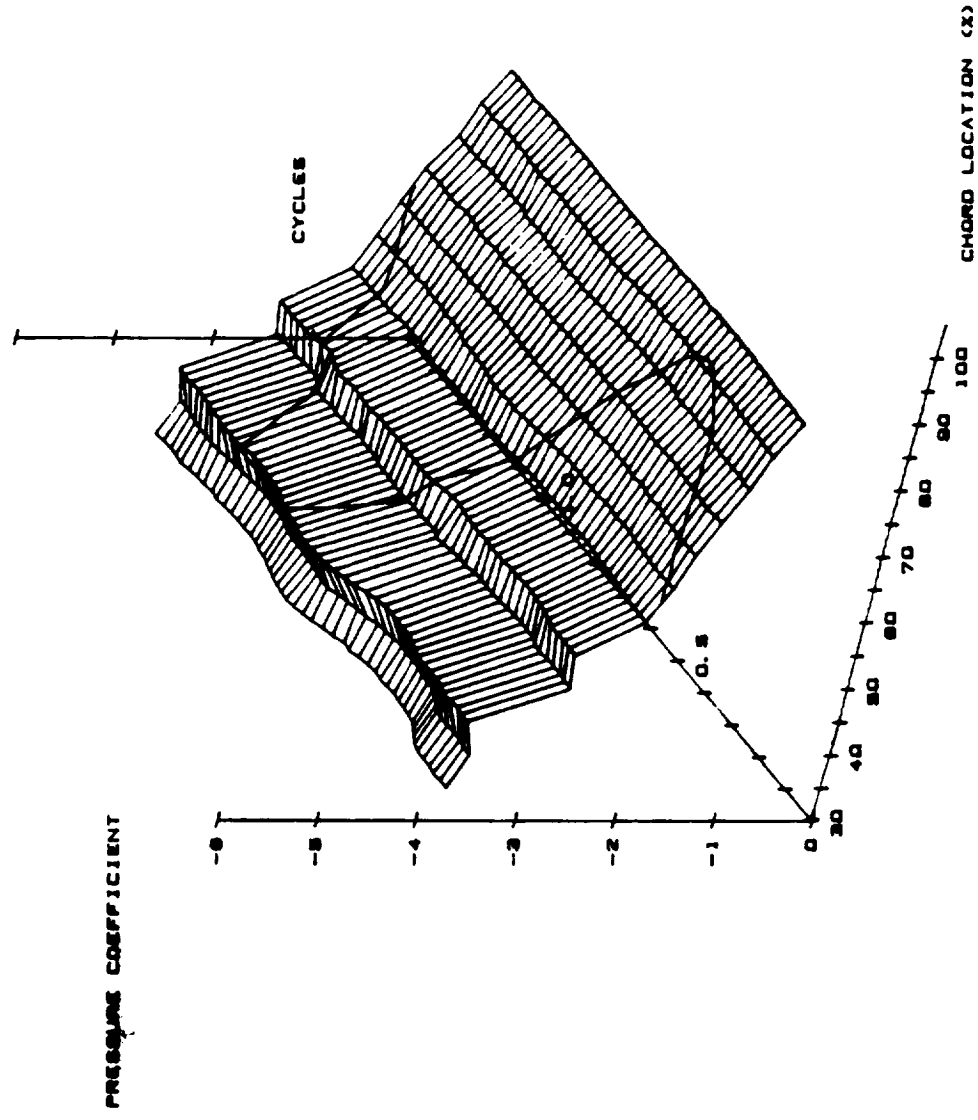
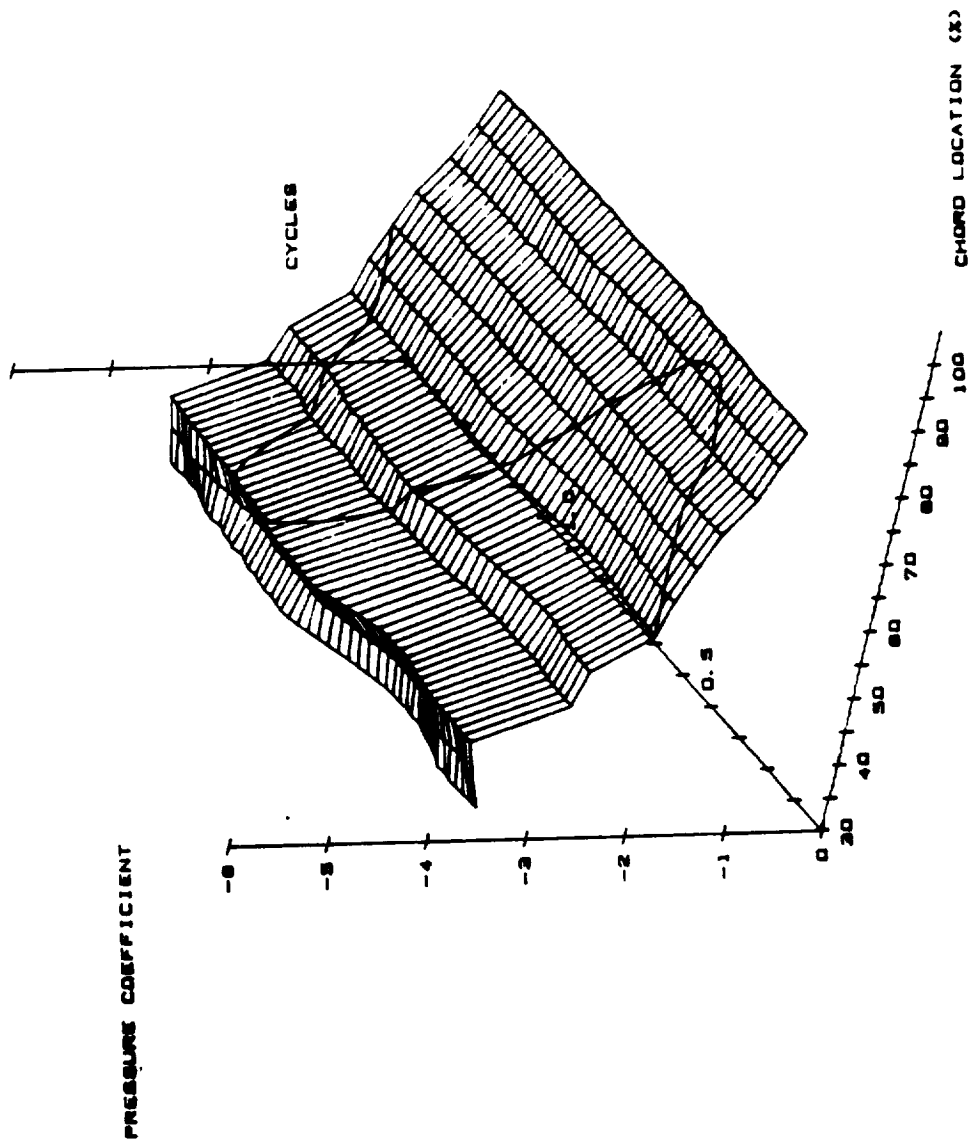


Figure 4.13 Unsteady Pressure Data : Pressure Coefficient as a function of Time and Chord Location. $Re = 420,000$, $U = 50 \text{ ft/s}$, $k = 0.10$

U = 50 ft/sec

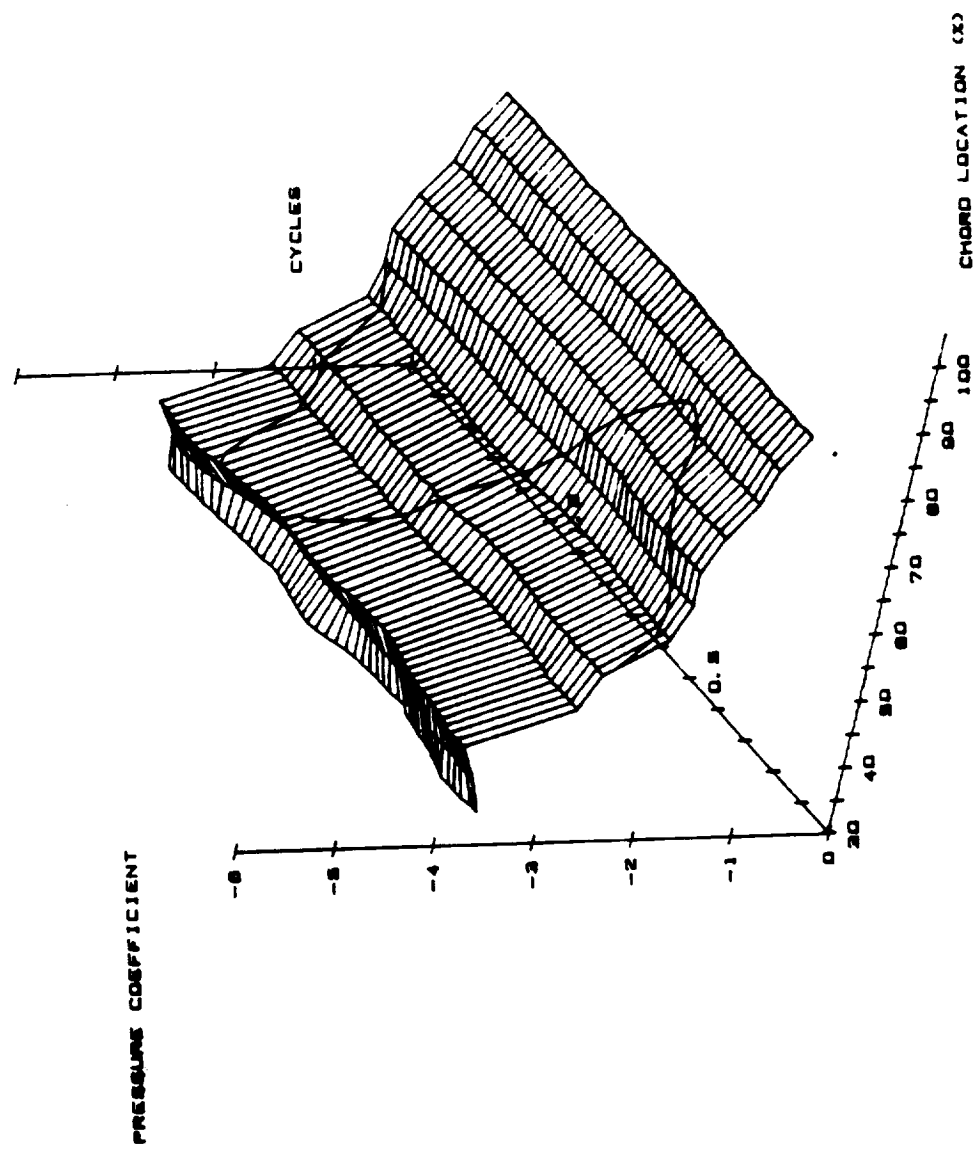
k = 0.20



Unsteady Pressure Data : Pressure Coefficient as a function of Time and Chord Location. $Re = 420,000$, $U = 50$ ft/s, $k = 0.20$

Figure 4.14

U = 50 ft/sec
k = 0.30



Unsteady Pressure Data : Pressure Coefficient as a function of Time and Chord Location. $Re = 420,000$, $U = 50$ ft/s, $k = 0.30$

Figure 4.15

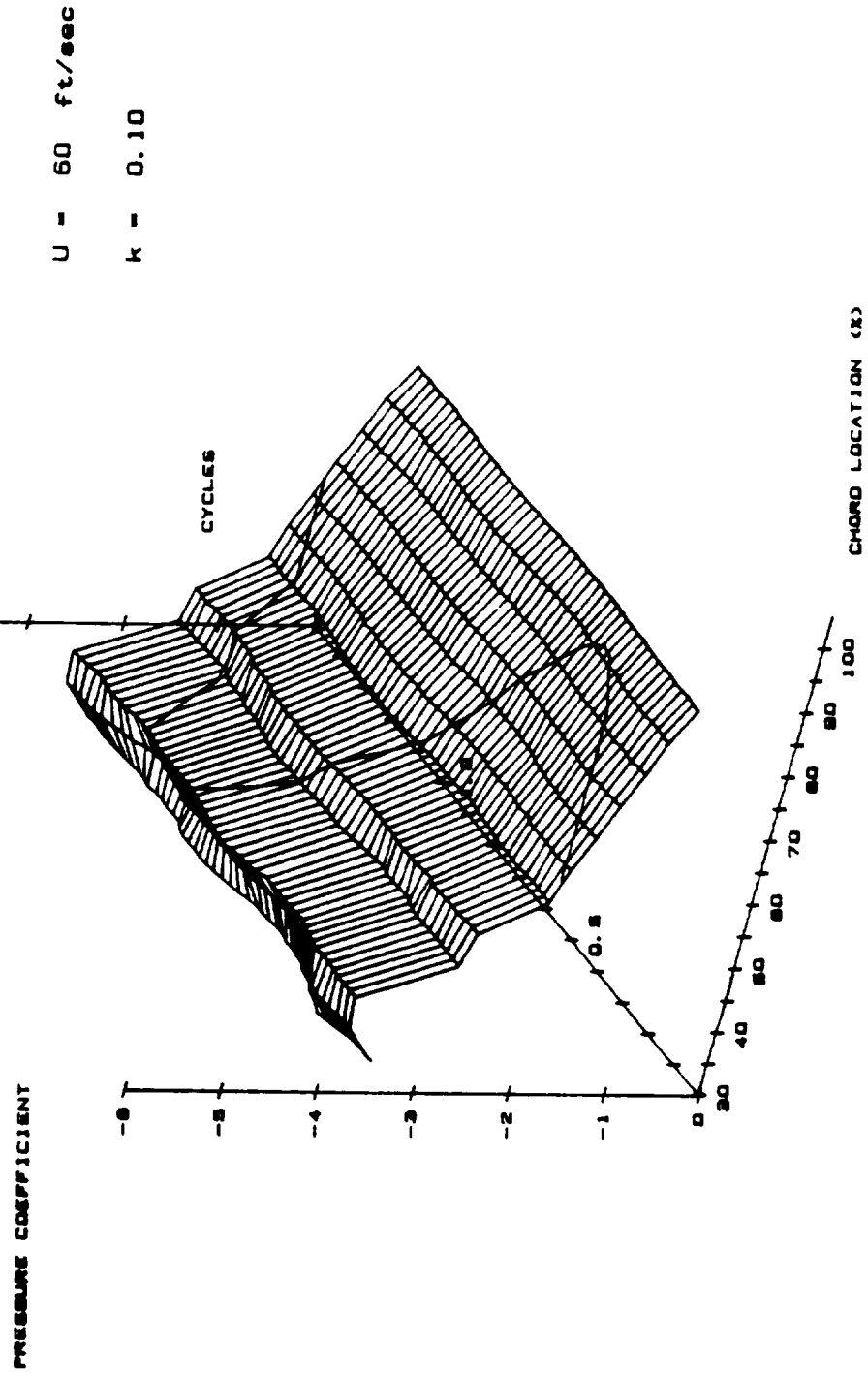


Figure 4.16 **Unsteady Pressure Data : Pressure Coefficient as a function of Time and Chord Location. $Re = 500,000$, $U = 60$ ft/s, $k = 0.10$**

U = 60 ft/sec
k = 0.20

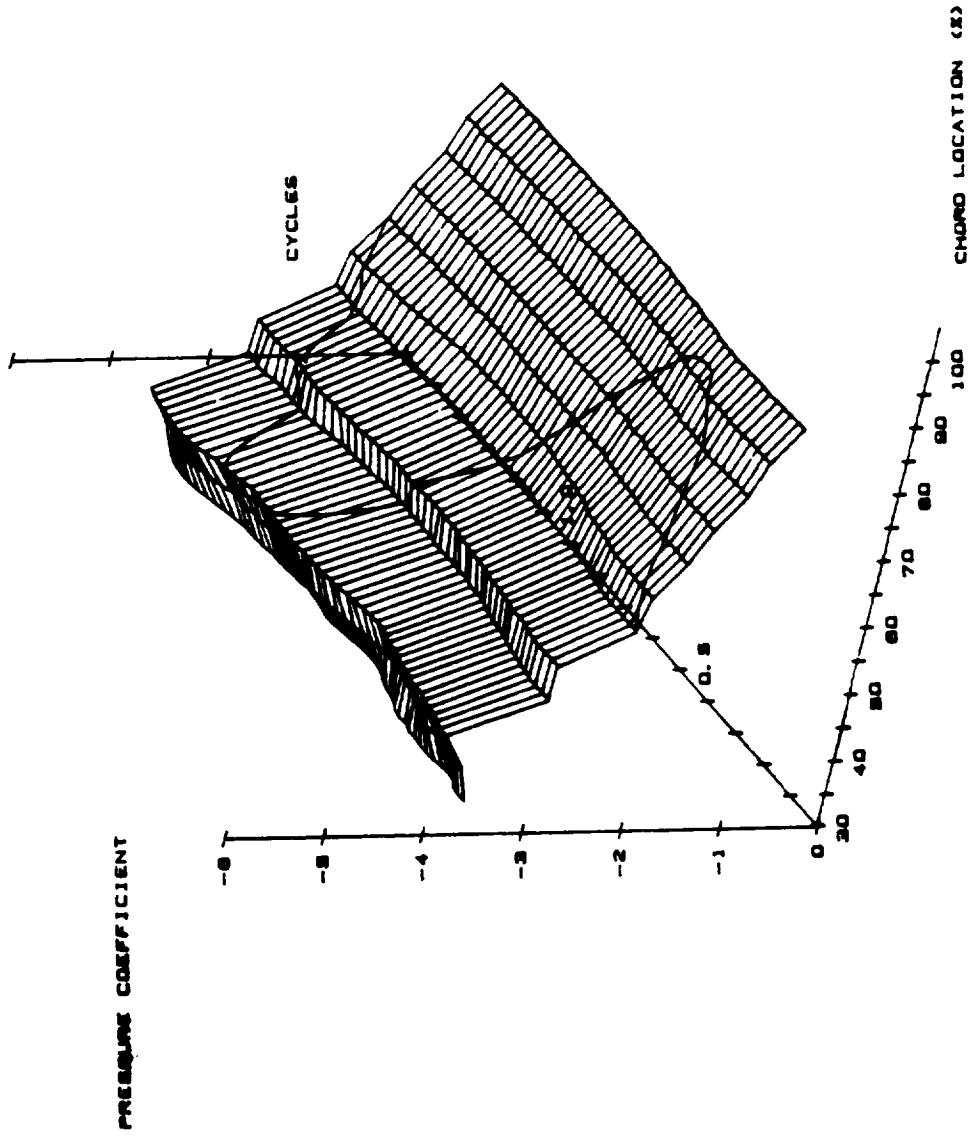


Figure 4.17 Unsteady Pressure Data : Pressure Coefficient as a function of Time and Chord Location. $Re = 500,000$, $U = 60$ ft/s, $k = 0.20$

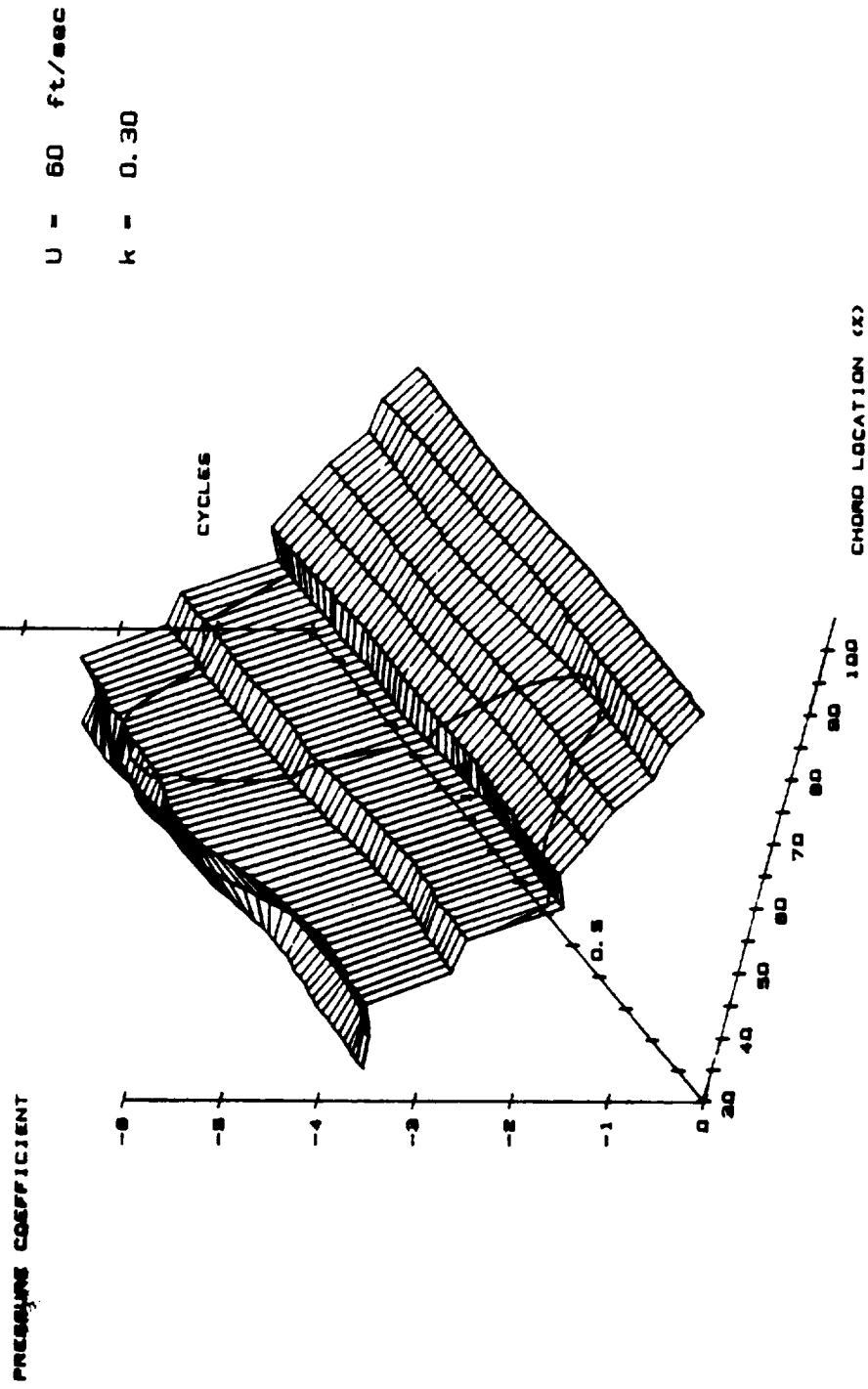


Figure 4.18 **Unsteady Pressure Data : Pressure Coefficient as a function of Time and Chord Location. $Re = 500,000$, $U = 60$ ft/s, $k = 0.30$**

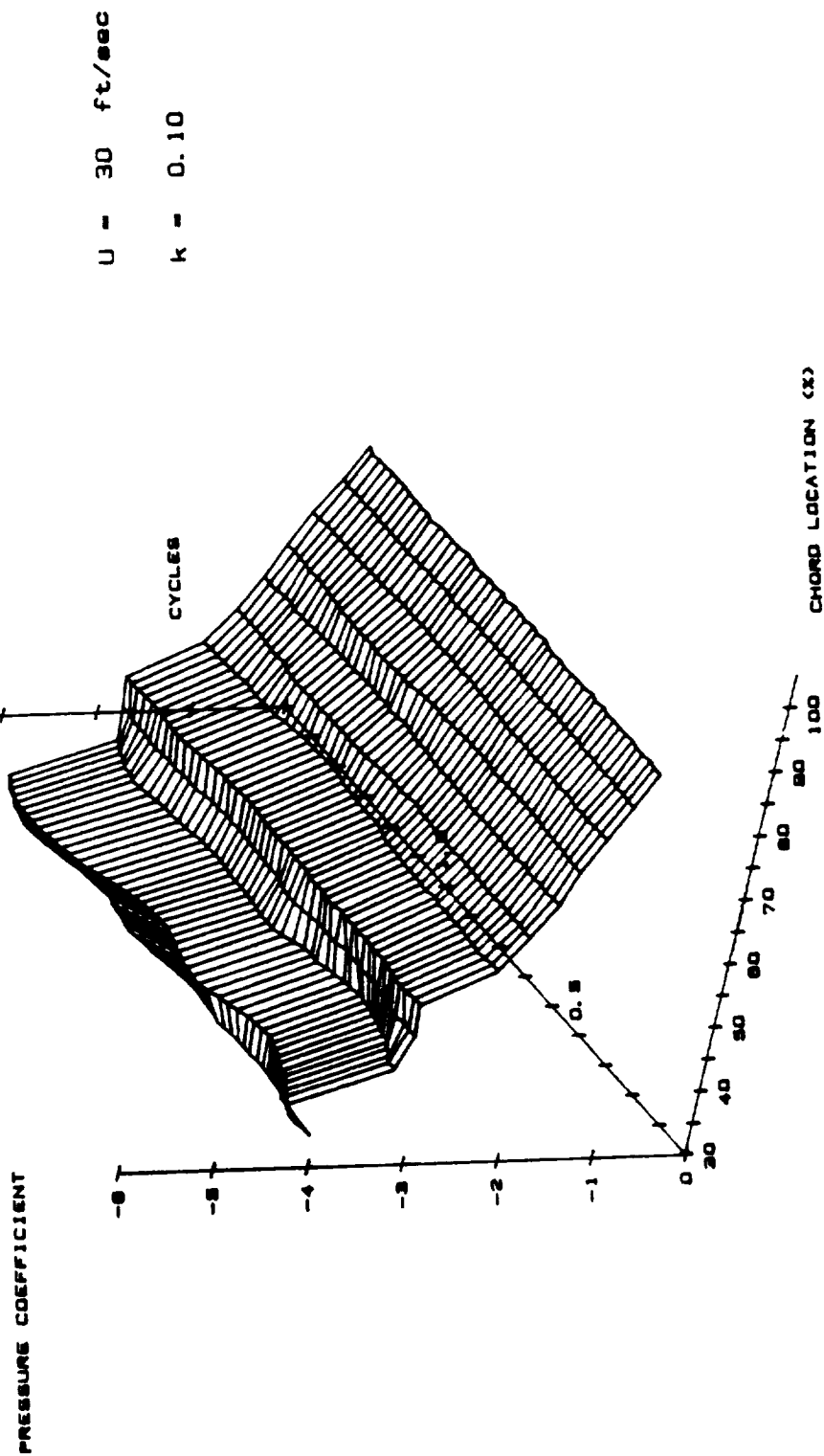


Figure 4.19 Unsteady Pressure Data from Right Side of Model: Pressure Coefficient as a function of Time and Chord Location. $Re = 250,000$, $U = 30$ ft/s, $k = 0.10$

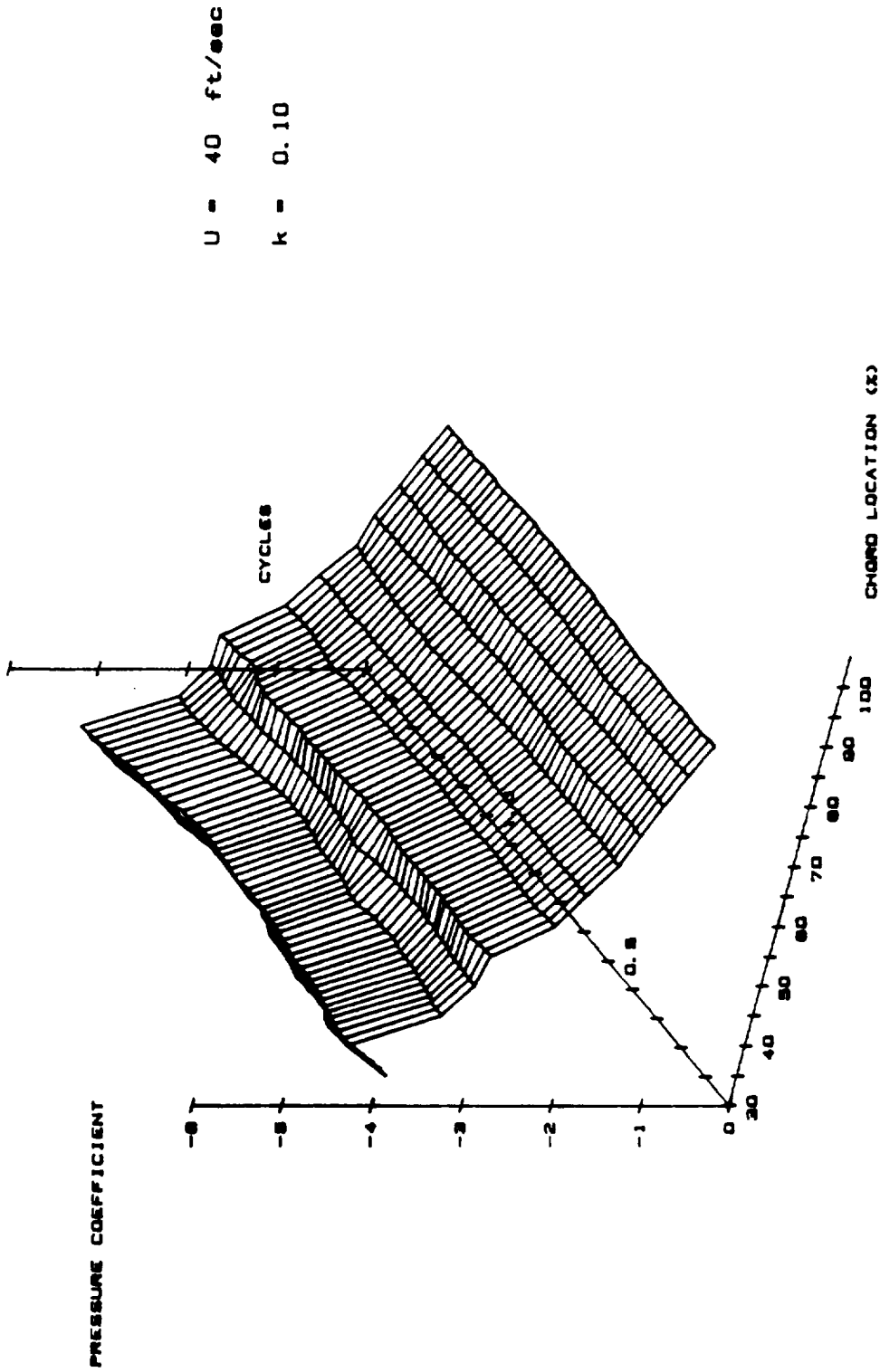


Figure 4.20 Unsteady Pressure Data from Right Side of Model: Pressure Coefficient as a function of Time and Chord Location. $Re = 335,000$, $U = 40$ ft/s, $k = 0.10$

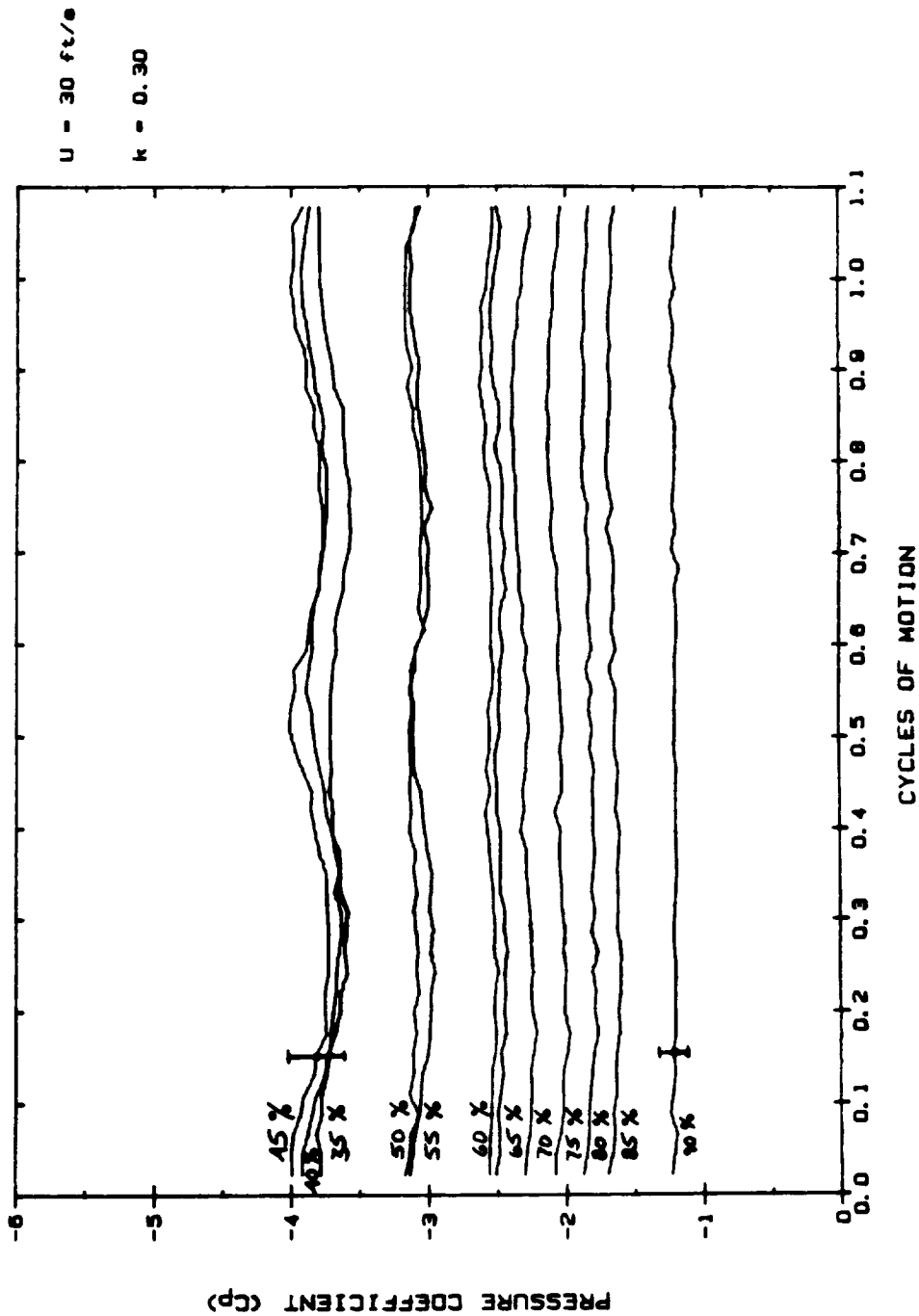


Figure 4.21 Unsteady Pressure Data : Pressure Coefficient as a function of Time. $Re = 250,000$, $U = 30$ ft/s, $k = 0.30$. Twelve Chord Locations Shown.

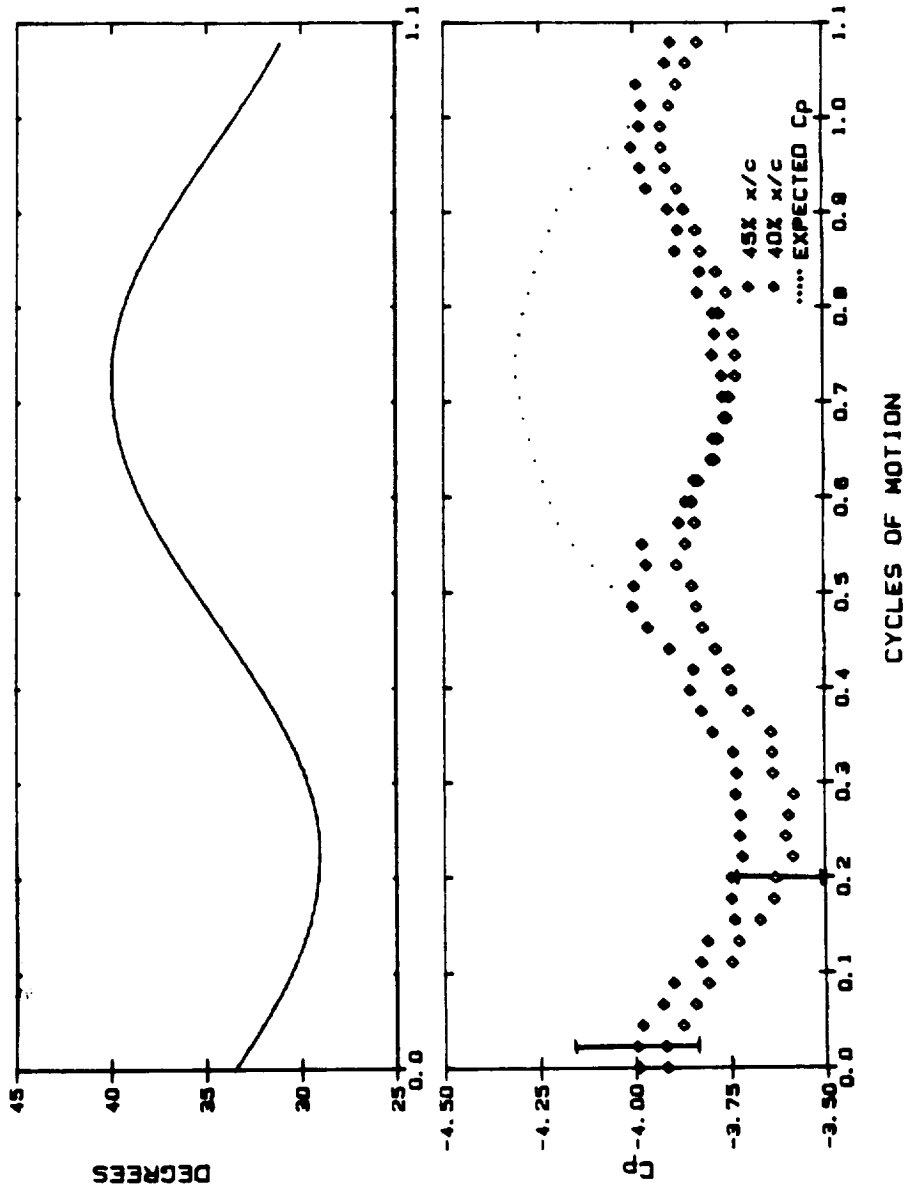


Figure 4.22 Unsteady Pressure Data : Pressure Coefficient as a function of Time. $Re = 250,000$, $U = 30$ ft/s, $k = 0.30$. Two Chord Locations Shown. (Expanded View of Figure 4.19).

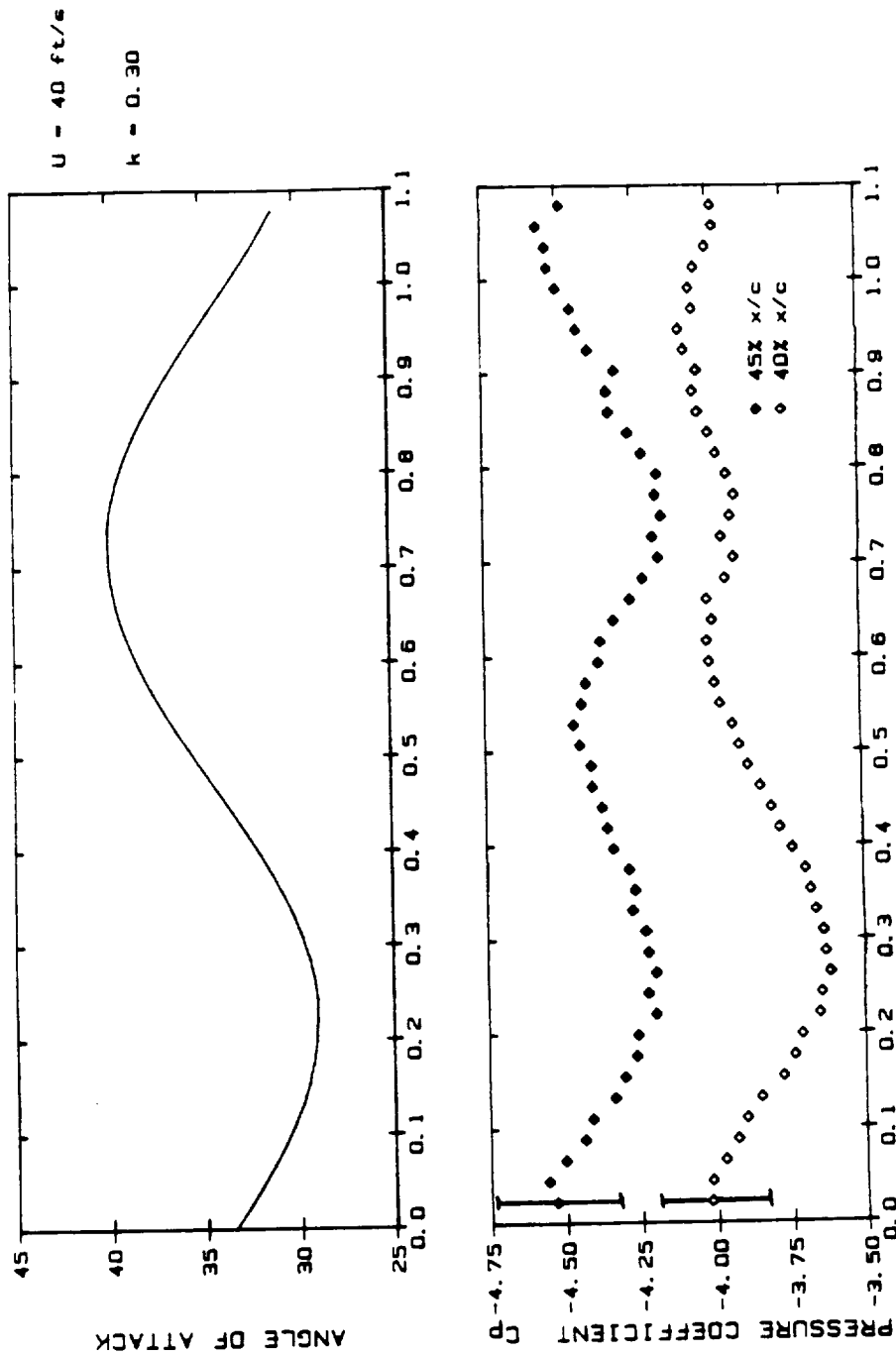


Figure 4.23 Unsteady Pressure Data : Pressure Coefficient as a function of Time. $Re = 335,000$, $U = 40$ ft/s, $k = 0.30$. Two Chord Locations Shown.

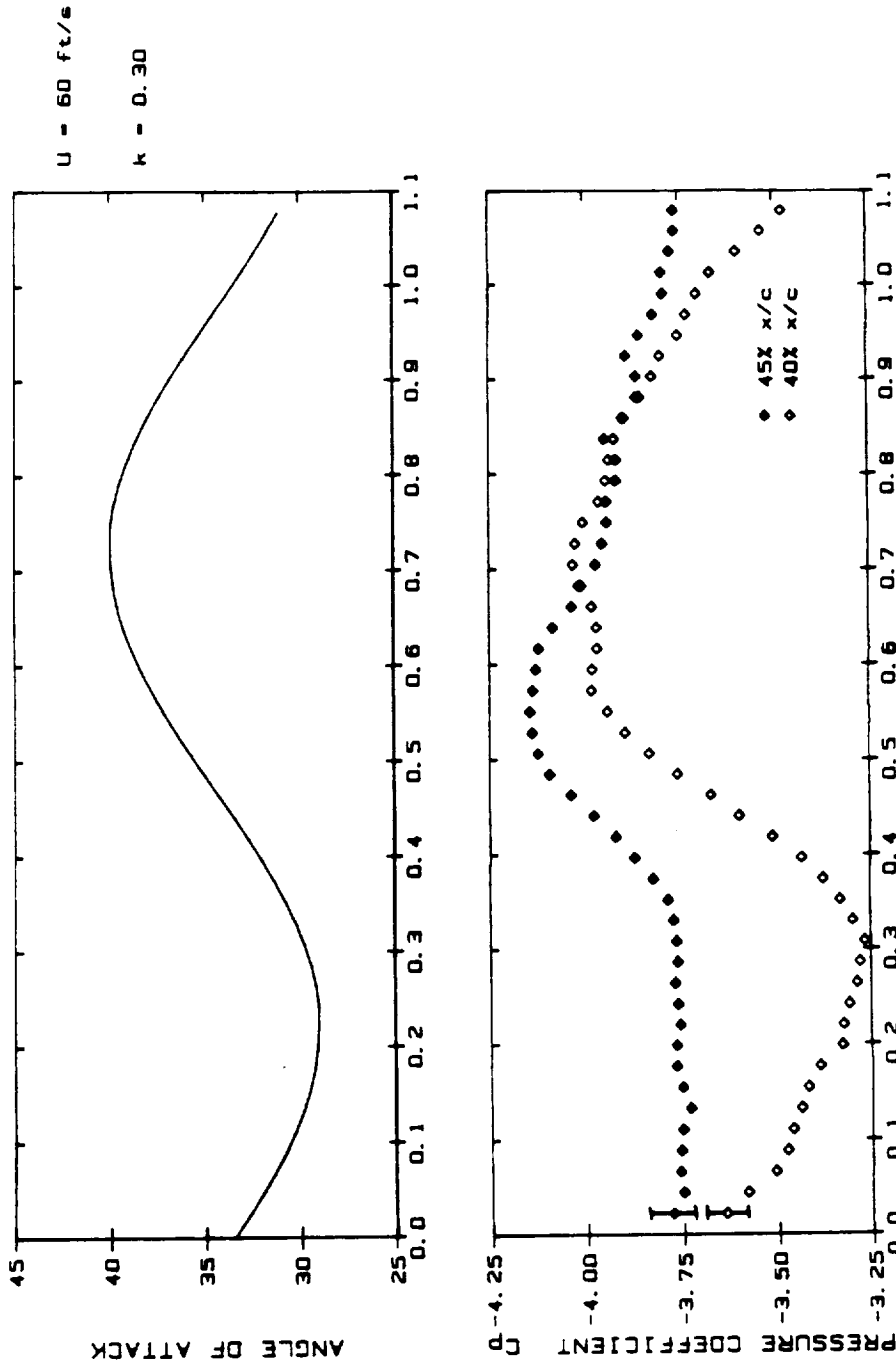


Figure 4.24 Unsteady Pressure Data : Pressure Coefficient as a function of Time. $Re = 500,000$, $U = 60$ ft/s, $k = 0.30$. Two Chord Locations Shown.

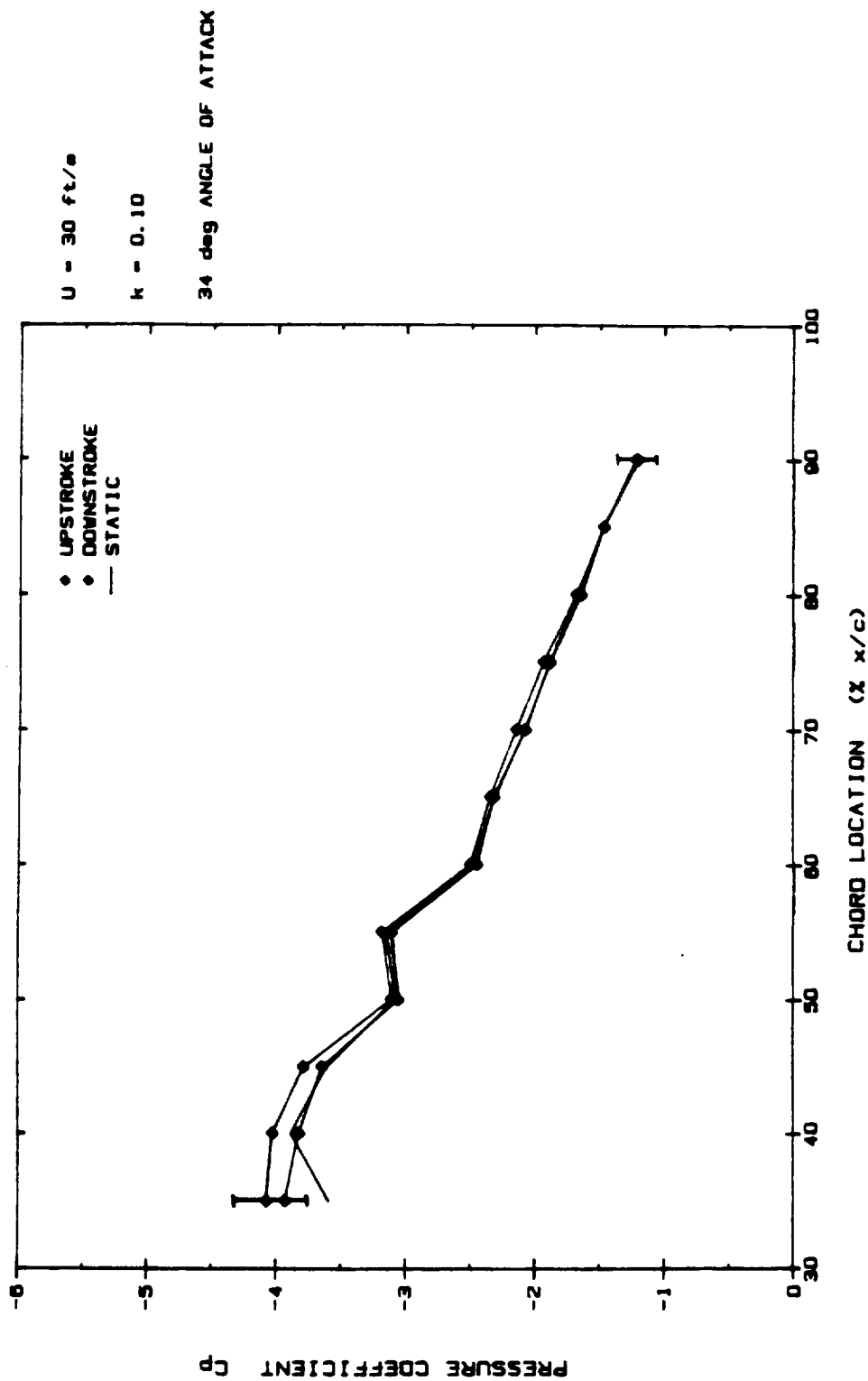


Figure 4.25 Instantaneous Pressure Distribution at 34° Angle of Attack: Upstroke, Downstroke, and Static. $Re = 250,000$, $U = 30$ ft/s, $k = 0.10$.

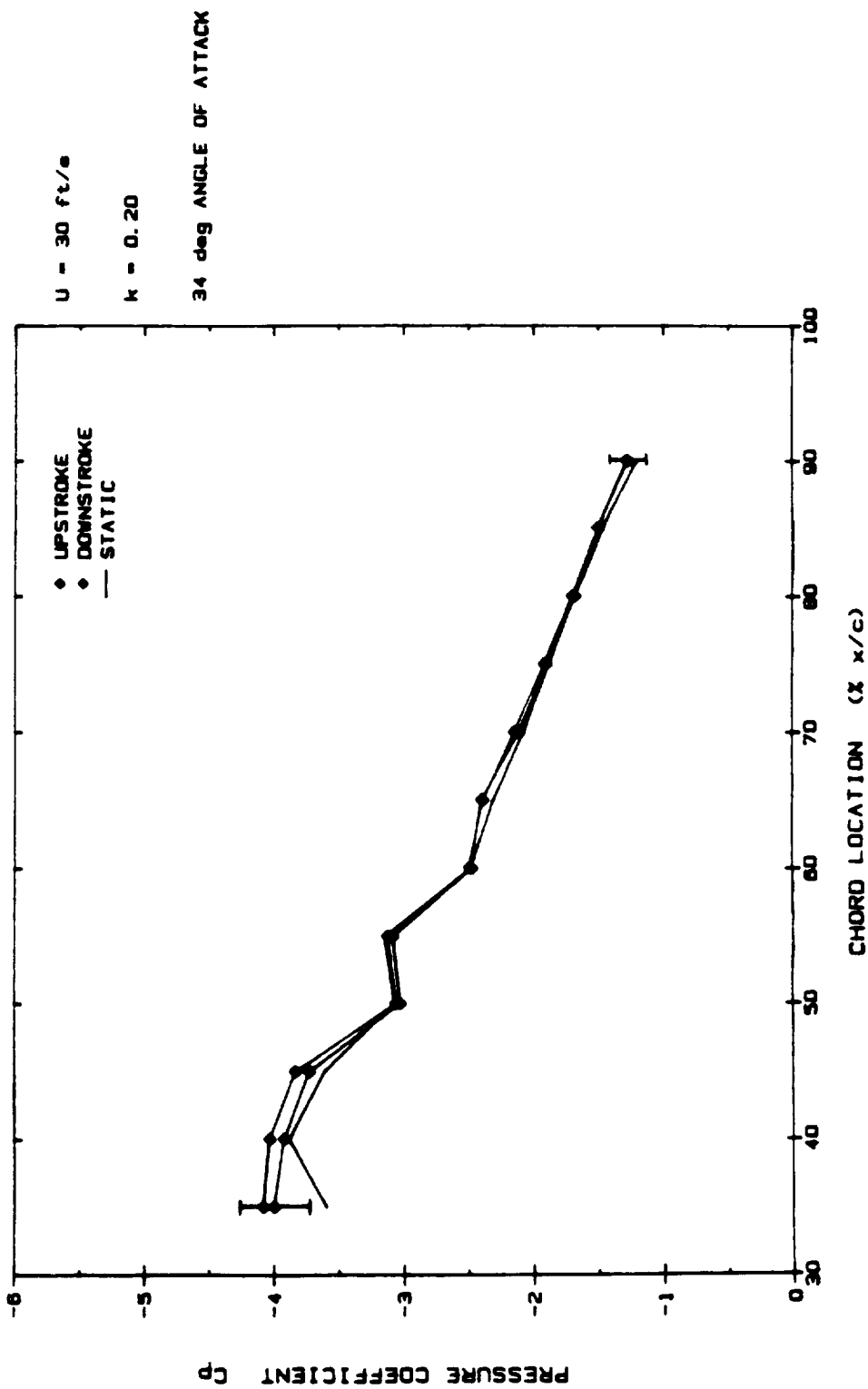


Figure 4.26 Instantaneous Pressure Distribution at 34° Angle of Attack : Upstroke, Downstroke, and Static. $Re = 250,000$, $U = 30 \text{ ft/s}$, $k = 0.20$.

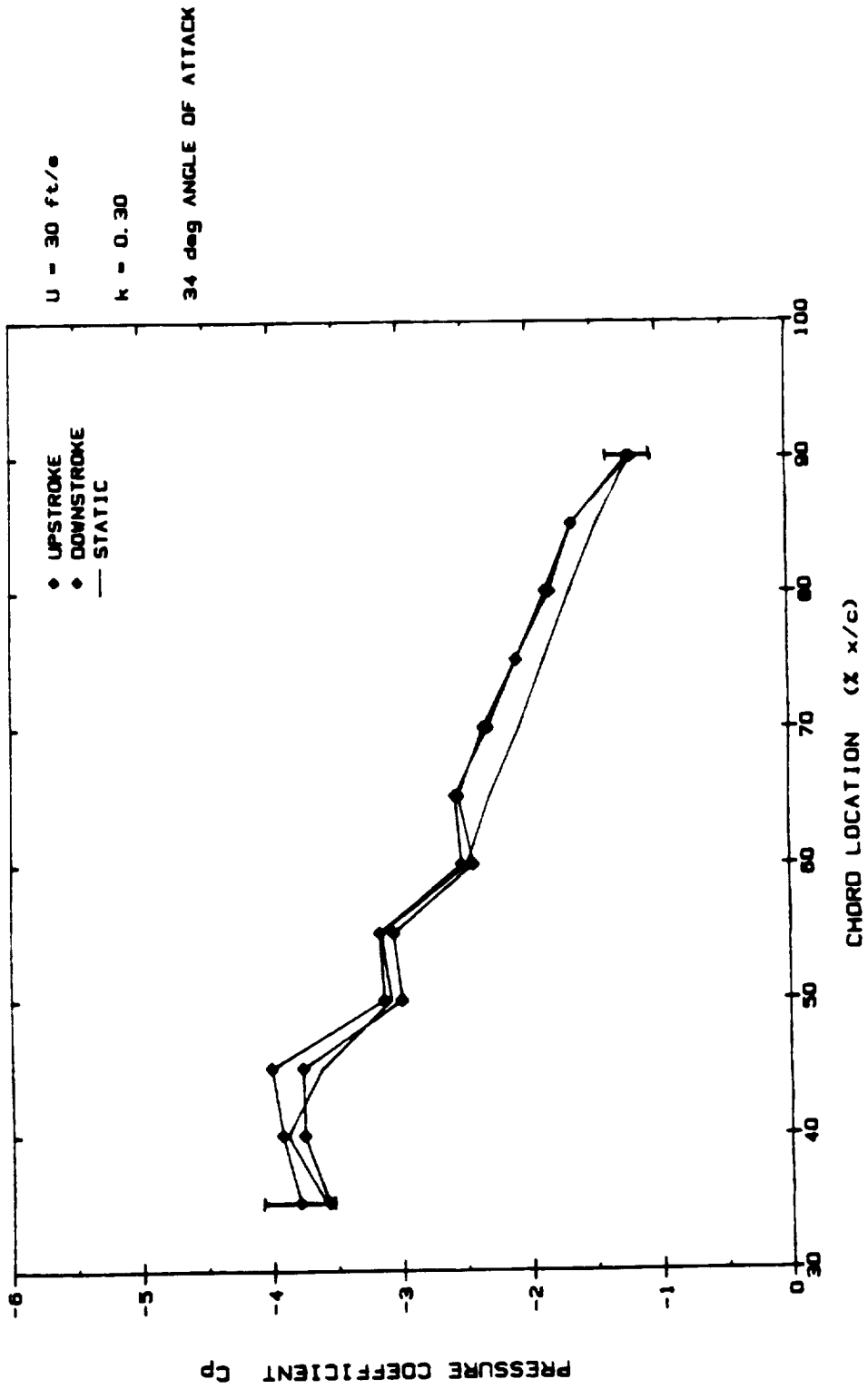


Figure 4.27 Instantaneous Pressure Distribution at 34° Angle of Attack : Upstroke, Downstroke, and Static. Re = 250,000, U = 30 ft/s, k = 0.30.

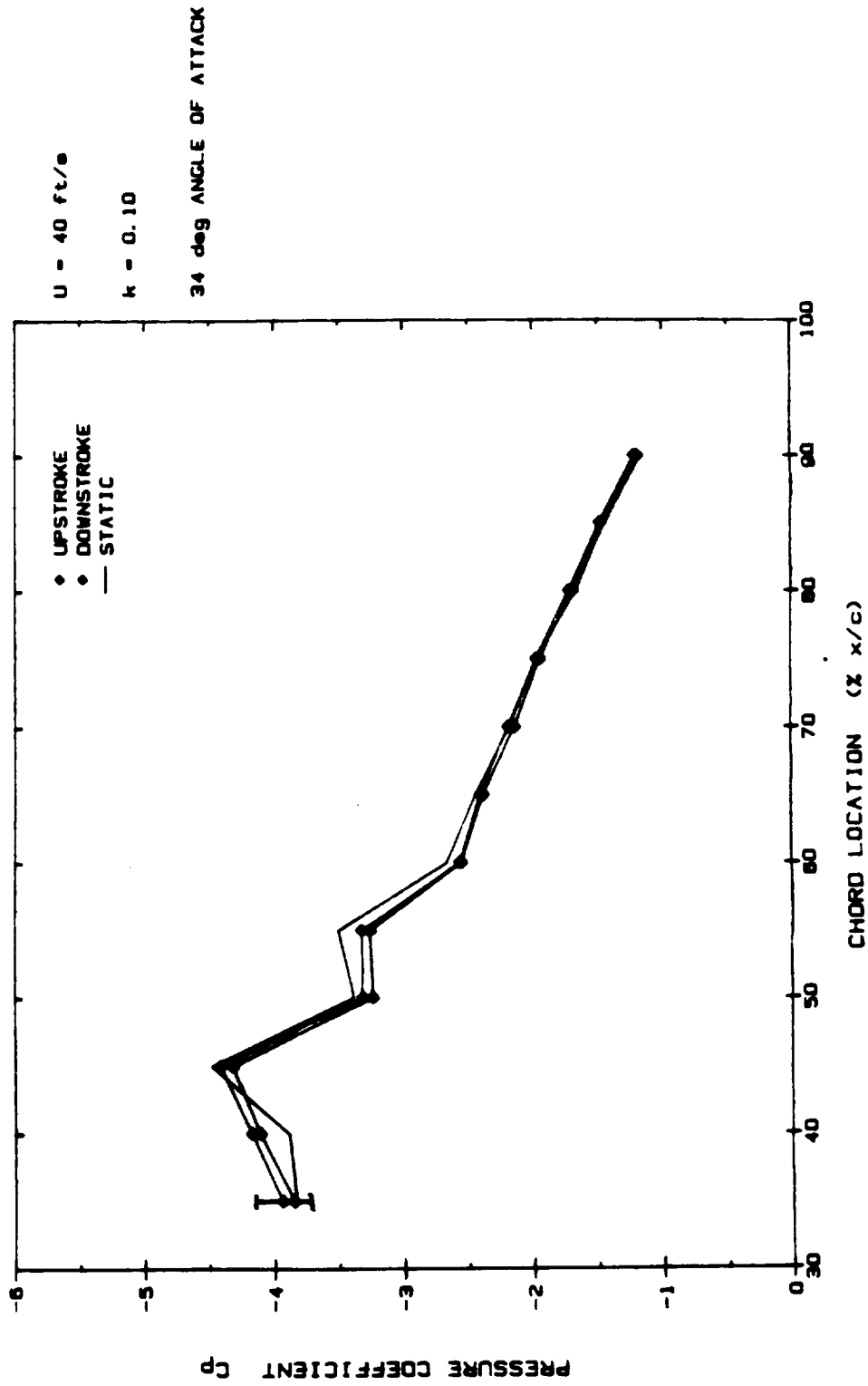


Figure 4.28 Instantaneous Pressure Distribution at 34° Angle of Attack : Upstroke, Downstroke, and Static. $Re = 335,000$, $U = 40$ ft/s, $k = 0.10$.

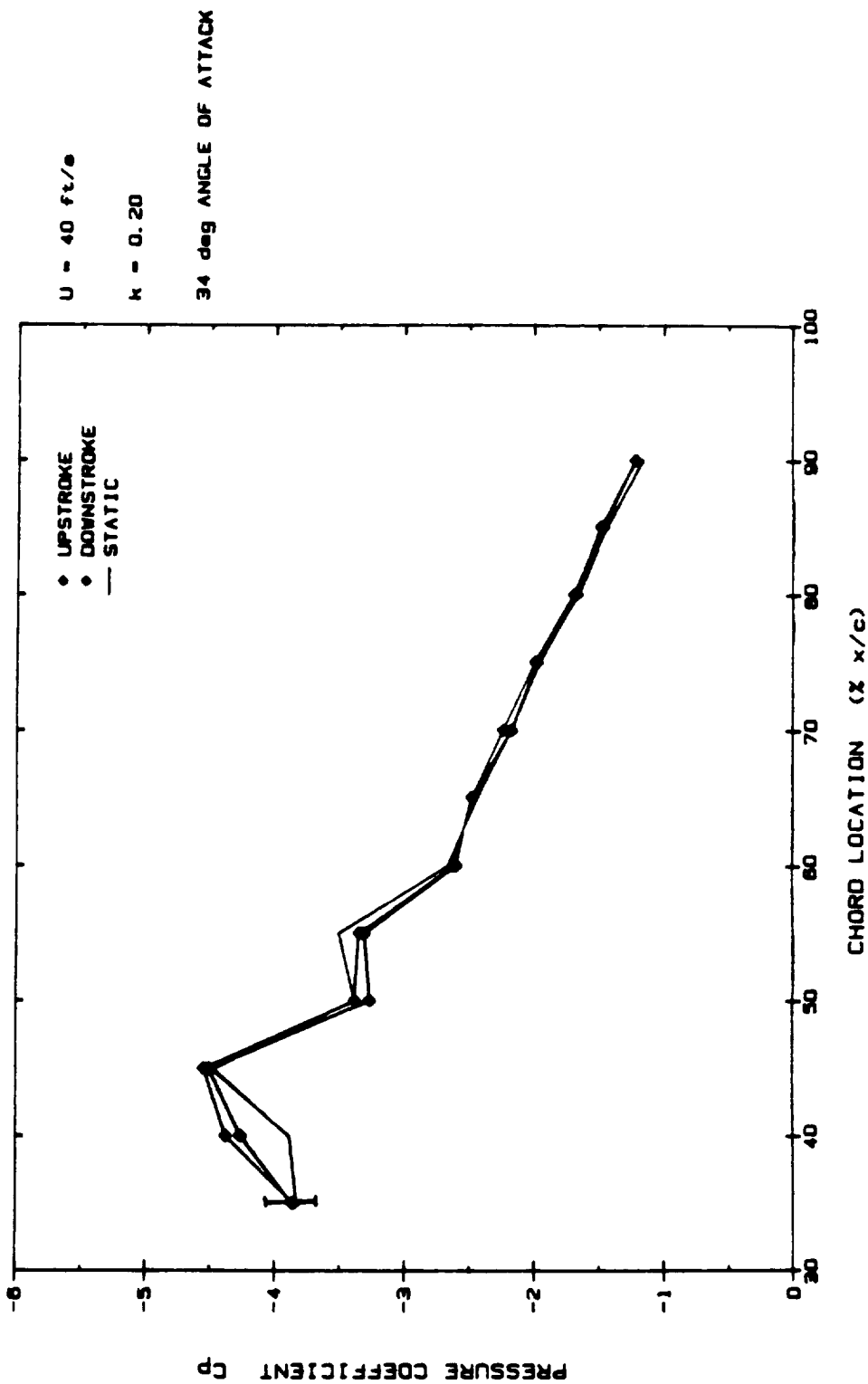


Figure 4.29 Instantaneous Pressure Distribution at 34° Angle of Attack : Upstroke, Downstroke, and Static. $Re = 335,000$, $U = 40 \text{ ft/s}$, $k = 0.20$.

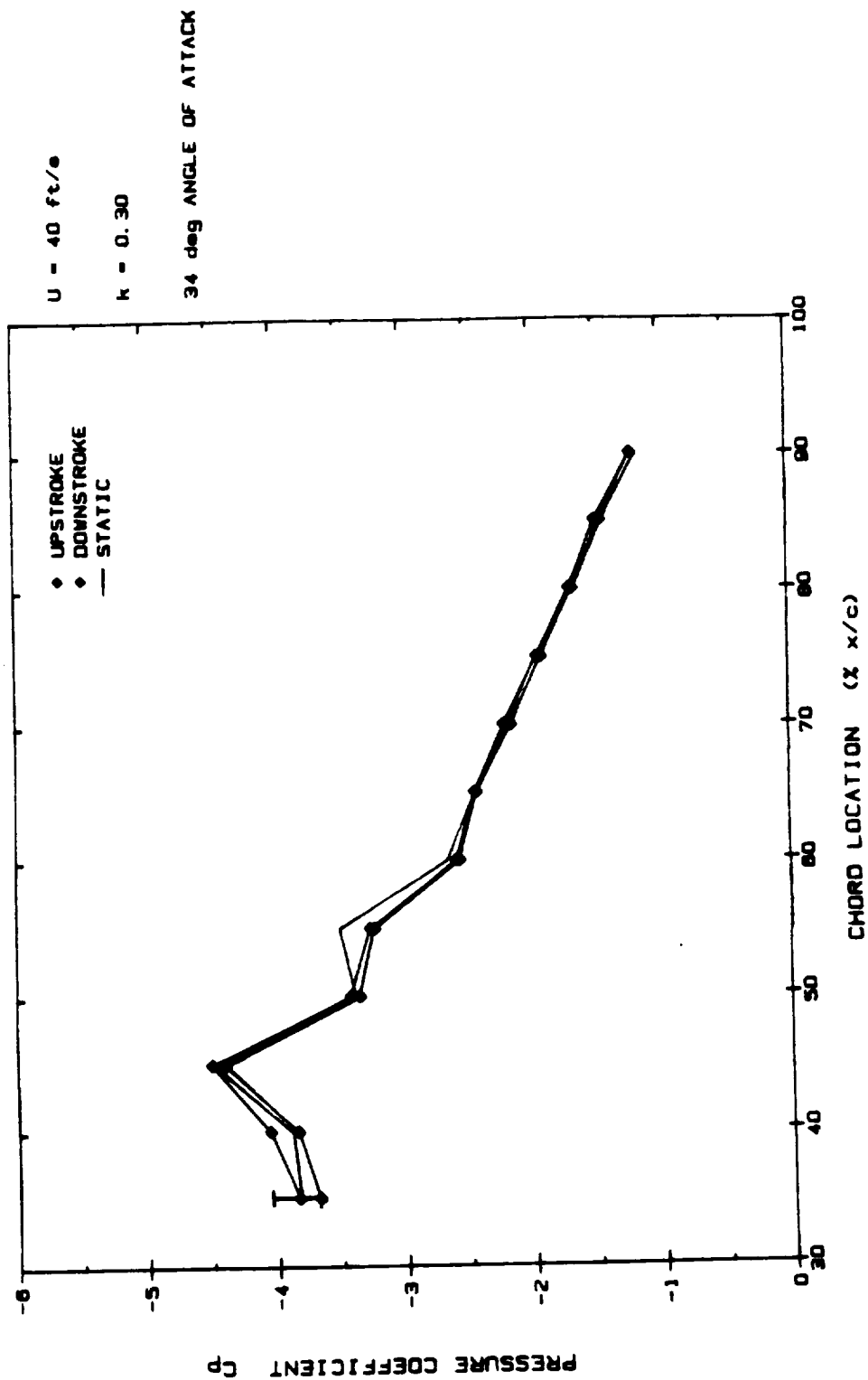


Figure 4.30 Instantaneous Pressure Distribution at 34° Angle of Attack : Upstroke, Downstroke, and Static. $Re = 335,000$, $U = 40 \text{ ft/s}$, $k = 0.30$.

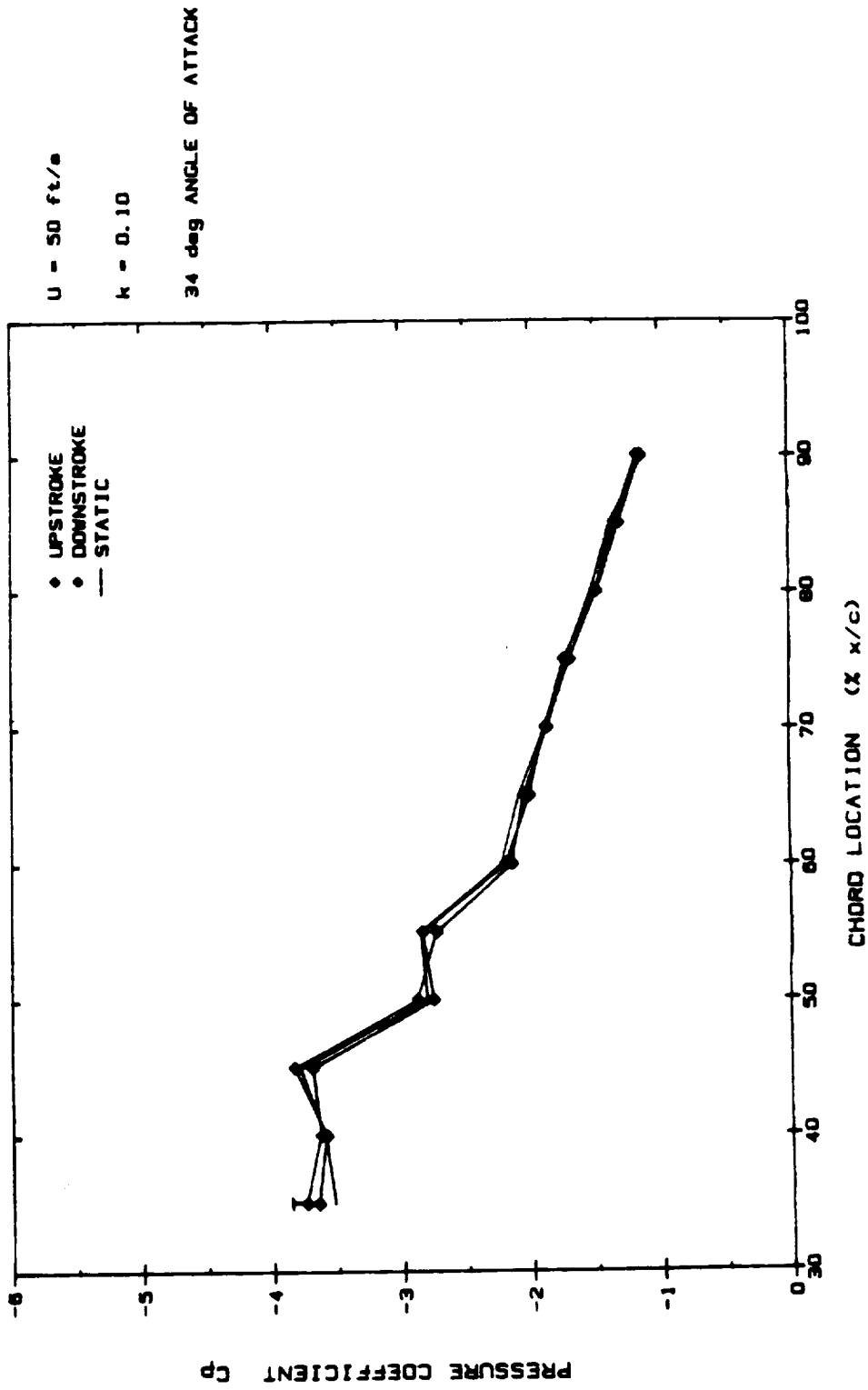


Figure 4.31 Instantaneous Pressure Distribution at 34° Angle of Attack : Upstroke, Downstroke, and Static. Re = 420,000, U = 50 ft/s, k = 0.10.

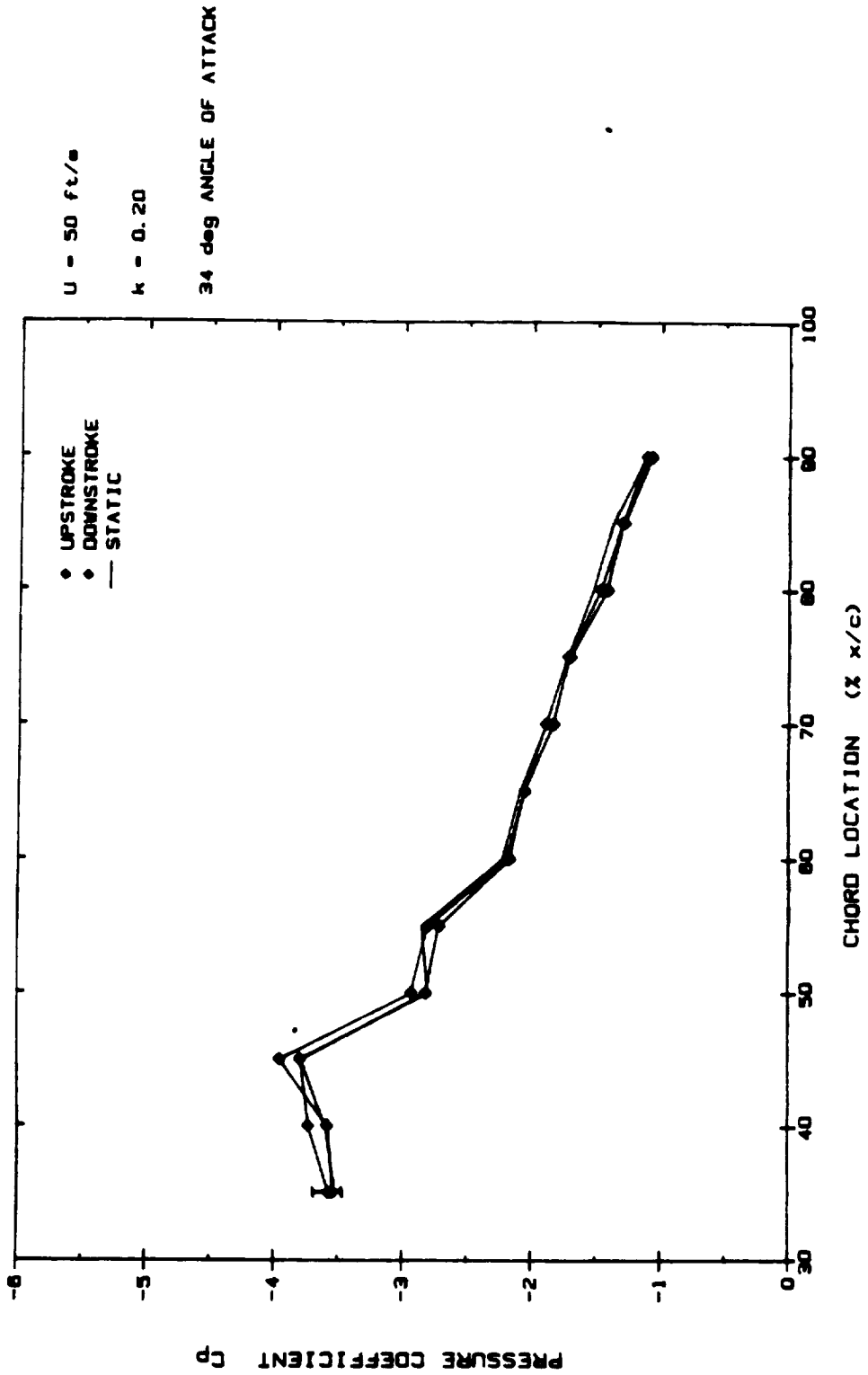


Figure 4.32 Instantaneous Pressure Distribution at 34° Angle of Attack : Upstroke, Downstroke, and Static. Re = 420,000, U = 50 ft/s, k = 0.20.

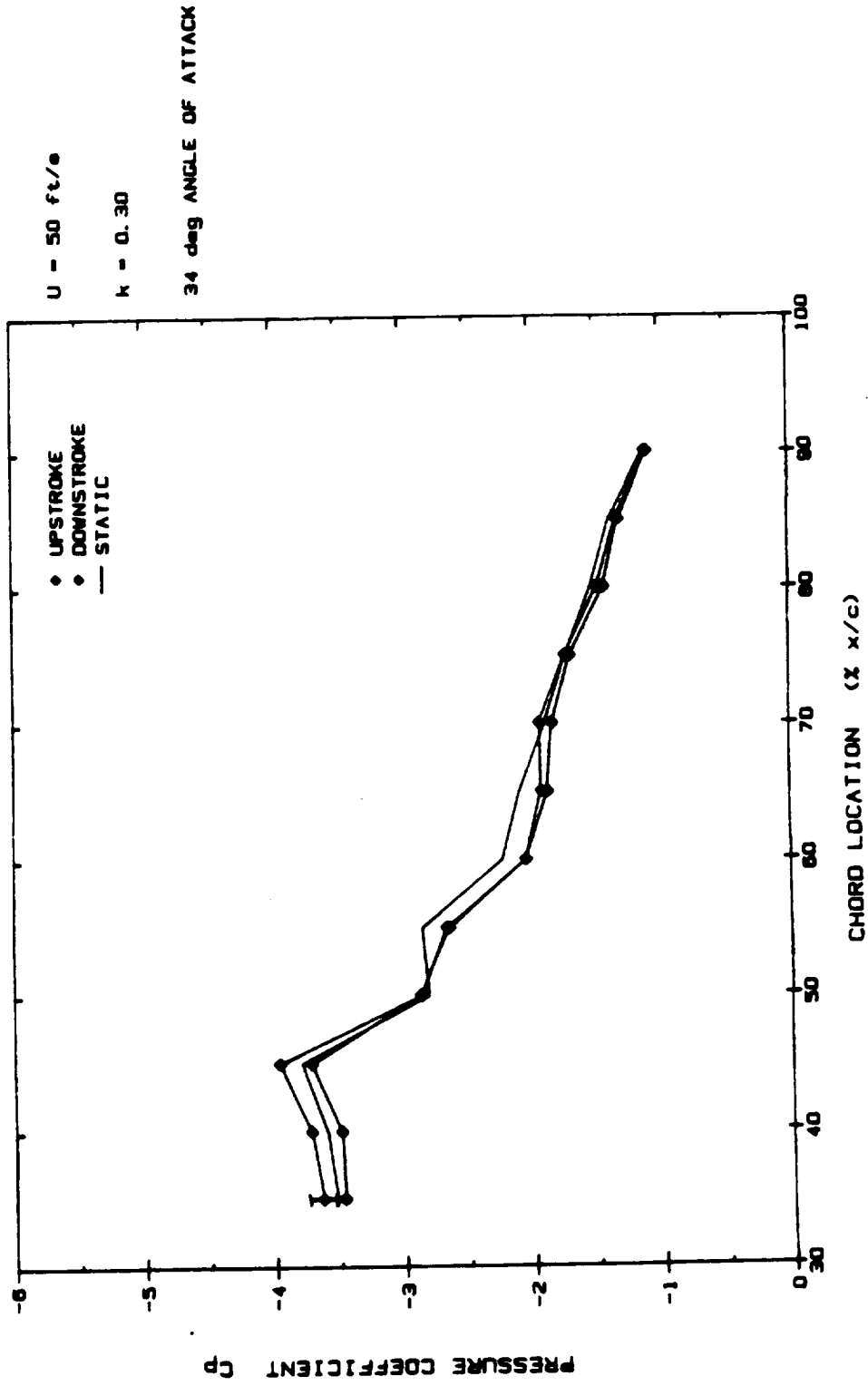


Figure 4.33 Instantaneous Pressure Distribution at 34° Angle of Attack : Upstroke, Downstroke, and Static. Re = 420,000, U = 50 ft/s, k = 0.30.

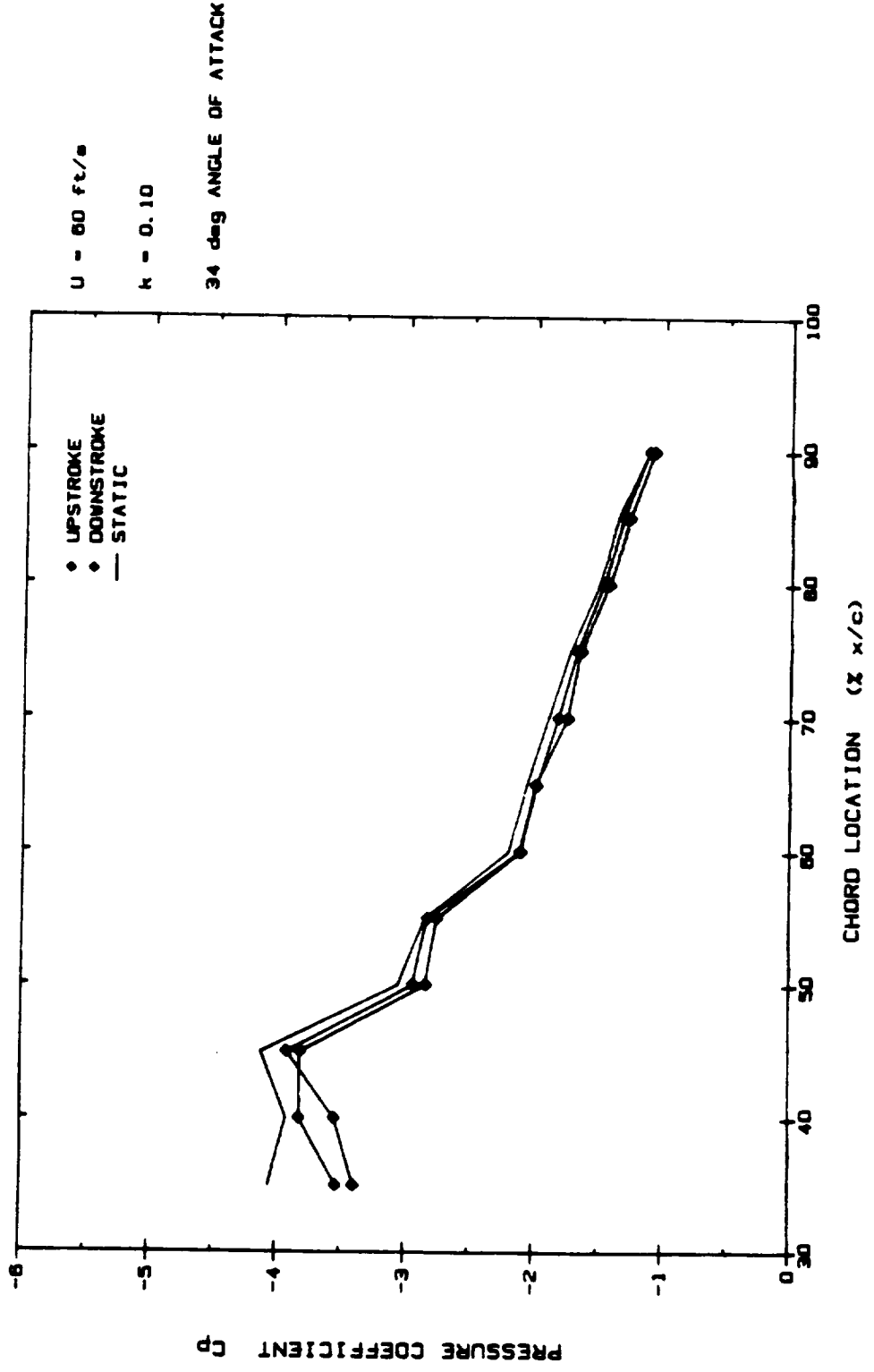


Figure 4.34 Instantaneous Pressure Distribution at 34° Angle of Attack: Upstroke, Downstroke, and Static. $Re = 500,000$, $U = 60$ ft/s, $k = 0.10$.

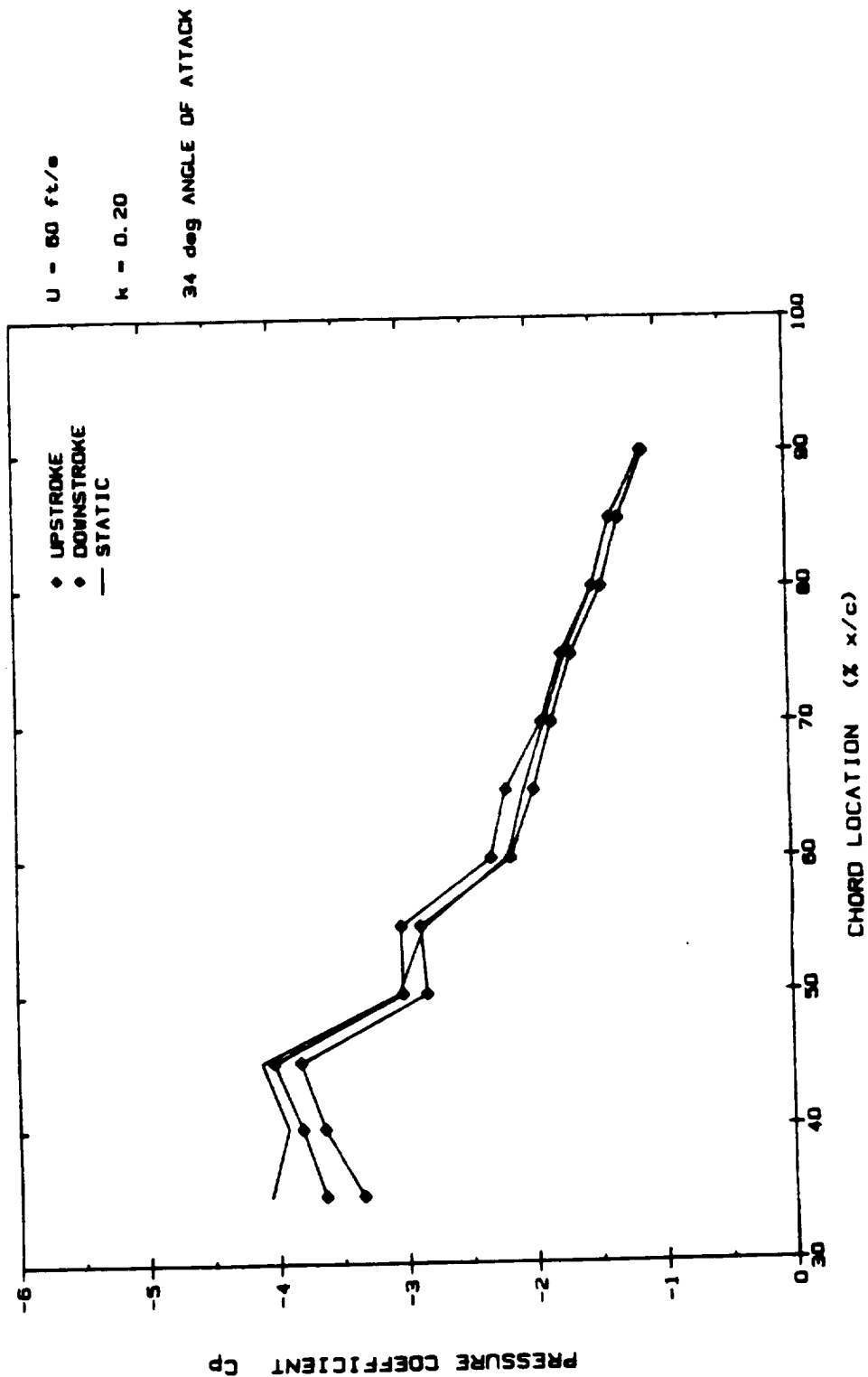


Figure 4.35 Instantaneous Pressure Distribution at 34° Angle of Attack : Upstroke, Downstroke, and Static. $Re = 500,000$, $U = 60 \text{ ft/s}$, $k = 0.20$.

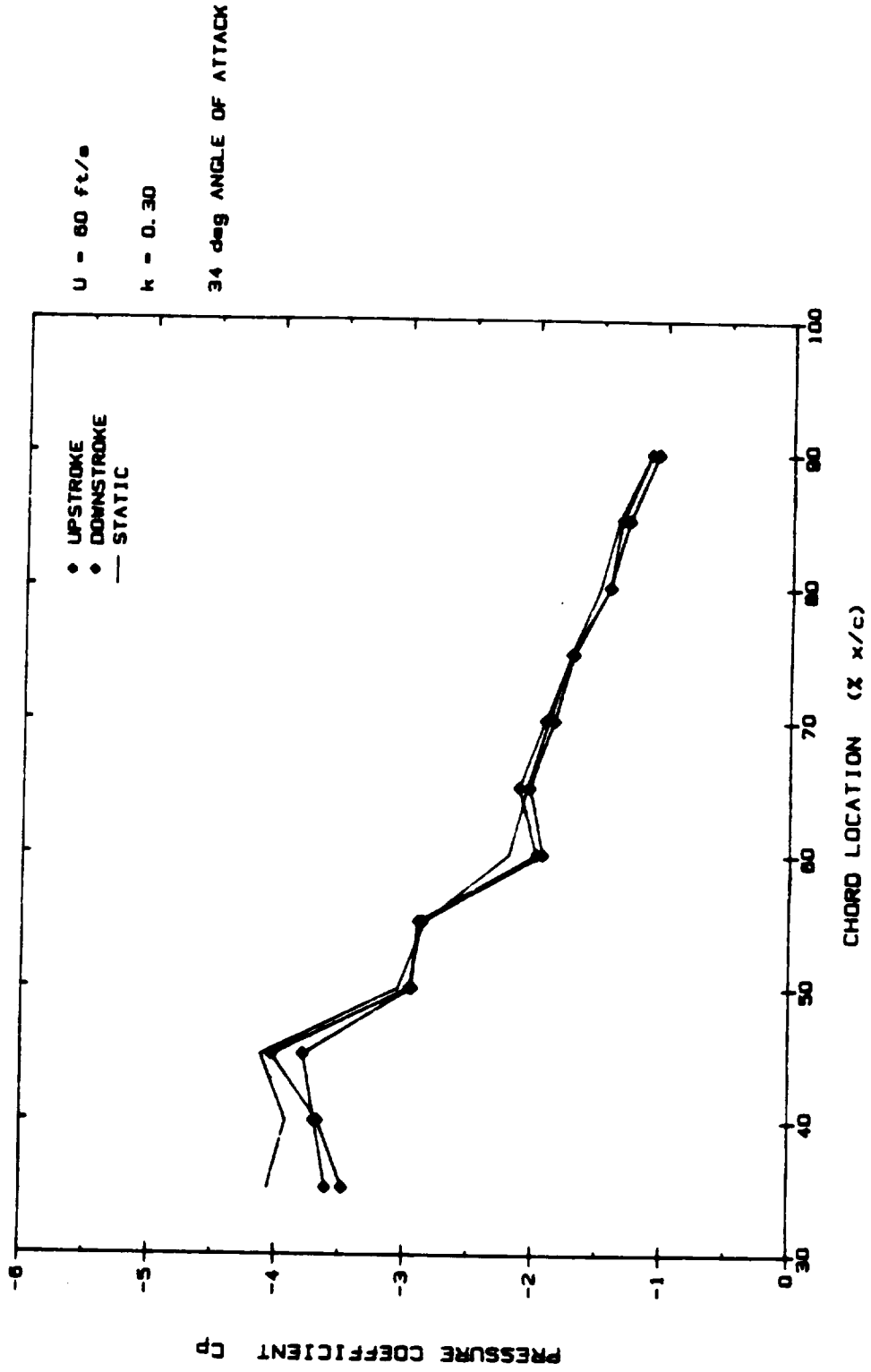


Figure 4.36 Instantaneous Pressure Distribution at 34° Angle of Attack : Upstroke, Downstroke, and Static. Re = 500,000, U = 60 ft/s, k = 0.30

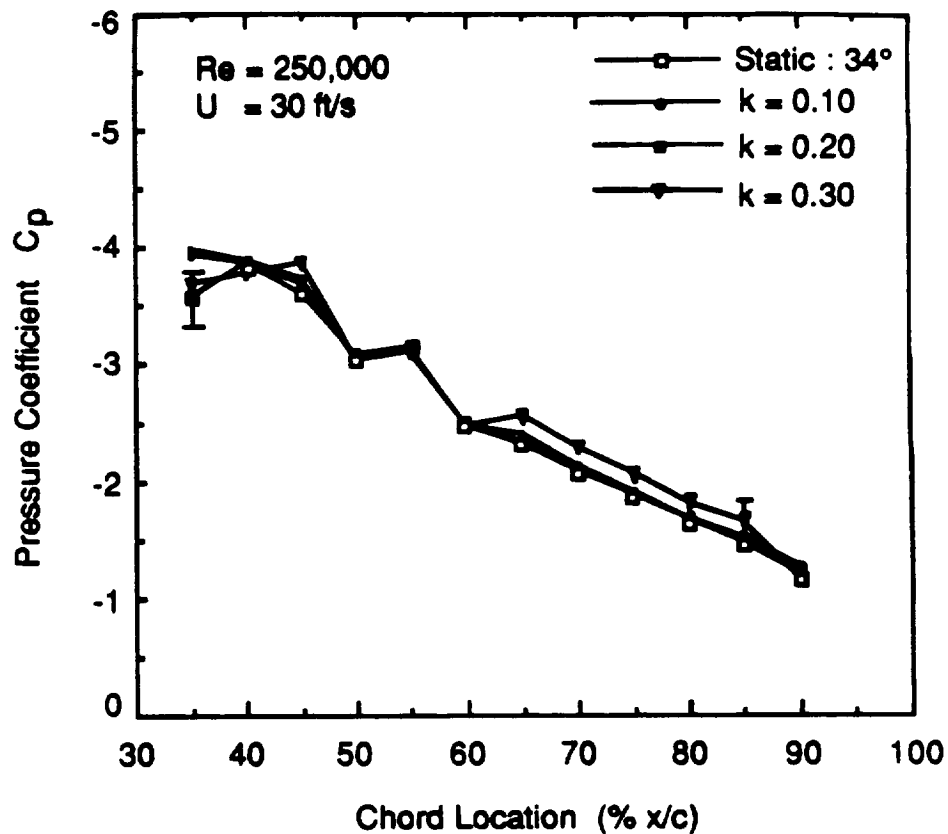


Figure 4.37

Unsteady Pressure Data : Average Pressure Coefficient as a Function of Chord Location. Re = 250,000 , U = 30 ft/s , k = 0.10,0.20,0.30. Static Curve at 34° also Shown.

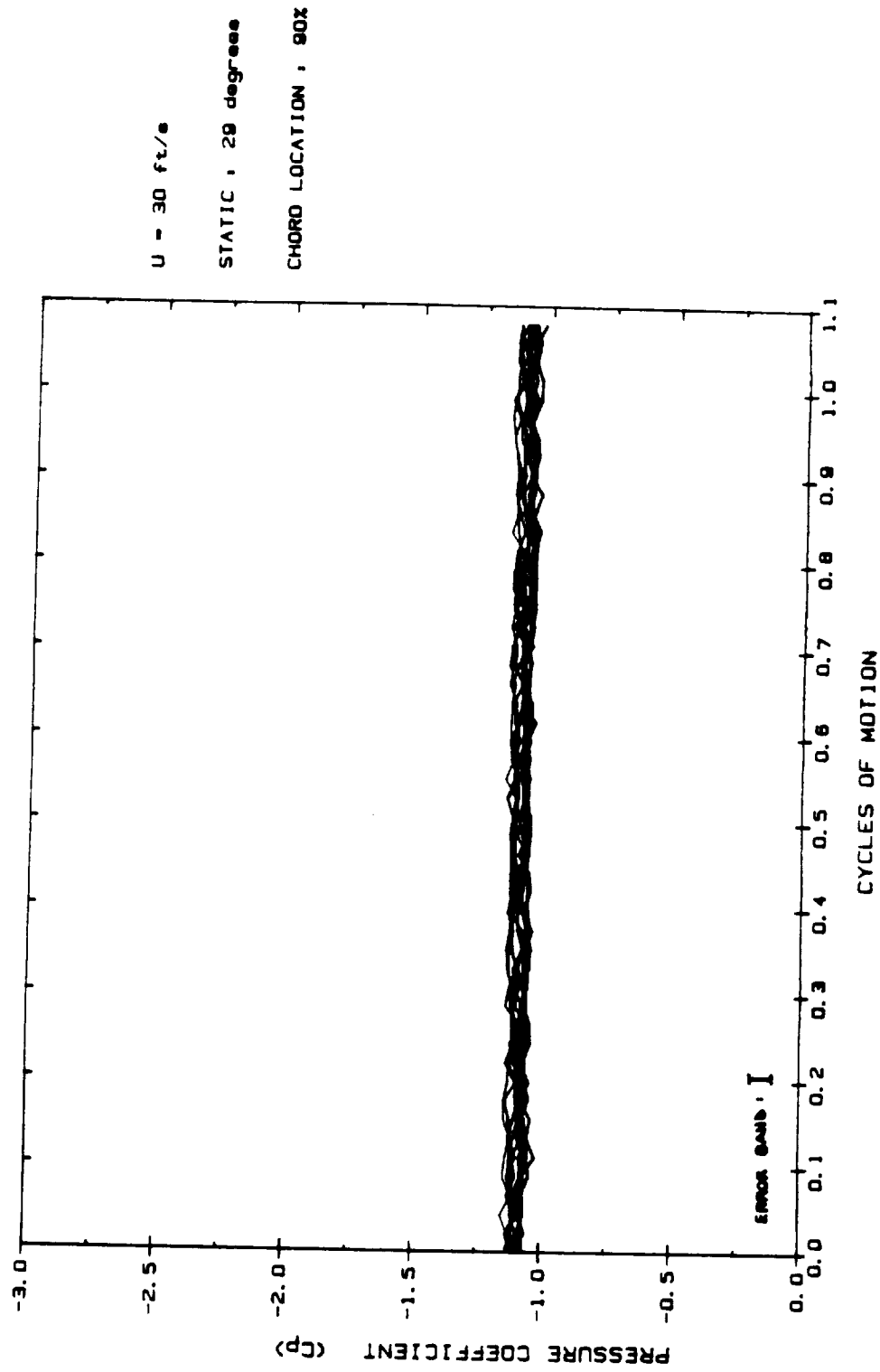


Figure 4.38 Unsteady Pressure Data : Pressure Coefficient Recorded at the Right Side, 90% Chord Location During each of Twelve Tests Performed on the Left Side. $Re = 250,000$, $U = 30$ ft/s, $k = 0.10$. Corresponds to Left Side Pressures Shown in Figure 4.7.

APPENDIX A

UNCERTAINTY OF PRESSURE COEFFICIENTS

TABLE A1

**UNCERTAINTIES IN THE PRESSURE COEFFICIENT : STATIC AND
DYNAMIC TESTS**

STATIC TESTS :

FREESTREAM VELOCITY	ANGLE OF ATTACK	RANGE OF UNCERTAINTY :	
		C_p	%
30 ft/s	29°	0.12-0.24	6.7-10.9
	34°	0.12-0.24	6.7-10.3
	39°	0.13-0.26	6.5-9.7
40 ft/s	29°	0.07-0.14	3.8-6.4
	34°	0.07-0.16	3.6-5.9
	39°	0.07-0.17	3.6-5.5
50 ft/s	29°	0.04-0.09	2.4-4.0
	34°	0.04-0.09	2.4-3.9
	39°	0.04-0.08	2.5-3.9
60 ft/s	29°	0.03-0.06	1.7-2.9
	34°	0.03-0.07	1.6-2.7
	39°	0.03-0.06	1.7-2.7

UNSTEADY TESTS :

FREESTREAM VELOCITY	REDUCED FREQUENCY	RANGE OF UNCERTAINTY :	
		C_p	%
30 ft/s	0.10	0.12-0.26	6.6-10.2
	0.20	0.13-0.26	6.5-10.0
	0.30	0.12-0.25	6.6-10.5
40 ft/s	0.10	0.07-0.16	3.6-5.9
	0.20	0.07-0.16	3.6-5.8
	0.30	0.07-0.16	3.6-5.8
50 ft/s	0.10	0.04-0.09	2.4-3.9
	0.20	0.04-0.09	2.4-3.9
	0.30	0.04-0.09	2.4-3.9
60 ft/s	0.10	0.03-0.06	1.6-2.7
	0.20	0.03-0.06	1.6-2.7
	0.30	0.03-0.06	1.6-2.7

APPENDIX B

TABULAR STATIC DATA

TABLE B1
TABULAR STATIC DATA

		U = 30 ft/s			U = 40 ft/s		
<u>Incidence:</u>		29°	34°	39°	29°	34°	39°
<u>% Chord</u>	<u>Cp:</u>						
35	-3.107	-3.592	-3.915	-3.112	-3.828	-4.049	
40	-3.165	-3.880	-3.865	-3.060	-3.885	-4.480	
45	-3.627	-3.610	-4.025	-3.720	-4.481	-4.669	
50	-2.774	-3.075	-3.199	-2.861	-3.382	-3.514	
55	-2.722	-3.152	-3.333	-2.815	-3.503	-3.388	
60	-2.164	-2.483	-2.762	-2.220	-2.661	-2.783	
65	-2.106	-2.304	-2.595	-2.133	-2.438	-2.638	
70	-1.857	-2.073	-2.339	-1.875	-2.174	-2.373	
75	-1.657	-1.878	-2.096	-1.687	-1.958	-2.130	
80	-1.475	-1.677	-1.844	-1.455	-1.661	-1.870	
85	-1.314	-1.468	-1.640	-1.286	-1.439	-1.642	
90	-1.084	-1.199	-1.344	-1.063	-1.159	-1.327	

		U = 50 ft/s			U = 60 ft/s		
<u>Incidence:</u>		29°	34°	39°	29°	34°	39°
<u>% Chord</u>	<u>Cp:</u>						
35	-3.390	-3.524	-3.077	-3.323	-4.056	-3.283	
40	-3.268	-3.598	-3.051	-3.216	-3.918	-3.272	
45	-3.903	-3.787	-2.867	-3.840	-4.118	-3.074	
50	-2.974	-2.804	-2.248	-2.868	-3.050	-2.377	
55	-2.792	-2.856	-2.226	-2.863	-2.846	-2.319	
60	-1.994	-2.224	-1.780	-2.120	-2.193	-1.839	
65	-1.874	-2.087	-1.684	-1.937	-2.055	-1.726	
70	-1.815	-1.886	-1.554	-1.742	-1.891	-1.565	
75	-1.704	-1.724	-1.456	-1.621	-1.724	-1.469	
80	-1.465	-1.524	-1.326	-0.991	-1.503	-1.341	
85	-1.314	-1.378	-1.249	-1.220	-1.367	-1.271	
90	-1.072	-1.114	-1.120	-0.984	-1.116	-1.143	

APPENDIX C
WIRING SCHEMATICS

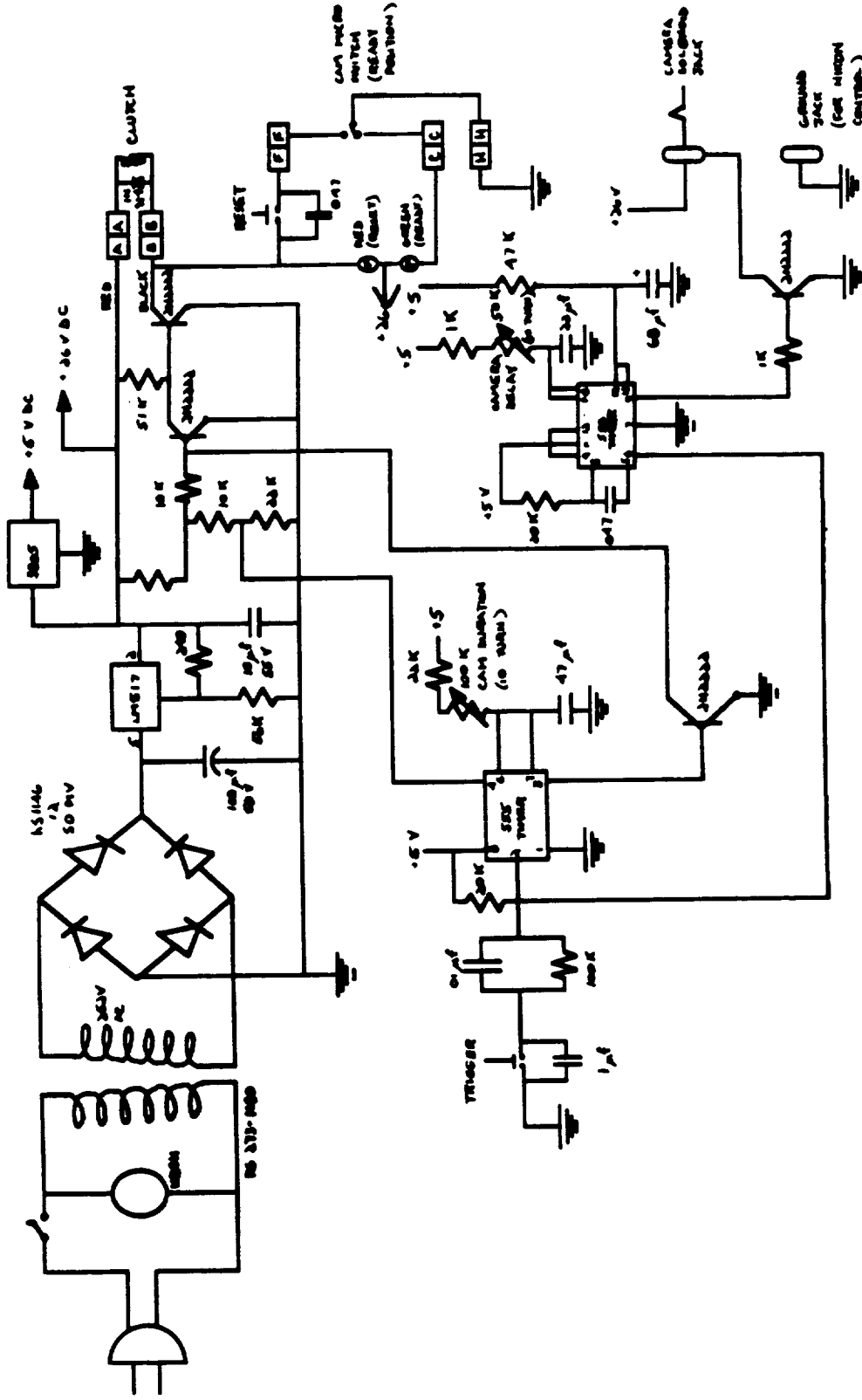


Figure C1
Wiring Schematic for Unsteady Pitching
Mechanism Control Box.

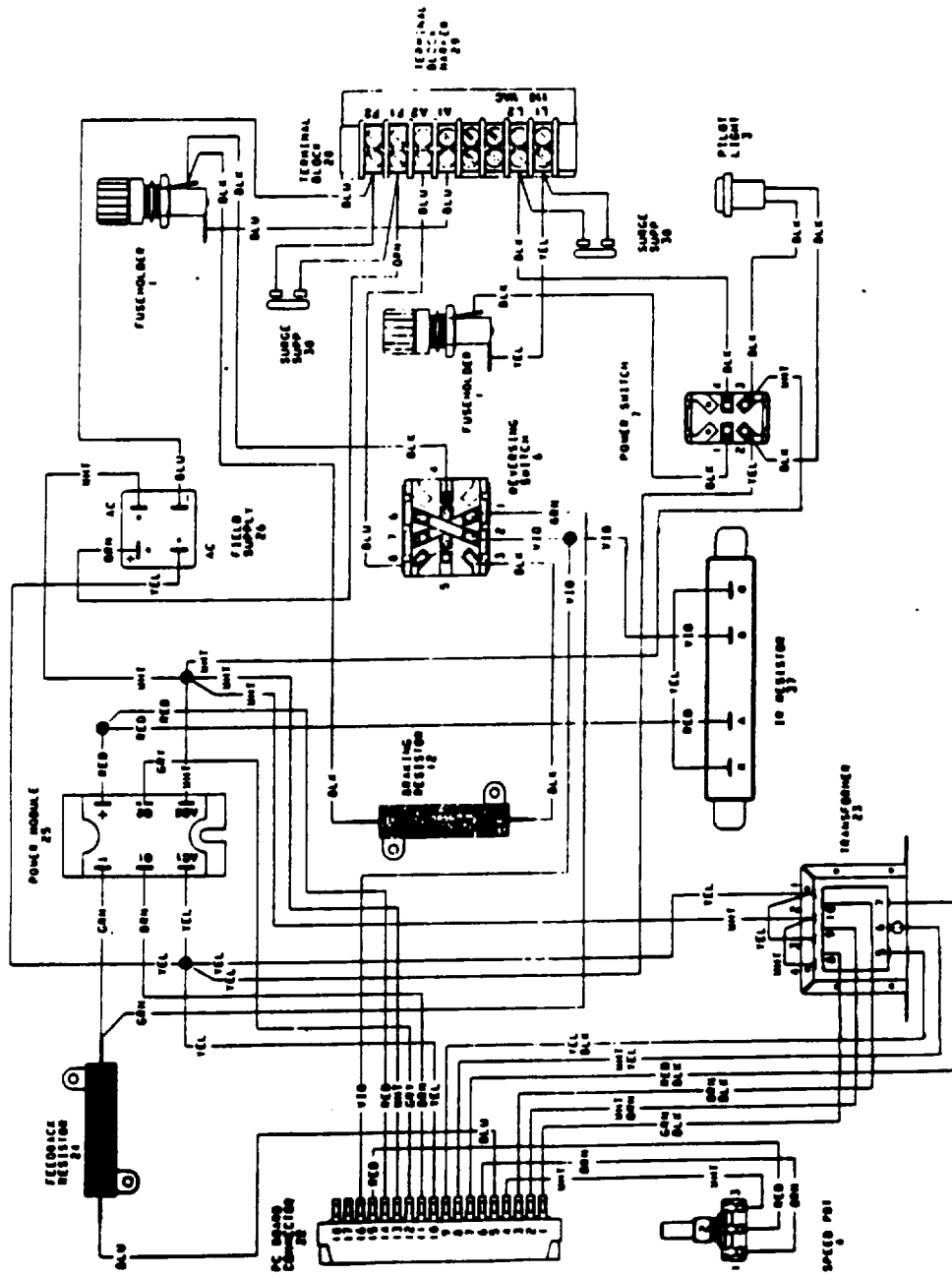


Figure C2 Wiring Schematic for Unsteady Pitching Mechanism Motor Controller.

REFERENCES

- Arena, Andrew, "The Effect of Asymmetric Vortex Wake Characteristics on a Slender Delta Wing Undergoing Wing Rock Motion", AIAA-89-3348, 1989.
- Bragg, M.B., and Soltani, M.R., "An Experimental Study of the Effect of Asymmetrical Vortex Bursting on a Pitching Delta Wing", AIAA Atmospheric Flight Mechanics Conference, Minneapolis, MN, August 15-17, 1988.
- Brandon, Jay M., and Shah, Gautam, H., "Effect of Large Amplitude Pitching Motions on the Unsteady Aerodynamic Characteristics of Flat-Plate Wings", AIAA-88-4331, August, 1988.
- Cunningham, Atlee M. Jr., "A Critique of the Experimental Aerodynamic Data Base for an Oscillating Straked Wing at High Angles", Fourth Symposium on Numerical and Physical Aspects of Aerodynamic Flows, California State University, January, 1989.
- Doebelin, Ernest O., Measurement Systems: Application and Design, 3rd Edition, McGraw-Hill Book Company, 1983.
- Earnshaw, P.B., "An Experimental Investigation of the Structure of a Leading-Edge Vortex", R.A.E. Tech Note Number Aero. 2740, March, 1961.
- Elle, B.J., "On the Breakdown at High Incidences Of the Leading-Edge Vortices on Delta Wings", Journal of the Royal Aeronautical Society, Volume 64, 1960.

- Er-EI, J., Effect of Wing/Canard Interference on the Loading of a Delta Wing", Journal of Aircraft, Volume 25, Number 1, 1987.
- Gad-el-Hak, M., Ho, C.M., and Blackwelder, R.F., "A Visual Study of a Delta Wing in Steady and Unsteady Motion", Proceedings of the Workshop on Unsteady Separated Flows, editors M.S. Francis and M.W. Luttges, Colorado Springs, Colorado, August 1983.
- Gad-el-Hak, M. and Ho., C.M., "The Pitching Delta Wing", AIAA Journal, Volume 23, Number 11, 1985.
- Holman, J.P., Experimental Methods for Engineers, McGraw-Hill Book Company, 1978.
- Hummel, D., and Srinivasan, P.S., "Vortex Breakdown Effects on the Low Speed Aerodynamic Characteristics of Slender Delta Wings in Symmetrical Flow", Journal of the Royal Aeronautical Society, Volume 71, 1967.
- Iwanski, Kenneth P., "An Investigation of the Vortex Flow Over a Delta Wing With and Without External Jet Blowing", Master's Thesis, University of Notre Dame, April, 1988
- Jarrah, Mohammad-Ameen M., "Unsteady Aerodynamics of Delta Wings Performing Maneuvers to High Angle of Attack", Ph.D. Dissertation, Stanford University, December, 1988.
- Jarrah, Mohammad-Ameen M., "Low-Speed Wing-Tunnel Investigation of Flow about Delta Wings, Oscillating in Pitch to Very High Angle of Attack", AIAA-89-0295, January, 1989.
- Kline, S.J., "The Purposes of Uncertainty Analysis", Journal of Fluids Engineering, Volume 107, June, 1985.

- Laidlaw, W.R., "Theoretical and Experimental Pressure Distributions on Low Aspect Ratio Wings Oscillating in Incompressible Flow", Massachusetts Institute of Technology Aeroelastic and Structures Research Laboratory Technical Report 51-2, September, 1954.
- Lamar, John E., and Campbell, James F., "Vortex Flaps - Advances Control Devices for Supercruise Fighters", Aerospace America, Volume 22, Number 1, January, 1984.
- Lambourne, N.C., and Bryer, D.W., "The Bursting of Leading-Edge Vortices - Some Observations and Discussion of the Phenomenon", Aeronautical Research Council Reports and Memorandum, Number 3281, 1962.
- LeMay, S.P., "Leading Edge Vortex Dynamics on a Pitching Delta Wing", Master's Thesis, University of Notre Dame, April, 1988.
- Lowson, M.V., "Some Experiments with Vortex Breakdown", Journal of the Royal Aeronautical Society, Volume 68, 1964.
- Magness, C., Robinson, O., and Rockwell, D., "Control of Leading-Edge Vortices on a Delta Wing", AIAA-89-0999, MARCH, 1989.
- McCormick, Barnes W., Aerodynamics, Aeronautics, and Flight Mechanics, John Wiley and Sons Publishers, 1979.
- McCune, James E., "Unsteady Wing Theory - The Karman/Sears Legacy", AIAA-88-3540, July, 1988.
- McKernan, J.F., "An Investigation of the Breakdown of the Leading Edge Vortices on a Delta Wing at High Angle of Attack", Master's Thesis, University of Notre Dame, January, 1983.
- Morris, Stephen L., et al., "Nonintrusive Measurements of Vortex Flows on Delta Wings in a Water Tunnel", AGARD 88-2595-CP, 1988.

- Parker, A.G., "Aerodynamic Characteristics of Slender Wings with Sharp Leading Edges - A Review", Journal of Aircraft, Volume 13, Number 3, 1976.
- Payne, Francis M., "The Structure of Leading Edge Vortex Flows Including Vortex Breakdown", Ph.D. Dissertation, University of Notre Dame, May, 1987.
- Peckham, D.H., "Low Speed Wind Tunnel Tests on a Series of Uncambered Slender Pointed Wings With Sharp Edges", Aeronautical Research Council Reports and Memoranda, Number 3186, 1958.
- Portnoy, H., "Unsteady Motion of Vortex-Breakdown Positions on Delta Wings", ICAS-88-683, 1988.
- Reynolds, G.A., and Abtahi, A.A., "Instabilities in Leading-Edge Vortex Development", AIAA-87-2424. Applied Aerodynamics and Atmospheric Flight Mechanics Conference, August 17-19, 1987.
- Rockwell, D., et al., "On Unsteady Flow Structure From Swept Edges Subjected to Controlled Motion", AFOSR Workshop on Unsteady and Separated Flows, U.S. Air Force Academy, Colorado Springs, Colorado, July 26-30, 1987.
- Scott, Matthew T., and McCune, James E., "Nonlinear Aerodynamics of Two-Dimensional Airfoils in Severe Maneuver", AIAA-88-0129, January, 1988.
- Thompson, S.A., Batill, S.M., and Nelson, R.C., "The Separated Flow Field on a Slender Wing Undergoing Transient Pitching Motions", AIAA-89-0194, January, 1989.
- Verhaagen, N.G., "Experimental and Numerical Investigation of the Vortex Flow over a Yawed Delta Wing", Seminar, University of Notre Dame, June, 1988.

- Visser, K.D., "Static Pressure Distributions for Delta Wings of Varying Chord Length", University of Notre Dame Aerospace Lab Memo, April, 1989.
- Visser, K.D., et al., "Control of Leading Edge Vortex Breakdown by Blowing", AIAA-88-0504, January, 1988.
- Visser, K.D., Nelson, R.C., and Ng, T.T., "A Flow Visualization and Aerodynamic Force Data Evaluation of Spanwise Blowing on Full and Half Span Delta Wings", AIAA-89-0192, January, 1989.
- Walpole, Ronald E., and Myers, Raymond, H., Probability and Statistics for Engineers and Scientists. 2nd Edition, MacMillan Publishing Company, Inc., 1978.
- Wentz, W.H., "Wind Tunnel Investigations of Vortex Breakdown on Slender Sharp-Edged Wings", PhD Dissertation. University of Kansas, 1968.
- Wolffelt, K.W., "Investigation of the Movement of Vortex Burst Position with Dynamically Changing Angle of Attack for a Schematic Delta Wing in a Water Tunnel with Correlation to Similar Studies in Wing Tunnel", AGARD CPP-413, 1986.

